

THE PHYSICAL PROPERTIES OF THE LAC DE GRAS
KIMBERLITES AND HOST ROCKS WITH CORRELATIONS
TO GEOPHYSICAL SIGNATURES AT DIAVIK DIAMOND
MINES, NWT

CARLA MARIA KENNEDY







Library and Archives
Canada

Published Heritage
Branch

395 Wellington Street
Ottawa ON K1A 0N4
Canada

Bibliothèque et
Archives Canada

Direction du
Patrimoine de l'édition

395, rue Wellington
Ottawa ON K1A 0N4
Canada

Your file *Votre référence*
ISBN: 978-0-494-80861-0
Our file *Notre référence*
ISBN: 978-0-494-80861-0

NOTICE:

The author has granted a non-exclusive license allowing Library and Archives Canada to reproduce, publish, archive, preserve, conserve, communicate to the public by telecommunication or on the Internet, loan, distribute and sell theses worldwide, for commercial or non-commercial purposes, in microform, paper, electronic and/or any other formats.

The author retains copyright ownership and moral rights in this thesis. Neither the thesis nor substantial extracts from it may be printed or otherwise reproduced without the author's permission.

In compliance with the Canadian Privacy Act some supporting forms may have been removed from this thesis.

While these forms may be included in the document page count, their removal does not represent any loss of content from the thesis.

AVIS:

L'auteur a accordé une licence non exclusive permettant à la Bibliothèque et Archives Canada de reproduire, publier, archiver, sauvegarder, conserver, transmettre au public par télécommunication ou par l'Internet, prêter, distribuer et vendre des thèses partout dans le monde, à des fins commerciales ou autres, sur support microforme, papier, électronique et/ou autres formats.

L'auteur conserve la propriété du droit d'auteur et des droits moraux qui protègent cette thèse. Ni la thèse ni des extraits substantiels de celle-ci ne doivent être imprimés ou autrement reproduits sans son autorisation.

Conformément à la loi canadienne sur la protection de la vie privée, quelques formulaires secondaires ont été enlevés de cette thèse.

Bien que ces formulaires aient inclus dans la pagination, il n'y aura aucun contenu manquant.


Canada

**The Physical Properties of the Lac de Gras Kimberlites and Host Rocks
with Correlations to Geophysical Signatures at Diavik Diamond Mines,
NWT**

Carla Maria Kennedy

A thesis submitted to the School of Graduate Studies in
the partial fulfillment of the requirements for the
degree of Masters of Science (Geophysics)

Department of Earth Sciences
Memorial University of Newfoundland
St. John's, Newfoundland

February 3, 2008

Abstract:

The geophysical response of any target is dependent upon the physical properties of the body and the surrounding host rock. The objective of this study is to develop an understanding of the physical properties of the kimberlites and host rocks at the Diavik Diamond Mine. Physical property data were collected at the Diavik Diamond Mine during a Mathematics of Information Technology and Complex Systems (MITACS) internship with Diavik. Data was collected using equipment supplied by Aurora Geosciences Ltd. The physical properties measured include density, resistivity, magnetic susceptibility and remanent magnetization. Samples were collected from drill core from previous drill programs that took place on Diavik property. In total, 400 kimberlite and surrounding host rock samples were collected from 16 kimberlite pipes. Pipes were selected based on core quality and pipe location.

The physical property data was statistically analyzed. Then, magnetic and gravity forward models of pipe A154N were made using GRAV3D (UBC-GIF 2002) and MAG3D (UBC-GIF 2002) software packages. These models were based on the data collected, along with a constrained geometric model of kimberlite pipe A154N given by Diavik. These forward models were compared to collected total magnetic field and gravity ground data which underwent a regional/residual separation using Li and Oldenburg's Method (1998). MAG3D and GRAV3D inversion software was then used to invert the residual data. The resulting subsurface models created by the inversion were then compared to the known model of pipe A154N.

After studying the physical properties and modeled geophysical signatures of pipe A154N, airborne total magnetic field data over the pipe was reviewed. Directional filters and edge detection techniques were tested to see how successful these methods were in helping to define the pipe A154N anomaly both on a large-scale map and in profiles over the pipe.

Acknowledgments:

This thesis would not have been possible without the support and cooperation of Memorial University, Diavik Diamond Mines, MITACS, and Aurora Geosciences.

At Memorial I found support and academic excellence from all staff and faculty. I would like to especially thank my supervisor, Dr. Hugh Miller, for your suggestions, time and guidance throughout the duration of this thesis. I feel honoured to be one of your last graduate students at Memorial, and to my committee member Dr. Colin Farquharson, for your insights, patience and your devotion to educate. I would like to also thank the following faculty and staff members at Memorial: Dr. Mark Wilson for his help with SPSS, Dr. Joe Hodych for allowing me to use his remanent magnetization equipment, Mr. Mohinder Grewal for his statistical guidance, and to Mrs. Gail Lamkin, and Mrs. Debbie Barnes for helping negotiate my contract with Diavik. Thank you to Mike Wheeler for allowing me to use his software package, to Mike Ash for the Gocad tutorials, and to Grant Lethbridge. Many thanks to UBC-GIF for allowing me to use their MAG3D and GRAV3D software.

I would also like to thank MITACS for providing me with a four month internship and funding. I would like to thank Diavik for providing me with core samples, funding, lab and office space, transportation, and geophysical information. I would like to especially thank Dave Eichenburg, Kari Thompson, Erika Kirsch, Roger Young, Gus Fomrades, Hayley McLean, and Gorden Clarke (formally of Diavik). I am grateful to the staff of Aurora Geosciences for providing room, transportation and lab equipment. I would especially like to thank Dr. Dave Hildes, Gary Vivian, Georges Belcourt, and Mike Power for bringing this project to life.

Finally, I would like to thank my family and friends for their love and support. A special thanks to Darrell, AeBoon, and Calvin, to Yuri for being my rock and my better half, and to my mom and dad for teaching me the importance of education.

Table of Contents

	Page#
List of Figures	vii
List of Tables	x
Chapter 1	
1.1 Introduction	1
1.2 A Brief Introduction to Diavik kimberlites	3
1.2.1 Magnetic signatures	4
1.2.2 Electromagnetics	5
1.2.3 Gravity	6
Chapter 2: Introduction to the Project Area	
2.1 Background	7
2.2 Regional Geology	8
2.2.1 Regional Structural Setting	10
2.2.2 Regional Tectonic History	10
2.3 Local Geology	12
2.3.1 Local Host Rocks	12
2.4 Kimberlites	14
2.4.1 Diamond Stability	14
2.4.2 Kimberlite Zones	16
2.4.3 Rock Type Classification	18
Chapter 3: Physical Property Data Collection	
3.1 Density	20
3.2 Magnetic Susceptibility	23
3.3 Remanent Magnetism	24
3.3.1 Koenigsberger Ratio	27
3.4 Resistivity	28
Chapter 4: Physical Properties Data Analysis	
4.1 Previous Kimberlite Physical Property Studies	33
4.2 Repeatability	34
4.2.1 Percent Differences - Density	35
4.2.2 Percent Differences - Magnetic susceptibility	36
4.2.3 Percent Differences - Remanent magnetization	37

4.2.4 Percent Differences - Resistivity	39
4.2.5 Repeatability Discussion	40
4.3 Physical Property Values: Initial Conclusions	40
4.4 Comparing pipe A154N to All Other Pipes	42
4.4.1 Comparisons: Discussions and Conclusions	43
4.5 Testing Correlations	45
4.5.1 Correlation Testing: Density vs. Physical properties	47
4.5.2 Density Correlation Conclusions	49
4.5.3 Correlation Testing: Depth vs. Physical Properties	50
4.5.4 Depth Correlation Conclusions	52
4.5.5 Final Notes on Correlation Testing	53
4.6 Comparison of Previous Studies to this Study	54
4.6.1 Previous Results: Discussion and Conclusions	55

Chapter 5: Physical Properties and Geophysical Signatures

5.1 Physical Property Models for Pipe A154N	73
5.2 Forward Modeling	74
5.3 Forward Modeling - Magnetic Field	76
5.3.1 Investigation into Remanent Magnetization	77
5.3.2 Magnetic Forward Modeling Discussion	78
5.4 Forward Modeling - Gravity	80
5.4.1 Gravity Forward Modeling Discussion	81
5.5 Forward Modeling Conclusions	82
5.6 Observed Geophysical Ground Data	83
5.6.1 Total Magnetic Field Data	84
5.6.2 Gravity Data	84
5.7 Regional Residual Separation	86
5.7.1 Upward Continuation	87
5.7.2 Second Order Polynomial	87
5.7.3 Li and Oldenburg Separation Method	88
5.7.4 Magnetics: Regional/Residual Removal Method	89
5.7.5 Comparing Magnetic Residual Results with Forward Modeling	90
5.7.6 Gravity: Regional/Residual Removal	91
5.7.7 Comparing Gravity Residual Results with Forward Modeling	91
5.8 Inversions	92
5.8.1 Data Misfit	93
5.8.2 Measure of Structure in the Model	93
5.8.3 Depth Weighting	95
5.9 Gravity and Magnetics Inversion	96
5.9.1 Gravity Inversion	97
5.9.2 Magnetics Inversion	98
5.9.3 Inversion Discussion and conclusions	100
5.10 Resistivity	101

Chapter 6: Exploration for Kimberlite Pipes	
6.1 Airborne Magnetic Investigation	149
6.1.1 Directional Filters	150
6.1.2 Edge Detection Techniques	151
6.1.3 Discuss and Conclusions	152
6.2 Other Kimberlite Detection Techniques	153
Chapter 7: Conclusions	162
References	167
Appendix A	171

List of Figures

	Page#
Chapter 1	
Figure 1.1: Kimberlite magnetic signatures	4
Figure 1.2: Kimberlite resistivity signatures	6
Chapter 2	
Figure 2.1: Location of Diavik Diamond Mine	7
Figure 2.2: Location of Slave Craton	9
Figure 2.3: Geology map of Eastern Island	13
Figure 2.4: Graph of diamond stability field	15
Figure 2.5: Diamond stability window	16
Figure 2.6: Standard kimberlite model	17
Chapter 3	
Figure 3.1: Alfa Mirage electronic Densimeter	21
Figure 3.2: MolSpin BigSpin	26
Figure 3.3: Resistivity circuit design	30
Figure 3.4: Generator and amplifier	31
Figure 3.5: Resistivity circuit setup	32
Chapter 4	
Figure 4.1: Location of collected pipes	57
Figure 4.2: Density measurements	58
Figure 4.3: Remanent magnetization measurements	59
Figure 4.4: Magnetic Susceptibility measurements	60
Figure 4.5: Resistivity measurements	61
Figure 4.6: Density histograms and statistical summary	62
Figure 4.7: Remanent magnetization histograms and statistical summary	63
Figure 4.8: Magnetic Susceptibility histograms and statistical summary	64

Figure 4.9: Resistivity histograms and statistical summary	65
Figure 4.10: Density vs. Remanent magnetization	66
Figure 4.11: Density vs. Magnetic Susceptibility	67
Figure 4.12: Density vs. Resistivity	68
Figure 4.13: Depth vs. Density	69
Figure 4.14: Depth vs. Remanent magnetization	70
Figure 4.15: Depth vs. Magnetic Susceptibility	71
Figure 4.16: Depth vs. Resistivity	72

Chapter 5

Figure 5.1: Geology model pipe A154N	103
Figure 5.2: Magnetic Susceptibility model pipe A154N	104
Figure 5.3: Density model pipe A154N	105
Figure 5.4: Koenigsberger ratio for each rock type	106
Figure 5.5: Forward model magnetic susceptibility model pipe A154N	107
Figure 5.6: Magnetic susceptibility model crater zone pipe A154N	108
Figure 5.7: Forward model magnetic susceptibility crater zone	109
Figure 5.8: Magnetic susceptibility model root zone pipe A154N	110
Figure 5.9: Forward model magnetic susceptibility root zone	111
Figure 5.10: Magnetic field strength pipe A154N	112
Figure 5.11: Forward model density model pipe A154N	113
Figure 5.12: Density model crater zone pipe A154N	114
Figure 5.13: Forward model density crater zone	115
Figure 5.14: Density model root zone pipe A154N	116
Figure 5.15: Forward model density root zone	117
Figure 5.16: Gravity response pipe A154N	118
Figure 5.17: Total magnetic field ground map over pipe A154	119
Figure 5.18: Gravity ground map over pipe A154N	120
Figure 5.19: Bathymetry map over pipe A154N	121
Figure 5.20: Gravity map with bathymetry contours	122
Figure 5.21: Profile of gravity and bathymetry data	123
Figure 5.22: Map of Bouguer corrected gravity data	124
Figure 5.23: Profile of gravity, bathymetry and Bouguer corrected data	125
Figure 5.24: Density contrast model	126
Figure 5.25: Map of gravity data after lake method corrections	127
Figure 5.26: Profile of gravity, bathymetry and lake method corrected	128
Figure 5.27: Observed magnetic dataset	129
Figure 5.28: Magnetic susceptibility model with pipe A154N removed	130
Figure 5.29: Resultant magnetic regional field for pipe A154N	131
Figure 5.30: Residual magnetic field for pipe A154N	132
Figure 5.31: Cartoon of Li and Oldenburg regional/residual removal	133
Figure 5.32: Observed gravity dataset	134

Figure 5.33: Density contrast model with pipe A154N removed	135
Figure 5.34: Resultant gravity regional data for pipe A154N	136
Figure 5.35: Residual gravity frilled for pipe A154N	137
Figure 5.36: Depth weighting parameters	138
Figure 5.37: Predicted gravity dataset default mode inversion	139
Figure 5.38: Gravity default mode inversion model	140
Figure 5.39: Predicted gravity dataset model mode inversion	141
Figure 5.40: Gravity model mode inversion model	142
Figure 5.41: Trimmed residual total magnetic field data	143
Figure 5.42: Trimmed and zeroed residual total magnetic field data	144
Figure 5.43: Predicted total magnetic field dataset default mode inversion	145
Figure 5.44: Predicted magnetic susceptibility default mode model	146
Figure 5.45: Predicted total magnetic field dataset model mode inversion	147
Figure 5.46: Predicted magnetic susceptibility model mode model	148

Chapter 6

Figure 6.1: Airborne total magnetic field map	155
Figure 6.2: Total magnetic field response over pipe A154N	156
Figure 6.3: Total magnetic field map after trend removal	157
Figure 6.4: Profile comparing total magnetic field before and after trend removal	158
Figure 6.5: Horizontal gradient of the total magnetic field	159
Figure 6.6: Analytical signal of the total magnetic field	160
Figure 6.7: Profile of the resulting magnetic horizontal gradient and analytical signal	161

List of Tables

	Page#
Chapter 3	
Table 1: Variation of water density with temperature	22
Chapter 4	
Table 2: Percent difference in density repeats	36
Table 3: Percent difference in magnetic susceptibility repeats	37
Table 4: Percent difference in remanent magnetization repeats	38
Table 5: Percent difference in resistivity repeats	39
Table 6: Representative repeatability results for each measurement	40
Table 7: Statistical summary of the physical property values	42
Table 8: Spearman rank test results for density vs. physical properties	49
Table 9: Spearman rank test results for depth vs. physical properties	52
Table 10: Comparing kimberlite vs. host rock relative values to previous studies	55
Table 11: Comparing Crater zone vs. root zone relative values to previous studies	55
Chapter 5	
Table 12: Magnetic susceptibility and density values for pipe A154N	74
Table 13: Geomagnetic field values for the location of A154N in 1994	78
Table 14: Density contrast values for pipe A154N	81
Table 15: Forward model predicted anomaly sizes	83

1.1 Introduction

Now that diamonds have been discovered in Canada's North and mines are in operation, the pressure to find more diamonds is rising. Kimberlite, an intrusive volcanic rock, is the main source rock for diamonds. Geophysical techniques have been at the heart of the Canadian kimberlite exploration industry from the beginning, and continue to remain one of the primary techniques for kimberlite exploration. During the history of the Diavik Diamonds Mine, the mine site and exploration properties have been extensively explored; with this comes the need for more effective and thorough exploration techniques. It is believed that these new techniques will only come from a more careful investigation into previously discovered kimberlite pipes. It is only by the study of known cases that we can learn how to discover the undiscovered cases. Since geophysical surveys respond to variations in the physical properties of the subsurface, knowing more about the physical properties of Diavik's kimberlites and their host rocks will lead to an increase in the interpretation accuracy of geophysical models which in turn will lead to an increase in exploration success.

The objective of this thesis was to collect a full suite of physical property data to be used in conjunction with data from previously conducted geophysical surveys to increase the understanding of the relationship between physical properties and kimberlite pipe geophysical signatures. These relationships were defined by using forward modeling and inversion techniques. This data was then used to isolate pipes in airborne total magnetic field data.

The data for this project was collected during a Mathematics of Information Technology and Complex Systems (MITACS) internship at Diavik Diamond Mines from June to October 2006. The measured properties include magnetic susceptibility, remanent magnetization, density, and resistivity. All laboratory equipment was provided by Aurora Geosciences Ltd. The details of the laboratory equipment and procedures will be discussed in Chapter 3.

Physical properties from the major kimberlite zones and host rock units were measured using 400 samples from 16 kimberlites pipes of the Lac de Gras kimberlite field on Diavik property. Chapter 4 will discuss statistical techniques used to define physical property inter relationships and representative values for the collected kimberlite and host rocks samples. Investigating Canadian kimberlite physical properties is not a new idea; others authors including Mwenifumbo, Hunter, and Killeen (1996) and Katsube and Kjarsgaard (1996) have previously published studies on the topic. Neither study concentrated on the Diavik area or sampled a large population of kimberlites and host rocks. The conclusions of these authors will be compared to the conclusions of this study in Chapter 4.

Inversion and forward modeling was performed using collected physical property values, along with an accurate geometric model of a kimberlite pipe. This investigation is presented in Chapter 5.

A study using edge detection techniques on airborne total magnetic field data is presented in Chapter 6. It relies upon the information learned from the inversion and forward modeling of pipe A154N. The potential of using pattern recognition techniques is also discussed.

1.2 A Brief Introduction to Diavik Kimberlites

There are three economic pipes on Diavik property (A154N, A154S and A418) which are Eocene in age (Graham et al. 1999). These pipes are located within a few kilometers of each other and are considered to be from the same cluster. These pipes have been investigated thoroughly. In contrast, there is little documentation about the more than 60 non-economic pipes that are distributed throughout Diavik properties.

As a result of glaciation the majority of kimberlite pipes at Diavik are found beneath lakes. Since kimberlite is a weak rock, retreating glaciers removed the top layers of the kimberlite pipes making ideal depressions for water to collect.

The diameter of a Diavik kimberlite pipe ranges from approximately 75m to 150m. The pipe walls have mean estimated dip between 78° and 84° that tend to converge at depth. However, the shapes and sizes of the pipes vary (Graham et al. 1999).

1.2.1 Magnetic Signatures

Kimberlite magnetic signatures detected in magnetic surveys originate from the contrast in magnetization between kimberlites and host rocks. By reviewing airborne total magnetic field data which was collected between 1992 –1997 and compiled by Aurora Geosciences, various magnetic signatures can be observed (Figure 1.1). Kimberlite pipes have been found with positive, negative and neutral anomalies.

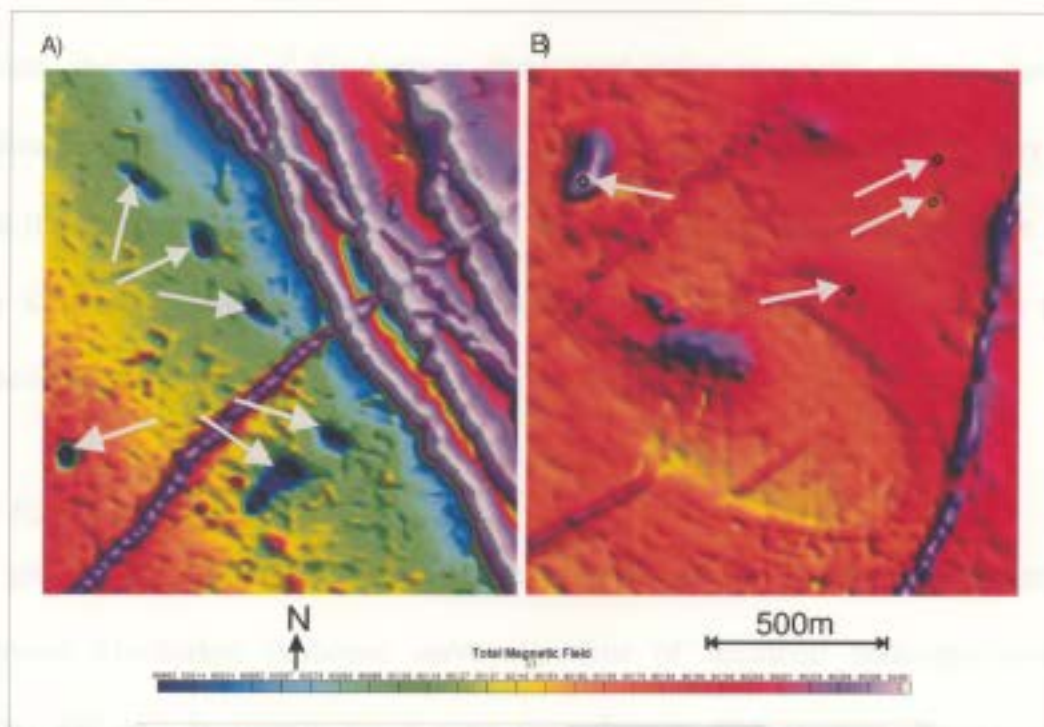


Figure 1.1: Examples of the different magnetic responses found on Diavik property with arrows pointing to kimberlite pipes. A) A typical kimberlite pipe cluster with negative anomalies. B) A kimberlite pipe cluster with neutral to high positive anomalies. Note due to issues of confidential XY UTM coordinates are not given.

Kimberlite pipes can be spatially and temporally associated with diabase dykes, regional faults, and geological contacts (Power et al. 2004). Pipes tend to be found in clusters, and in general these clusters are of similar ages and possess similar magnetic signatures. Due to these intimate age relationships, it can be assumed that each cluster has a similar

intensity and direction of remanent magnetization, as this is locked in during the cooling process (Power et al. 2004). This is a generalization, and exceptions to the previous statement have been found. The varying remanent magnetization of a kimberlite can either produce a negative magnetic anomaly that is easily recognized (remanent field is opposing present field) or produce a positive magnetic anomaly that is often obscured and difficult to recognize (remanent field is in the general direction of the present field).

To date, the majority of kimberlites discovered using magnetic surveys have been negative magnetic anomalies. These small, circular, negative anomalies are easy to pick out in the comparatively positive magnetic background. It is assumed that there are still many kimberlites that have not yet been discovered due to their neutral or positive magnetic responses.

1.2.2 Electromagnetics

Both ground and airborne EM systems have been successful in finding kimberlites in the Northwest Territories. Airborne surveys consist of multicoil helicopter-borne EM systems and less frequently fixed wing time domain EM systems. Relevant ground surveys include HLEM, and coincident loop TDEM. By reviewing an airborne apparent resistivity map (56kHz) that was collected in 1997 and compiled by Aurora Geosciences, the relationship between pipe cluster and apparent resistivity response can be explored (Figure 1.2). Unlike magnetic data, pipes within a cluster do not generally possess similar apparent resistivity responses.

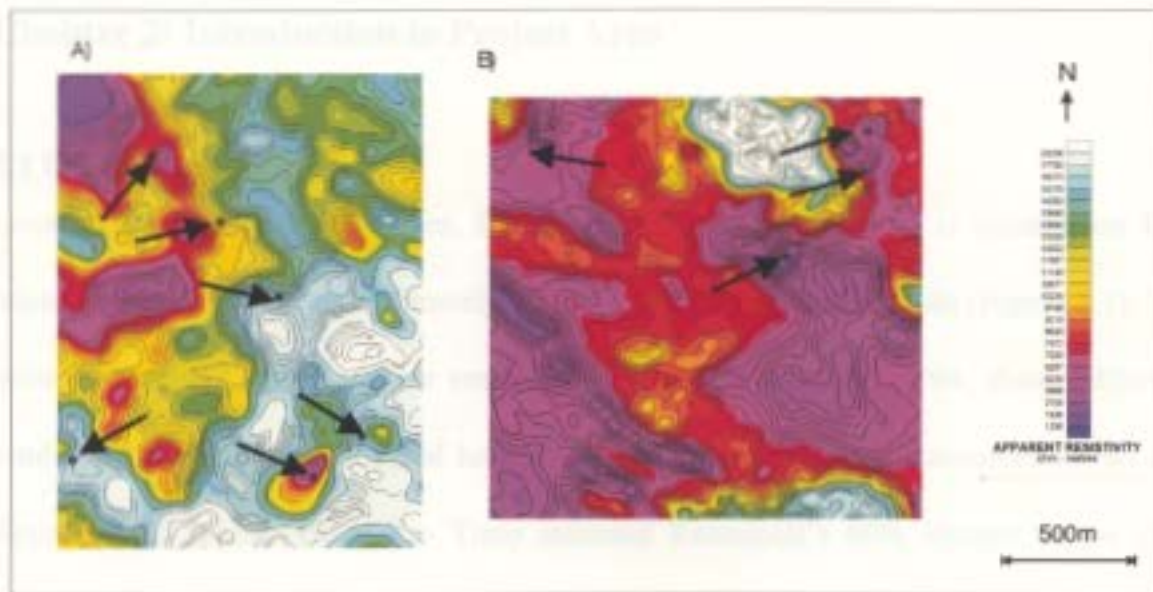


Figure 1.2: Examples of the different resistivity responses found on Diavik property with arrows pointing to the kimberlite pipes. A) A typical kimberlite pipe cluster with anomalies of various intensities. B) A kimberlite pipe cluster with low resistivity anomalies. Note due to issue of confidential UTM coordinates are not given.

1.2.3 Gravity

Gravity is usually used during the secondary phase of kimberlite exploration, after a potential target has been found and further information is needed. Ground gravity surveys are not considered the fastest or most cost effective way for looking for kimberlite pipes. Gravity data is very sensitive to elevation changes and since the majority of kimberlites are found beneath lakes, a careful removal of bathymetric effects is necessary in order to isolate the kimberlite response.

Chapter 2: Introduction to Project Area

2.1 Background

Located in Northwest Territories, Diavik Diamond Mine (Diavik) is situated on Eastern Island in Lac De Gras, approximately 300 km northeast of Yellowknife (Figure 2.1). The mine is accessed by air, or ice road during winter months. In 1994, diamondiferous kimberlite pipes were discovered here by a joint venture of Aber Resources (40%) and Kennecott (60%). In 1996, Rio Tinto assumed Kennecott's 60% interest in the joint venture and established Diavik Diamonds Mines Inc.

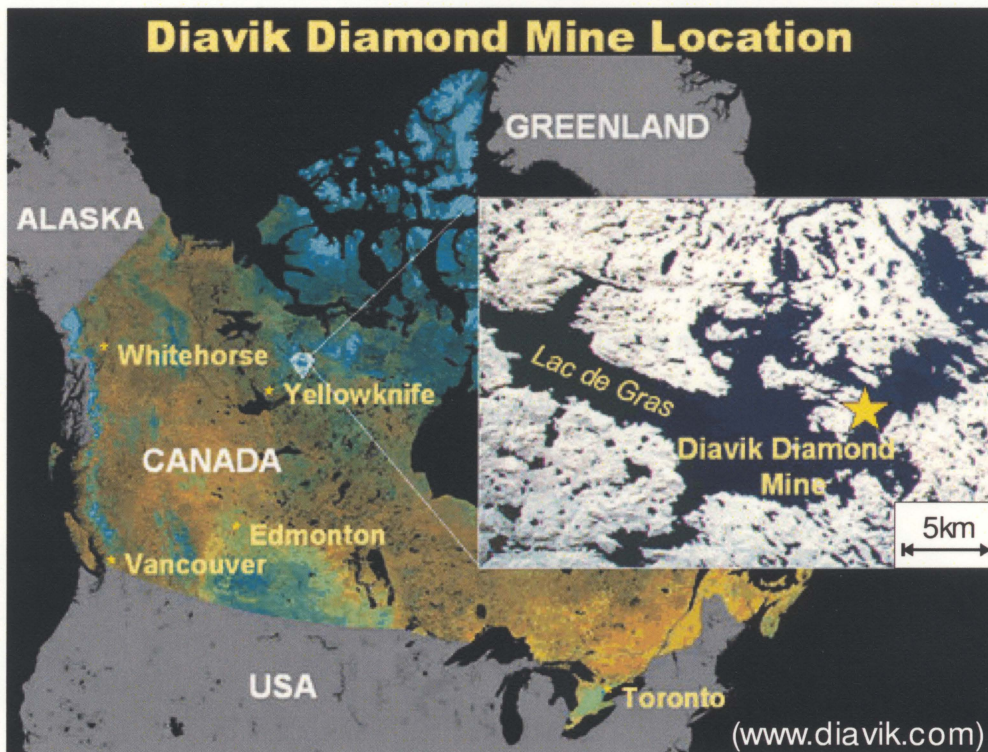


Figure 2.1: Map of North America showing the location of the Diavik Diamond Mine. A yellow star notes the location of Eastern Island.

Lac de Gras is approximately 60 km long and averages 16 km wide, with a shoreline length of 740 km. The lake has an average depth of 12 m and a maximum depth of 56 m and the water quality of this lake is close to distilled water (Diavik 2007). Surrounding Lac de Gras is rolling tundra with very few trees, numerous lakes, bedrock outcrops and glacial deposits of boulders, till and eskers. Permafrost occurs within 1-2m of the surface and continues to an undefined depth (Diavik 2007).

At the moment, pipe A154S and pipe A154N are open pit mines, and are in the process of transitioning into underground mines whereas pipe A418 will begin mining Fall 2007. The estimated reserve of the three ore bodies is 29.8 million tonnes at 3.2 carats/tonne (diluted). Excluding any new discoveries, the mine life is estimated to be 10 to 15 years. Diamond production began in January 2003. (Diavik 2007)

2.2 Regional Geology

Diavik is located in the Archean Slave Craton in the northwestern section of the Canadian Shield (Figure 2.2) (King and Helmstaedt 1997).

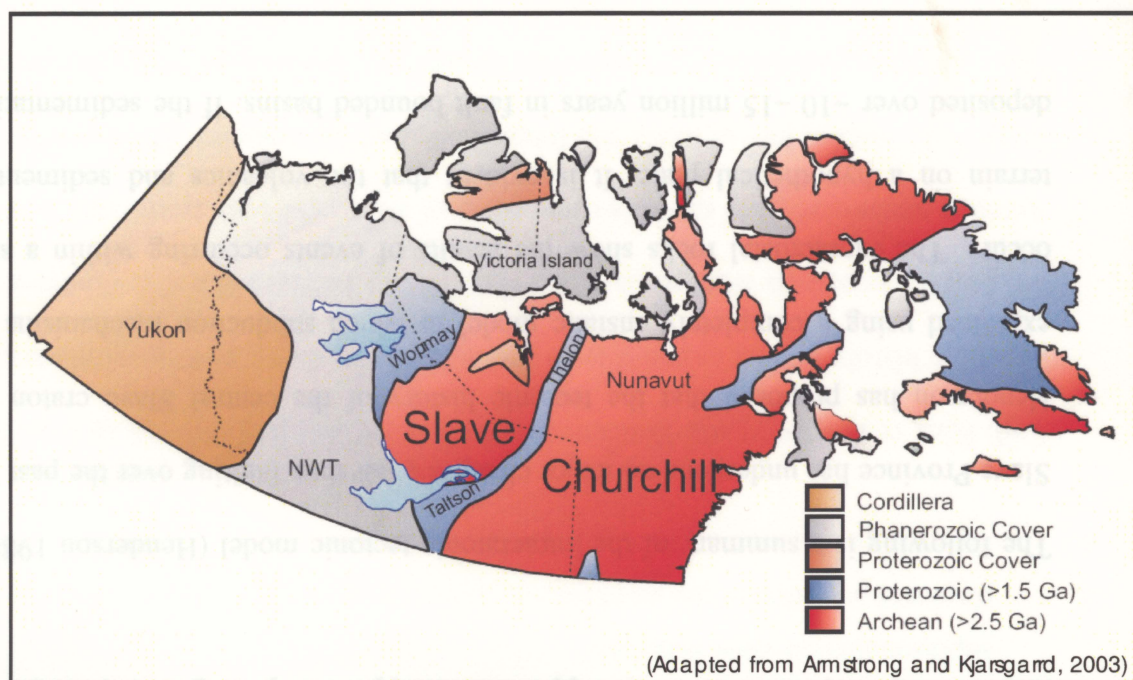


Figure 2.2: Map showing the location of the Slave Craton which straddles the boarder between the Northwest Territories and Nunavut.

The surface exposure of the province consists of approximately 65% late-Archean granitoids (2.7 to 2.55 Ga) and 35% late-Archean supracrustal rocks (2.72 to 2.66 Ga) of the Yellowknife Supergroup (Graham et al. 1999). The Yellowknife Supergroup dominates the central and eastern parts of this province. It is dominantly comprised of volcanic and turbiditic sedimentary rocks (King and Helmstaedt 1997).

The Yellowknife Supergroup overlies the middle-Archean Central Slave Basement Complex (CSBC), which has only been identified in the west and central portions of the Slave Craton (Davis et al. 2001). The CSBC dips to the east and underlies the central part of the craton at depth (Davis et al. 2001). However, there has been no observation of

basement in the eastern portion of the craton (Bleeker et al. 2001). The absence of the CSBC is supported by isotopic data (Bleeker et al. 2001).

2.2.1 Regional Structural Setting

The Slave Province is bounded in the east by the Thelon Orogen (~2.2 Ga), to the west by the Wopmay Orogen (1.9-2.1 Ga), to the south by the Great Slave Lake Shear Zone, to the north by the overlapping Proterozoic and younger supracrustals rocks of the Bear Province and Artic Platform (Griffin et al. 1999), to the southeast by the McDonald Faults and to the northeast by the Bathurst Fault (Graham et al. 1999)

2.2.2 Regional Tectonic History

The tectonomagmatic evolution of the area remains controversial, with evidence for two tectonic models (Kjarsgaard 1996) including an intracratonic model, supported by Henderson (1988) and a subduction-type model, supported by King et. al (1992).

The following is a summary of the intracratonic tectonic model (Henderson 1988): The Slave Province has undergone no major changes other than faulting over the past 2.5 Ga. Henderson has proposed that the tectonic history of the central Slave craton can be explained using a completely ensialic model in which subduction mechanisms do not occur. The supracrustal rocks show the results of events occurring within a silicious terrain on a hypothetical plate. It is evident that the volcanics and sediments were deposited over ~10 –15 million years in fault bounded basins. If the sedimentation and

volcanism took place in similar environments over the same period time, then a tectonic mechanism involving regional extension of the crust is required. It would have been active over the entire province at approximately the same period of time. Such a tectonic mechanism may have been the interaction between hypothetical Archean plates, although Henderson admits that there are a variety of processes that can result in regional crustal extension.

Alternatively, King et al. (1992) believes that there is evidence that subduction has taken place. The best model to explain the geology of the Contwoyto Lake area (located in the central Slave Craton) is one of progressive arc – continent collision. King et al. (1992) summarized this model as:

1. Early construction of an arc or arcs
2. Lateral accretion of arc components to an ancient western craton
Ongoing deformation of accreted assemblages during emplacement of suprasubduction-zone magmas,
3. Regional elevation of the geotherm,
4. Massive crustal melting during uplift and cooling.

Both King et al. (1992) and Henderson (1988) admit that it is difficult to determine the complete history of this craton due to the lack of remaining geological evidence. This controversy is not an isolated case. Bleeker (2002) believes that the controversy over Archean tectonic models exists because most of the world's Archean crust is too small (only 7- 11 million km² in total), too fragmented, and too complex. He also adds that the Slave craton in particular is characterized by complex depositional and volcanic histories

that have been overprinted by polyphase deformation and multiple intrusive granitoid events (Bleeker 2002). It is unlikely we will ever know what exactly occurred in this area during Archean time.

2.3 Local Geology

2.3.1 Local Host Rocks

Kimberlite pipes are hosted in a complex of Archean granitoids and micaceous meta sediments of the Slave Structural Province. The host rocks for the Diavik kimberlites consist of the Yellowknife Supergroup and two types of granitoids (Graham et al. 1999) (Figure 2.3). One type of granitoid consists of a suite of 2610-2600 Ma syn- to late-deformational monzodiorite, granodiorites and trondhjemites, whereas the other suite of granitoids consists of 2599-2580 Ma post-deformation mica granites (Graham et al. 1999). A magnetic survey can easily distinguish the two types of granitoids: the post-deformation mica granites are slightly more magnetic than the potassic (pink) granitoids (Graham et al. 1999). The Yellowknife Supergroup as described earlier consists of volcanic and turbiditic sedimentary rocks.

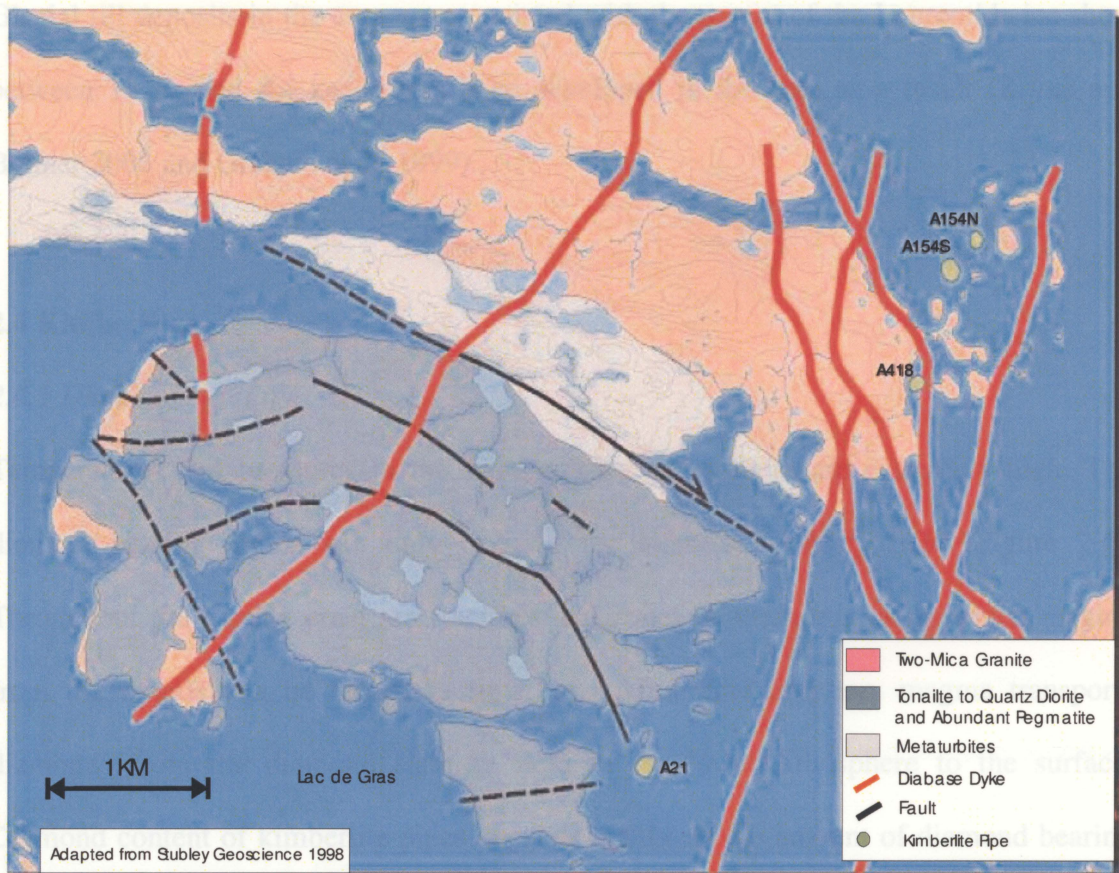


Figure 2.3: A simplified geological map of Eastern Island, Lac de Gras, NWT.

There are three dominant sets of diabase dykes of Proterozoic age cutting the Slave craton including the Mally (ca. 2.23 Ga) trending to the northeast, the Lac de Gras (ca. 2.02 Ga) trending to the north-northeast and the Mackenzie dykes (ca. 1.27 Ga) trending to the northwest (Bryan and Bonner 2003). These dykes correlate with Proterozoic dyke swarms in the central Slave Province (Stubley 1998). Individual dykes are irregular in width, strike, and dip and are texturally indistinguishable. (Stubley 1998)

Glacial till deposits in the area are associated with the retreat of the Laurentide ice sheet between 14 ka and 8.4 ka. Eskers have developed in the area as a result (Bryan and Bonner 2003 and Graham et al. 1999).

2.4 Kimberlites

2.4.1 Diamond Stability

Temperatures and pressures in the Earth's lower lithosphere are extremely high. The diamond-bearing region can only exist in the diamond stability field (Figure 2.4). Throughout the Earth's crust are fractures and zones of weakness along which magma from the mantle can be forced to flow. In a kimberlite eruption, magma transports diamonds from the diamond stability field in the lower lithosphere to the surface. Diamond content of kimberlite pipes depends highly on the amount of diamond bearing mantle material encountered by the kimberlite magma during ascent (Kjarsgaard 1996). The catalyst of kimberlite eruptions is unknown

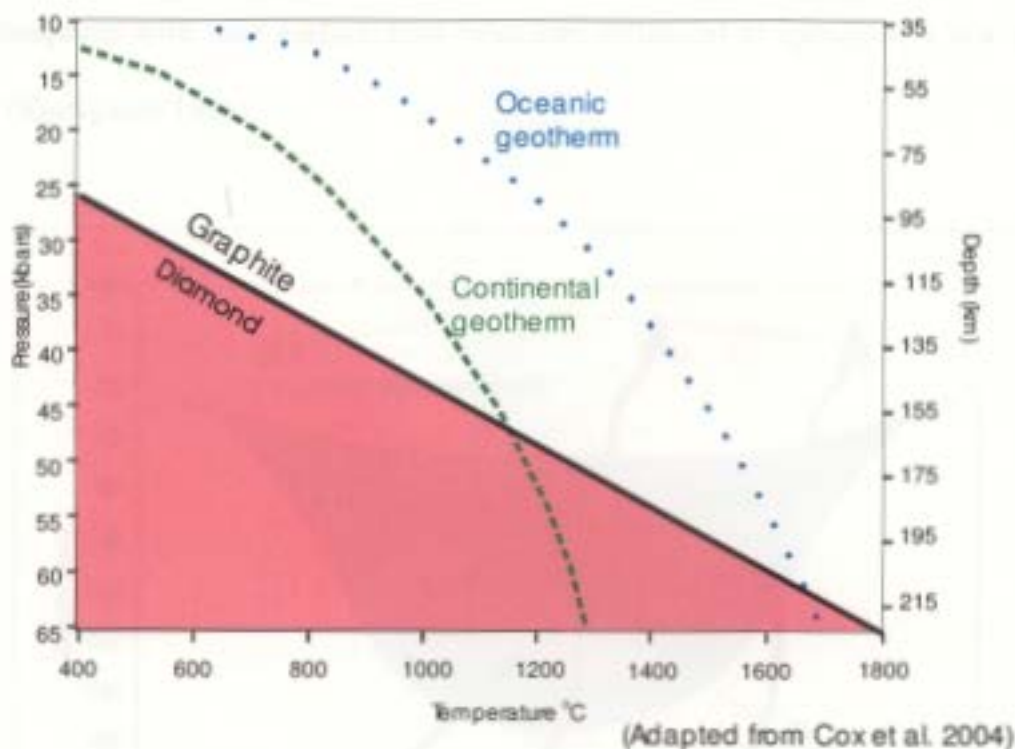


Figure 2.4: The diamond stability field (in pink) shows the temperature and pressure conditions required for diamonds to grow and be stable.

As shown in Figure 2.4, the diamond stability field only exists within the pressure range of 25 kbars to 65 kbars, at depths between 95 km and 220 km and at temperatures between 400°C and 1800 °C. If these conditions are not met, graphite will be formed instead of diamonds. Diamonds are considered to be metastable outside their stability field. This implies that they are kinetically stable, but not thermodynamically stable, on the Earth's surface and throughout most of the Earth's crust (May 2007).

In order for the diamonds to reach the Earth's crust, diamondiferous kimberlite eruptions must rapidly transport diamonds from within the diamond stability field (or "diamond window") to the Earth's surface (Figure 2.5). Kimberlite magma ascends rapidly through

the lithosphere with near surface vent velocities estimated at speeds of a few hundred km/hr (Kjarsgaard 1996).

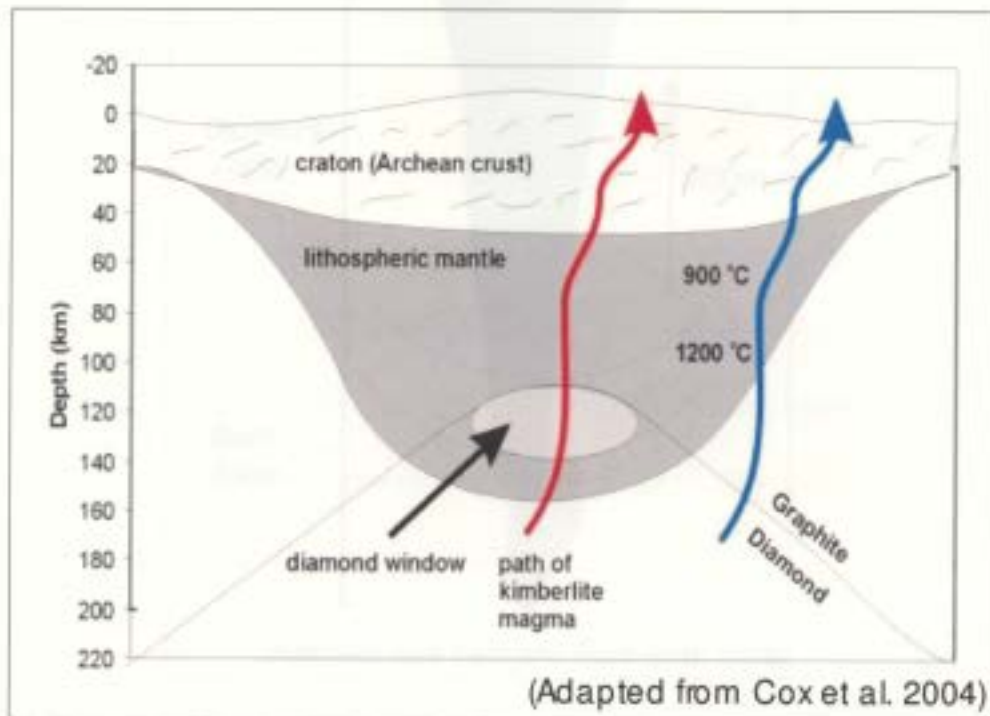


Figure 2.5: Cartoon of the diamond stability window (Adapted from Cox et al. 2004).

2.4.2 Kimberlite Zones

The violent eruption causes debris to explode out of the pipe leaving a crater which overtime is backfilled with a mixture of material. This may include kimberlite blown out during the eruption and host rock and organic material from the surrounding area. This heterogeneous mixture causes unique zones and layering to form in the pipe. (Lorenz and Kurszlauskis 2003) (Figure 2.6)

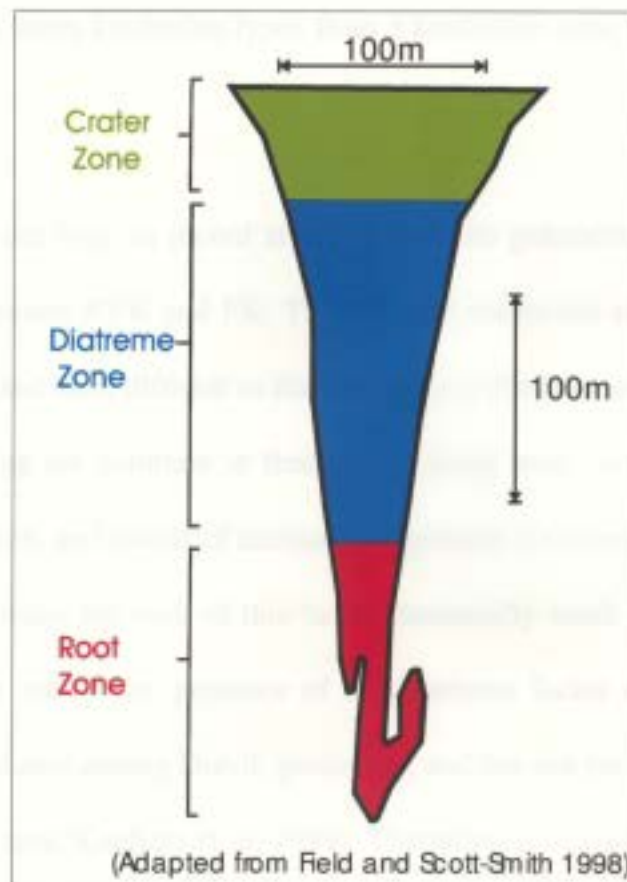


Figure 2.6: The standard model of a kimberlite. The three major zones include crater, diatreme, and root.

The three major zones in a typical kimberlite (Figure 2.6) include the crater, diatreme and root zones. These kimberlite zones are composed of various types of kimberlite. The crater zone is interpreted as the region of backfill after the kimberlite eruption. It includes both pyroclastic kimberlite (PK) and resedimented volcanoclastic kimberlite (RVK). The naming system that is commonly used utilizes the term volcanoclastic kimberlite (VK) when textures that distinguish RVK and PK are not clear (Graham et al. 1999). The diatreme zone is composed mostly of tuffisitic kimberlite. The root zone is comprised of hypabyssal kimberlite (HK). It should be emphasized that this model is a

generalization. At times kimberlite types from a kimberlite zone can be found in another zone.

The majority of core logs on record at Diavik use the generalized term VK, instead of distinguishing between RVK and PK. The VK unit comprises somewhat massive beds, which are altered and have difficult to discern textures (Graham et al. 1999). Sedimentary sorting and bedding are common in these units, along with clay minerals, xenoliths of host rock, vegetation, and fossils of terrestrial organisms (Graham et al. 1999). The added material tends to make the rock of this facies structurally weak compared to kimberlite found in the root zone. The presence of the diatreme facies in Diavik kimberlite is currently being debated among Diavik geologists, and has not yet been recognized in drill samples from the area (Graham et al. 1999). Therefore, it is assumed for the purpose of this thesis that a diatreme kimberlite zone does not exist in Diavik kimberlites. HK is formed by the crystallization of volatile rich kimberlite magmas and occurs as a system of dykes and sills, which fed the eruption.

2.4.3 Rock Type Classification

Rock types were organized into the following three groups: host rock, crater zone and root zone. The host rock group includes metaturbidities, tonalite-quartz diorite and two-mica granite. The kimberlite types VK, RVK, and PK have all been placed under the umbrella term of the crater zone, the HK were grouped in a separate group called the root zone.

Chapter 3: Physical Properties Laboratory Measurements

Basic physical rock property data is important information required for interpreting geophysical data. It provides an opportunity for further development and refinement of geophysical models and methods (Katsube and Scromeda 1994). The main objective of this chapter is to review the principles behind the physical property being measured, along with the precautions used during data collection to avoid laboratory bias. As noted in Chapter 1, the physical rock property data types measured during this thesis include density, remanent magnetization, magnetic susceptibility, and resistivity.

There is debate over the relationship between the properties obtained by laboratory measurements and in situ properties. Once out of the ground, samples used in laboratory experiments can become weathered, fragmented, dehydrated, or altered in the process of being obtained (Telford et al. 1990). As a result, the physical property value collected may not be representative of the in situ value of the sample. Due to the timing and budget of this project, data collection using borehole-logging equipment was not feasible. All data was collected from core stored at the Diavik mine site and was obtained from previous drill programs. The core used for this study was stored outside in wooden core boxes and was exposed to the extreme weather conditions of the area. As a result, some core had become weathered and deteriorated. Great efforts were made to ensure that physical property measurements were collected as accurately as was reasonably possible.

3.1 Density

The physical property affecting gravity anomalies is the local variation in density (Telford et al. 1990). Density can be measured in situ by borehole logging tools, estimated from seismic velocity, or more commonly, measured in a laboratory using small samples. Density of a rock sample depends on the density of the constituent minerals in combination with the porosity and nature of the pore fluid within the rock (Telford et al. 1990). The rock samples that were used during this thesis had generally been stored for many years in core boxes; samples were often dehydrated and weathered. Since the saturation percentage of a sample is a major factor in bulk density measurements all samples were re-saturated in a vacuum chamber. It was assumed that the samples were originally saturated in the subsurface. This is a realistic assumption since most kimberlite pipes are commonly found beneath or close to bodies of water, and the water table in the tundra is commonly very close to the surface. There is the issue of permafrost that does extend to an unknown depth in the area. However, since most kimberlite pipes are found under bodies of water it is not thought that permafrost is an issue.

The nature of the pore fluid also plays a role in the bulk density of a sample, therefore consideration was given to using water with compositional properties similar to those of water found in the area. Lac de Gras, under which several pipes have been discovered, has a water composition that has been described as close to distilled. However, it is unknown how the water properties and composition changes as it flows through the

groundwater systems under the lake. In addition, some samples came from localities near bodies of water of unknown water properties. After considering these factors, it was decided that water from the Diavik mine site water station would be distilled using a reverse osmosis water purification system and used to re-saturate the samples. This substitution of distilled water will shift the bulk density of the samples by an unknown amount, however it is felt that this change will probably be negligible.

Density is defined in equation (1):

$$\rho = \frac{m}{v} \quad (1)$$

where: m = the mass of the sample (g)
 v = the volume of the sample (cm^3)
 ρ = density (g/cm^3)

The density measurements for this project were collected using an Alfa Mirage Electronic Densimeter MD-300S (Figure 3.1).



Figure 3.1: Picture of the Alfa Mirage Electronic Densimeter MD-300S.

The instrument measures density based on Archimedes' principle, which is the standard practice of measuring density in a laboratory environment. After saturation, the sample is weighed in air, and then weighed in water. By using equation (1), the density of the rock can be determined by the following equation (2):

$$\rho_{rock} = \rho_{water} \left(\frac{W_{rock\ in\ air}}{W_{rock\ in\ air} - W_{rock\ in\ water}} \right) \quad (2)$$

where: ρ_{rock} = density of the rock (g/cm^3)
 ρ_{water} = density of the water (g/cm^3)
 $W_{rock\ in\ air}$ = weight of the rock in air (g)
 $W_{rock\ in\ water}$ = weight of the rock in water (g)

It is important to note that the density of water will change depending on the temperature:

Water Temperature ($^{\circ}\text{C}$)	Density (g/cm^3)
0 (liquid)	0.9999
4	1.0000
20	0.9982
40	0.9922
60	0.9832
80	0.9718

Table 1: The variation of water density with temperature (Physical Geography.net 2004)

All density values are based on the density of water at 4°C (1g/cm³). The electronic densimeter used has a compensating water temperature feature allowing for the measurement to be taken at any measured temperature, after which instrument will automatically convert the reading to one taken at 4°C.

The densimeter has a minimum density resolution of 0.001g/cm³ and can measure a sample of up to 300 grams. It also calculates volume, allowing samples of various shapes to be used.

3.2 Magnetic Susceptibility

Magnetic susceptibility of a rock sample is determined by the amounts and susceptibilities of various magnetic materials the sample, and is primarily controlled by the amount of ferromagnetic minerals (Parasnis 1996). Magnetic susceptibility can only be measured on outcrops or on rock samples. It is not homogenous throughout the entire rock, therefore point measurements do not always give the bulk susceptibility of the rock (Telford et al. 1990).

Induced magnetization is defined by Telford et al (1990) as Eqn. 3:

$$I = H\kappa \quad (3)$$

where: H = geomagnetic field (A/m)

κ = the susceptibility of the sample (unitless)

I = induced magnetization (A/m)

A KT-9 Kappameter by Exploranium was used to measure magnetic susceptibility. The Kappameter uses a 10 kHz LC oscillator and an inductive coil (Exploranium 1997). The Kappameter manual outlines the steps taken by the unit during a measurement (Exploranium 1997):

1. The frequency of the oscillator is measured in free space.
2. The oscillator frequency is next measured when the coil is placed on a material of unknown susceptibility.
3. A frequency difference is measured that is directly proportional to the material's
4. susceptibility.
5. The susceptibility is calculated from this frequency difference

As stated earlier, the magnetic susceptibility of a material is not homogenous; therefore 10 measurements were taken at random locations on each sample. These readings are then automatically averaged and results are displayed in 10^{-3} SI units.

3.3 Remanent Magnetization

The geomagnetic field of the Earth has changed throughout the planet's history. The geomagnetic field can cause a small bias in the distribution of magnetic moments of ferromagnetic grains (Butler 1992). As a mineral is cooled through its Curie point, this bias in the magnetic moment is frozen into the mineral and can be retained over time. When measuring remanent magnetization we are in effect measuring the Earth's historical geomagnetic field. There are both primary and secondary types of remanent magnetization.

Primary effects occur during the formation/cooling of the rock and secondary effects occur after rock formation. In the case of kimberlites, the primary type of remanent magnetization is thermoremanent magnetization, which occurs during the cooling of kimberlite magmas from elevated temperatures. However, there are secondary effects that can alter the primary remanent magnetization (Butler 1992). These effects include exposure to lightning strikes, prolonged exposure to other geomagnetic fields, or chemical changes. These effects may change the primary remanent magnetization of the ferromagnetic mineral grains and affect their magnetic moments (Butler 1992).

Techniques for measuring remanent magnetization were first developed in the 1950's and continue to progress. The spinner magnetometer became the most widely used magnetometer in the late 1960's and is still in widespread use today. There are a variety of different types of spinner magnetometer, but all share common components (Butler 1992). A spinning shaft rotates the rock sample, and a magnetic field sensor is used to detect the oscillating magnetic field that is produced by the rotating magnetic moment of the sample (Butler 1992). The sensor sends out a signal, which is then passed to a phase sensitive detector that is designed to amplify signals at the rotation frequency of the spinning shaft (Butler 1992). For this project a spinner magnetometer called the MolSpin BigSpin was used to collect remanent magnetization values (Figure 3.2).



A= Power switch	F= Fluxgate and sample holder
B= Battery charger hook up	G= Lever to move the sample holder
C= Cable port to connect to computer	H= Fluxgate ring
D= Switch to Local if not using computer, Switch to R.S. 232 if using computer	I= Three screw that lock the fluxgate ring in place
E= Attenuator dial	

Figure 3.2: Picture of the BigSpin by MolSpin with a location key.

The BigSpin requires that all samples be securely fitted inside a 5 cm by 5 cm by 5 cm glass cube. This cube is placed on a cradle located inside a fluxgate. The sample is then spun. The BigSpin measures the magnetic moment of each of the three axes of a sample twice. In total, 6 spins are needed. The measurements have an accuracy of 0.035 mA/m. Since samples are small and of various shapes, their volumes were calculated using the densimeter described in Section 3.1. By using the magnetic moment data and the volume, the remanent magnetization as defined by Butler (1992) was calculated (Eqn. 4):

$$J = \frac{M}{v} \quad (4)$$

where: M = total magnetic moment (Am^2)
 v = the volume of the sample (m^3)
 J = remanent magnetization (A/m)

Due to a lack of core orientation during the time of drilling, the direction of the remanent magnetization could not be found. This information would have been valuable to this project. However, the magnetic intensity of the remanent magnetization can be used along with the magnetic susceptibility of each sample to find the Koenigsberger ratio.

3.3.1 Koenigsberger Ratio

To explore the effect of remanent magnetization in the area, the Koenigsberger ratio was evaluated. The Koenigsberger ratio is the ratio of remanent magnetization to induced magnetization in a rock sample (Eqn.5):

$$Q = \frac{J}{H\kappa} \quad (5)$$

where: J = remanent magnetization (A/m)
 H = Earths geomagnetic field (A/m)
 κ = magnetic susceptibility (unitless)
 Q = Koenigsberger Ratio (unitless)

A Koenigsberger ratio or Q-factor result greater than 1.0 suggests that remanent magnetization is at least just as important as the induced magnetization in a sample's resultant field in situ magnetization.

3.4 Resistivity

Resistivity defines a material's ability to resist the flow of an electric current and is measured in SI units of Ohm-m. Since conductivity is the inverse of resistivity, a conductor is defined as a material through which an electric current can easily flow (Telford et al. 1990). Resistivity is affected by the amount of water saturation, permeability and porosity of a rock. Ground water often contains a substantial ionic content and is much more conductive than an average rock sample so even minor amounts of saturation can greatly change a rock's resistivity. Temperature and pressure can also effect the measurement of resistivity. The relationship has not been accurately defined for most rocks but resistivity tends to decrease with burial depth as temperature and pressure increases (Telford et al. 1990). To reduce the temperature/saturation effects the collected samples were kept at a constant temperature and were saturated using a vacuum chamber. Once again, physical properties of the in situ water of each kimberlite pipe are unknown and distilled water from the Diavik mine site water system was used. Distilled water may not accurately reflect the in situ water composition but in the absence of any other data it is the fluid of choice.

The conductivity of the distilled water was measured using a Model 73 Engineered Systems & Designs Inc Conductivity/Temperature meter. Water input to the vacuum chamber measured at 0 μ -Siemens/meter, after saturating the samples the conductivity varied between 20 to 30 μ S/m. It is believed that this change is caused by ions freed from the rocks during the saturation process. Each rock type was saturated separately to ensure that increase in water conductivity did not contaminate different rock types.

Resistivity of a cylinder of core is defined by Telford et al. (1990) and as Eqn. 5:

$$R = \frac{VA}{lI} \quad (5)$$

where: R= resistivity (ohm-m)
l = length of core (m)
V= voltage across the sample (v)
A= cross-sectional area of the cylindrical core (π radius²) (m²)
I= current (amps)

Resistivity was measured in the laboratory using the following circuit described by Telford et al. (1990) and seen in Figure 3.3.

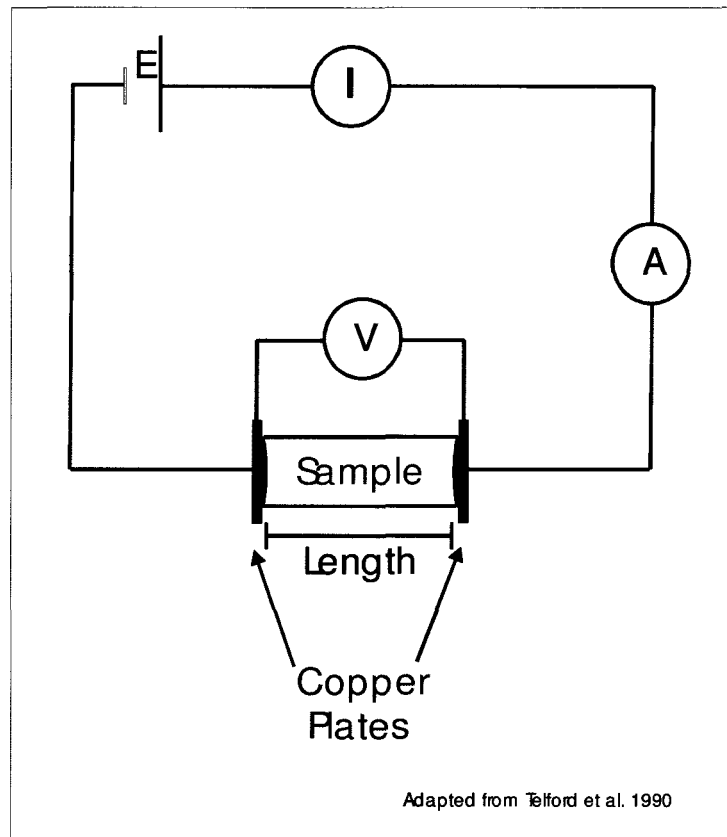


Figure 3.3: Circuit design that was used to measure the resistivity across a cylindrical core sample of a defined length. Note E represents the electricity source, I represents a function generator, V represents a voltmeter, and A represents an ammeter.

A BK Precision sweep function generator provided a DC power source, which was connected in series to a Trek high-voltage power amplifier (Figure 3.4). An ammeter set in series was used to measure current. To send current through the sample, copper plates were used as electrodes and were placed on the cut edges of the sample. Other conductors such as clay were also tried as electrodes. This method was ineffective as clay was very messy and not time efficient to apply or remove. Copper plates, in the end, were the most effective electrodes. All rock samples were cut using a rock saw, however, the faces of

the rock sample were not 100% smooth causing small air gaps between the rock and the copper electrodes which increased the contact resistance. To reduce this resistance, thin sponges soaked in copper sulfate solution were placed between the copper plates and rock sample. The copper plates, sponges and rock sample were then sandwiched together using a large plastic clamp. The voltage across the sample was measured using a Circuit-Test Electronics voltmeter with an impedance of 10M Ohms, attached in parallel to the copper plates. An image of this circuit can be seen in Figure 3.5



Figure 3.4: BK Precision sweep function generator and the Trek high-voltage power amplifier used to create the power source in the circuit.

Chapter 3: Physical Properties Under Stress

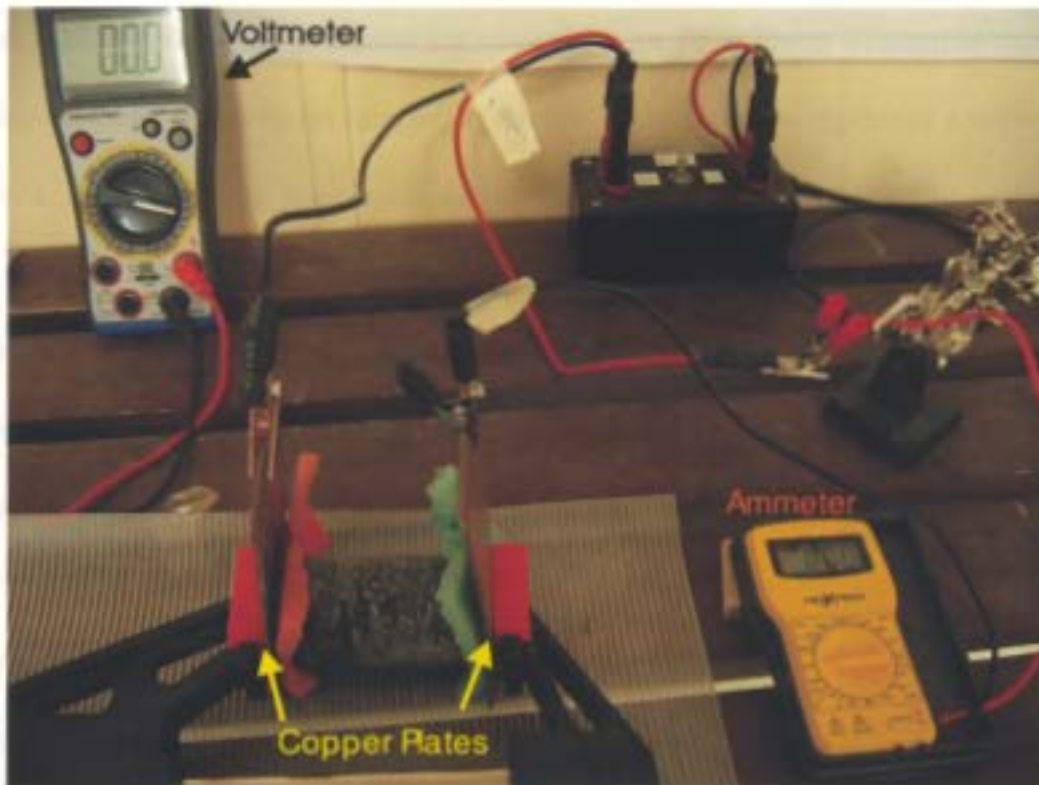


Figure 3.5: Resistivity measurement setup showing the core sample sandwiched between the damp sponges soaked in copper sulfate solution and copper plates. Current is sent through the sample via alligator clips that are attached to the copper plates. The voltage is measured by connecting the voltmeter in parallel across the copper plates.

Chapter 4: Physical Properties Data Analysis

In total, 400 samples were collected for analysis from 16 different kimberlite pipes. The locations of these pipes can be seen in Figure 4.1. These samples represent a subset of the host rock and kimberlite population of the Diavik area. Core availability and quality, along with time and money constraints, played large roles in which pipes and specific samples were selected. The objective of this chapter is to define physical property values that will be used to represent the Diavik area, and will be used to define and constrain forward models and inversions of magnetics and gravity data in Chapter 5.

4.1 Previous Kimberlite Physical Property Studies

Mwenifumbo et al. (1996) used borehole techniques to measure the geophysical characteristics of the Fort a la Corne Kimberlite in Saskatchewan and four kimberlites in Kirkland Lake area in Ontario. They concluded that even though the physical properties are variable within a pipe and also between pipes, geophysical data could be used to classify differences in zones and source material of kimberlites. They noted that the density and magnetic susceptibility values in kimberlites are higher than the surrounding host sediments (Mwenifumbo et al. 1996).

Katsube and Kjarsgaard's study in 1996 included 41 kimberlite samples from Northwest Territories, Saskatchewan, and Ontario. They measured density, porosity, resistivity, and magnetic susceptibility. They classified the samples into crater facies and hypabyssal facies, which throughout this thesis are referred to as crater and root zone. They

concluded that the hypabyssal facies had high bulk density and electrical resistivity, while the crater facies had low density and resistivity. They also found that magnetic susceptibility showed no relation to kimberlite facies. However, they did find a relationship between porosity and magnetic susceptibility for each facies.

4.2 Repeatability

Before conducting any statistical analysis on the collected data, it is important to ensure that measurements are repeatable. In a hypothetically perfect experiment, subsequent readings of the same physical property using the same equipment would give exactly the same results. In practice, small errors often creep into an experiment and change the values of subsequent repeated measurements. Errors in observations can be divided into the two groups: accidental and systematic errors (Topping 1969). Accidental errors are often due to small, random mistakes made by the observer, and these effects can be reduced by repeating measurements (Topping 1969). To help alleviate accidental errors great care and time was allowed to ensure each measurement was taken using the same systematic approach. The experimental controls used included constant air and water temperatures, vacuum and soaking times, and copper sulfate concentrations. Systematic errors can arise from the observer or the instrument. These errors have to do with observational procedure, and cannot be alleviated by repeating measurements (Topping, 1969). It is often very difficult to distinguish between these two types of error since any data error may be a combination of both types.

In order to test repeatability, 10 samples of each of the three rock types were measured twice. To compare repeated readings, the percent difference between two measurements was found by:

1. Calculating the absolute difference between each pair of readings
2. Dividing the absolute difference by the higher reading in each pair
3. Multiplying the result by 100 to express it as a percentage

4.2.1 Percent differences for Density

Physical Property	Rock Type	Repeated Measurements (g/cm ³)		Percent Difference (%)
Density	Host Rock	2.634	2.635	0.0379
		2.661	2.661	0
		2.684	2.682	0.0745
		2.621	2.621	0
		2.617	2.622	0.1906
		2.7	2.702	0.0740
		2.724	2.729	0.1832
		2.74	2.738	0.0729
		2.661	2.66	0.0375
		2.699	2.699	0
	Crater Zone	2.935	2.938	0.1021
		2.636	2.641	0.1893
		2.844	2.854	0.3503
		2.819	2.821	0.0708
		2.403	2.425	0.9072
		2.467	2.485	0.7243
		2.584	2.588	0.1546
		2.416	2.417	0.0413
	Root Zone	2.552	2.568	0.6230
		2.572	2.58	0.3100
		2.862	2.872	0.3481
		2.797	2.806	0.3207
		3.05	3.051	0.0327
		2.714	2.715	0.0368
		2.875	2.877	0.0695
		2.951	2.95	0.0338
		2.691	2.692	0.0371
2.879	2.878	0.0347		
2.846	2.849	0.1053		
2.859	2.853	0.2098		

Table 2: The repeated density measurement values and the percent difference for each pair. The mean percent difference in density for all rock types is extremely low at approximately 0.15%.

4.2.2 Percent Differences for Magnetic Susceptibility

Physical Property	Rock Type	Repeated Measurements (unitless)		Percent Difference (%)
Magnetic Susceptibility	Host Rock	0.00043	0.00035	18.60
		0.00057	0.00044	22.80
		0.00064	0.00059	7.81
		0.00023	0.00018	21.73
		0.00026	0.00026	0
		0.00025	0.00026	3.84
		0.00008	0.00005	37.5
		0.00029	0.00026	10.34
		0.00018	0.00016	9.44
		0.00045	0.00055	18.18
	Crater Zone	0.00328	0.00304	7.31
		0.0151	0.015	0.66
		0.00593	0.00694	14.55
		0.00434	0.0043	0.92
		0.00088	0.0008	9.09
		0.00255	0.00227	10.98
		0.00186	0.00188	1.06
		0.00099	0.00084	15.15
		0.00109	0.00104	4.58
		0.00122	0.00145	15.86
	Root Zone	0.0138	0.014	1.42
		0.00581	0.00554	4.64
		0.0161	0.0178	9.55
		0.013	0.0131	0.76
		0.0154	0.0158	2.53
		0.013	0.0133	2.25
		0.00208	0.00215	3.25
0.00983		0.00982	0.10	
0.00573		0.00534	6.80	
0.0042	0.00433	3.00		

Table 3: The repeated measurement values and percent difference results for each pair of magnetic susceptibility measurements tested. The percent difference in magnetic susceptibility for all rock types is less than 10% for most readings. The host rock and crater zone have a larger percentage difference than the root zone. As discussed in Section 3.2 of Chapter 3, susceptibility is inhomogeneous throughout the entire rock. This inhomogeneity could be more dominant in host rock and crater zone samples than the root zone samples due to their characteristically inhomogeneous compositions. Based on the results of the repeated samples, all data measurements are considered repeatable within 10%.

4.2.3 Percent Differences for Remanent Magnetization

Physical Property	Rock Type	Repeated Measurements (A/m)		Percent Difference (%)
Remanent Magnetization	Host Rock	9.99E-05	0.00012	16.54
		0.000087	0.000193	54.89
		0.000106	0.000169	37.5
		8.21E-05	9.03E-05	9.08
		0.000102	0.00013	21.36
		0.008593	0.007668	10.76
		0.017922	0.017447	2.64
		0.000014	0.0002	26.35
		0.000109	8.66E-05	20.47
		8.24E-05	0.000151	45.35
	Crater Zone	0.050385	0.049721	1.31
		0.024923	0.025114	0.758
		0.048424	0.048135	0.597
		0.012405	0.01194	3.74
		0.058481	0.056396	3.56
		0.004783	0.004625	3.29
		0.278573	0.273197	1.92
		0.055238	0.05406	2.13
		0.016207	0.016448	1.46
		0.0008	0.000715	10.59
	Root Zone	0.200624	0.224995	10.83
		0.158588	0.219542	27.76
		0.023282	0.028734	18.97
		0.092343	0.091855	0.528
		0.208364	0.210465	0.99
		0.161103	0.166151	3.04
		0.081369	0.079186	2.68
0.054879		0.054482	0.72	
0.230824	0.394202	41.44		
0.436102	0.478024	8.76		

Table 4: The repeated measurement values and the percent difference results of each pair of remanent magnetization measurement tested. The percent difference in remanent magnetization for all rock types is less than 25%.

4.2.4 Percent Differences for Resistivity

Physical Property	Rock Type	Repeated Measurements (ohm-m)		Percent Difference (%)
Resistivity	Host Rock	11524.77	11572.20	0.409
		14070.79	12404.07	11.84
		520.80	508.74	2.31
		1261.35	1142.16	9.45
		1678.52	1571.00	6.41
		7811.65	7305.93	6.47
		13874.86	12587.50	9.27
		20017.11	17611.93	12.01
		14904.52	17260.59	13.65
	4601.39	4568.32	0.71	
	Crater Zone	5737.13	5414.00	5.63
		132.52	133.61	0.81
		687.96	626.52	8.93
		983.72	935.82	4.87
		1969.46	1860.08	5.55
		1045.35	854.68	18.23
		1449.35	1376.12	5.05
		3609.65	3810.84	5.27
		538.614	762.91	29.40
	1026.92	1113.45	7.77	
	Root Zone	1284.74	1124.57	12.46
		586.76	534.26	8.95
		7509.83	7185.28	4.32
		250.65	232.73	7.14
		188.69	204.97	7.94
		725.00	691.99	4.55
		734.90	670.52	8.76
12829.50		11292.79	11.97	
2733.08		2495.44	8.69	
675.17	731.25	7.67		

Table 5: The repeated measurement values and the percent difference results of each pair of resistivity measurements. Since the percent difference in resistivity samples measured is less than 10% for most readings, all resistivity measurements will be considered to be repeatable within 10% of each other.

4.2.5 Repeatability Discussion:

From the percent difference results (Table 6), the measurements taken during this project are believed to be repeatable within reasonable error. The remanent magnetization results are the least repeatable, the cause of which is believed to be slight movements by the sample while spinning. Efforts were made to avoid this, however, it was difficult to ensure all samples were 100% secure. The low variance in the repeatability of density, (the most repeatable of all measurements) and the magnetic susceptibility and resistivity measurements, are believed to be caused by a combination of the accuracy of the instrument used and the systematic approach followed during data collection.

Measurement	Percent Difference
Density	0.15%
Remanent Magnetization	Less than 25%
Magnetic Susceptibility	Less than 10%
Resistivity	Less than 10%

Table 6: Representative repeatability results for each measurement

4.3 Physical Property Values: Initial Conclusions

The raw data collected can be seen in table form in *Appendix A*. All collected data are shown as histograms with normal curves in Figures 4.2 to 4.5 and includes data collected from all 16 pipes.

By inspecting the trends in the histograms for density (Figure 4.2), remanent magnetization (Figure 4.3) and magnetic susceptibility (Figure 4.4), it can be seen that

the range of data is larger for the kimberlite zones than that of the host rock zone. It is assumed that this increased range is caused by heterogeneous mineral distributions within the kimberlite zones, and the heterogeneous inclusions of foreign material introduced to the kimberlite crater zone during the eruption process and subsequent resedimentation.

By inspecting the ranges on the resistivity histograms (Figure 4.5) an opposite trend can be seen; the host rock zone has a larger range than that of the kimberlite zones. This could be an effect of the three local rock types which are all included in the host rock classification system. Each rock type likely has a different resistivity range. The degree of weathering of the host rocks could also cause this range difference. An increase in weathering throughout the host rocks samples would increase the amount of fractures causing an increase in porosity and saturation. As discussed in Section 3.4, porosity, permeability, and saturation can dramatically affect resistivity. This increased weathering is unlikely to be homogenous throughout the area, and may explain the variable in the resistivity values from sample to sample.

The results in Table 7 display the mean values of each physical property for each rock type for all 16 kimberlite pipes. Whether rock types zones can be distinguished from one another during a geophysical survey is predominantly due to their physical property contrasts. In general, the larger the contrast between two rock types the easier their signatures will be to differentiate in survey data. The densities of the host rock and root zone are very similar, while the crater zone density is comparatively lower. It is assumed

from this density contrast and from the usual location of the crater zone (close to the surface) that there is potential to distinguish between host rock and crater zone during a gravity survey. However, it is not felt that the contrast between the root zone and host rock shows the same potential. Both remanent magnetization and magnetic susceptibility show an order of magnitude difference between each rock type and therefore show great potential for differentiating the different rock groups. In addition, resistivity measurements also show a variation between each rock type with a large difference between host and kimberlite values.

Physical Property	Host			Crater			Root		
	N	Std. Dev	Mean	N	Std. Dev	Mean	N	Std. Dev	Mean
Density (g/cm ³)	187	0.0565	2.67	98	0.1271	2.51	40	0.1656	2.65
Remanent Magnetization (A/m)	175	0.382	0.0497	96	0.801	0.538	36	1.526	2.046
Magnetic Susceptibility (unitless)	190	3.043e-4	1.497e-4	136	0.005	0.0027	54	0.0126	0.0169
Resistivity (ohm-meters)	86	9021.72	8994.32	32	1671.53	1638.12	12	3327.75	2230.9

Table 7: Statistical summary of the physical property values for all kimberlite pipes, where N represents sample size and Std. Dev represents standard deviation.

4.4 Comparing Pipe A154N to All Other Pipes

Pipe A154N, one of the 16 pipes used during data collection, is currently being mined. Due to its economic nature, it has been the subject of many drill programs in order to construct mining plans. As a result of this drilling the geometry of this pipe is well defined and Diavik has constructed a geology model of this pipe. This model, along with

collected physical property data can be used to perform inversions and forward models. Pipe A154N will be the focus of an investigation into the relationship between physical properties and geophysical signatures, in Chapter 5. Before using the physical properties of pipe A154N, statistical analysis was carried out on this and the other 15-kimberlite pipe to show that the physical property values of pipe A154N are considered representative of all pipes in the Diavik area. This was performed by constructing histograms for each rock type and physical property for pipe A154N and all other pipes (as seen in Figures 4.6 to 4.9) and by comparing the mean values for each histogram.

4.4.1 Comparison: Discussion and Conclusions

The physical property results for each of the kimberlite pipes excluding A154N will not be discussed independently during this thesis due to small sample sizes. Instead they will be considered as representative samples of all the Diavik kimberlites and will be analyzed together as one data group. Attention should be drawn to the fact that approximately 50% of all samples collected came from pipe A154N due to the availability of core from this pipe. Sample sizes of less than 10 will not be considered statically relevant therefore will not be used for comparison. It should be noted that the values for the combination of all other pipes will have larger data ranges in the data than the values in the pipe A154N category since this data was collected from multiple pipes located throughout the Diavik area (Figure 4.1).

By comparing the density, remanent magnetization, and magnetic susceptibility results seen in Figures 4.6, 4.7 and 4.8 respectively, it can be concluded that physical property values for pipe A154N are within similar orders of magnitude to those from all other pipes. There are three exceptions to this statement, including the density of the root zone, and the remanent magnetization and magnetic susceptibility of the host rock. The density differences seen in the root zone were unexpected. The average value for pipe A154N is 2.80 g/cm^3 but the average of the other pipes is 2.66 g/cm^3 . This results in a much lower density contrast between host rock and root zone kimberlite for all other pipes.

The differences seen in both magnetic properties for host rock are considered to be caused by three different rock types being lumped together into the host rock group. Two of the three rock types included in this group (Section 2.3.1) have distinct magnetic signatures. The distribution of these three rock types throughout the survey area may lead to the observed widely varying magnetic properties for host rock.

Due to the small sample sizes of the kimberlite zones, no conclusions can be drawn from the comparison of kimberlite resistivity values. This is a major problem for root zone resistivity measures as it was difficult to find core samples which were the appropriate shape in order to measure. The host rock resistivity samples show an order of magnitude difference between pipe A154N and the other 15 pipes. This difference is once again suspected to be caused by the three independent rock types included in the host rock

group, and (Subsection 4.3.1). Inhomogeneous weathering may also be contributing to this difference.

Based on the previous comparison, and with several noted exceptions, the physical property values of pipe A154N are comparable to the values of the 15 other kimberlite pipes sampled in the Diavik area. The A154N values have distinct advantages over the combined data from all other sampled pipes: they are taken from a large number of samples, possess a smaller range of values, and appear to be closer to normally distributed. Consequently, the physical property values for pipe A154N will be used throughout the following investigation to represent mean values for host rock, crater zone, and root zone physical properties.

4.5 Testing Correlations

The correlation of both density and depth with various physical properties was tested for all rock types. Data from all samples was divided into two categories: those samples from pipe A154N and those samples from all other pipes. This was done to help compare dependence ratios in pipe A154N with the other kimberlite pipes in the area. Correlations are used to measure how strongly related two parameters are to one another (Devore 2004). There are several different methods available to calculate correlations, with each method generating slightly different results. Two standard methods are the Pearson and Spearman. The Pearson is used only if data is normally distributed as it relies on the mean of the dataset. When the mean is used, anomalous or extreme values can bias the

results. The Spearman method, in contrast, works on normally and non-normally distributed datasets because it does not take the mean into account (Davis 2002). This method separates both sets of data by numerically ranking and then correlates these ranks (Davis 2002). Since not all of the physical property measurements taken for pipe A154N and the other 15 pipes are considered normally distributed, the Spearman method was used.

The Spearman method is based upon Spearman's ranking correlation coefficient test, which indicates the monotonic correlation/dependence of ranked bivariate datasets (Hays and Winkler 1970) It is given in Eqn 6 (Davis 2002):

$$\rho = 1 - \frac{6 \sum_{i=1}^n [R(x_i) - R(y_i)]^2}{n(n^2 - 1)} \quad (6)$$

where : $R(x_i)$ and $R(y_i)$ = the ranking of each dataset

n = number of data variables in each dataset

ρ = ranking coefficient

In general, positive values indicate that the bivariate relationship is monotonically-increasing and negative values indicate the relation is monotonically-decreasing (Hay and Winkler 1970). The Spearman correlation coefficient, ρ , ranges from 1 to -1, with 1 or -1 indicating a perfect positive or negative correlation and zero indicating no correlation. The strength of the relationship can be broken down into three groups: weak correlation ($\rho < 0.4$), medium correlation ($0.4 < \rho < 0.7$) and strong correlation ($\rho > 0.7$). The same

categories exist for the negative relationships except that the ranges are negative. Please note that these groupings are intended only as “rule of thumb” ranges for correlation strength.

A confidence interval, or level of confidence, can also be associated with the correlation coefficient. A confidence interval reports an interval within which the calculated value is plausible (Davis 2002). In general, the higher the confidence interval value, the more like the result will be repeated. The statistical program Statistics Package for the Social Sciences graduate package 15.0 (SPSS 2006) was used to conduct Spearman correlation test on all datasets. This program marks values with a confidence level of 95% with an asterix (*) and 99% with double asterices (**). The same symbols will be used here.

4.5.1 Correlation Testing: Density vs. Physical Properties

The Spearman correlation test was used to test the monotonic function dependence of each physical property against density for data from Pipe A154N, along with the other 15 sampled kimberlite pipes. The data relating to each test was also plotted to gain a visual understanding into each relationship (Figures 4.10, 4.11 and 4.12).

The relationship between density and remanent magnetization (Figure 4.10) for all rock types is one of weak dependence. Both the host rock cases have positive dependencies and have a confidence level of 99% and 95% respectively. The crater zone results indicate a positive dependence with a 95% confidence for pipe A154N, but a negative

dependence with no assigned confidence level for the other pipes. The root zone results show a negative weak dependence without an assigned confidence level for both categories.

The correlation between density and magnetic susceptibility (Figure 4.11), shows the host rock as having a medium positive dependence with a confidence level of 99% for both pipe A154N and the other 15 pipes categories. Both kimberlite zones for pipe A154N have a medium positive correlation with density; the associated confidence level for the crater zone is 99%. The results for the other 15 pipes are somewhat different with both kimberlite zones showing a weak correlation with density, though the crater zone dependence is positive and the root zone dependence is negative.

The last property to be tested against density was resistivity (Figure 4.12). Both pipe A154N and the other 15 pipe categories show the host rock as having a weak positive correlation. The crater zone results for pipe A154N predict a positive weak correlation, however, for the other 15 pipes category, the sample size for the crater zone was too small to draw conclusions about correlation. As seen in Subsection 4.4.1, the sample sizes for the root zone kimberlite are also too low to be considered significant for both categories.

4.5.2 Density Correlations Conclusions

In general, statistical results with a confidence level of 95 to 99% are considered statistically significant. It is assumed that test results with these levels accurately represent the true relationships between density and the other physical properties (Table 8).

Rock Type	Remanent Magnetization		Magnetic Susceptibility		Resistivity	
	Pipe A154N	All Other Pipes	Pipe A154N	All Other Pipes	Pipe A154N	All Other Pipes
Host	Weak [*]	Weak [*]	Medium ^{**}	Medium ^{**}	Weak [*]	Weak
Crater	Weak [*]	Negative Weak	Medium ^{**}	Weak	Weak [*]	N/A
Root	Negative Weak [*]	Negative Weak	Medium	Negative Weak	N/A	N/A

Table 8: Summary of the Spearman rank test results for the relationship between density and all other physical properties. Asterisks indicate the associated confidence level, where one asterisk equals 95% confidence level and two-asterisk equal 99% confidence level. The green highlighted results indicate the correlation decided for each case.

By reviewing Table 8, there are several cases where the two pipe categories show different results. When this occurs, the case with a higher associated confidence interval is chosen as the correlation result. For example, in the case of the crater zone remanent magnetization, the pipe A154N category displays a positive weak result with a confidence level of 95% whereas the other 15 pipes category describes the relationship as a negative weak one with no confidence level. Since the pipe A154N has a higher confidence level this result will be chosen as the representative correlation. In cases were neither categories has an associated confidence interval, the data scatter plots were reviewed. The category with the smallest dispersion is chosen to represent the correlation

relationship. An example of this is seen with the relationship between density and magnetic susceptibility for the root zone. By reviewing Figure 4.11, it is clear that the scatter of the other 15 pipes values are much more dispersed than the pipe A154N values, therefore the correlation result for pipe A154N was chosen.

The Spearman correlation results predict a weak positive correlation for both remanent magnetization and resistivity against density for both the host rock and crater zone. There is a negative weak dependence predicted for the root zone remanent magnetization. The relationship of all rocks for magnetic susceptibility vs. density is predicted as being a medium positive dependence. This correlation is related to the magnetic minerals that are causing the magnetic susceptibility response. Mafic rocks trend to be denser and more magnetic which maybe the reason for this correlation.

4.5.3 Correlation Testing: Depth vs. Physical Properties

All samples were collected from various depths, making it possible to ascertain whether any of the physical properties correlate with depth. If a physical property shows a strong dependence with depth it will play an important role in assigning values to any geophysical model. All depth measurements were taken relative to the depth below the surface in meters. It should be noted that according to core logs there is crater zone rock type found deeper than the root zone in pipe A154N. It was decided to keep these samples as crater zone. Recall that the kimberlite model seen in Section 2.4.2 is a

generalized model and the in sections of these zones are not as clear cut as shown in Figure 2.6.

Test results for the ranking of density and depth show a slight negative correlation for host rock, crater zone and root zone for both categories. One notable exception is the root zone in the other pipes category, which shows a medium negative correlation (Figure 4.13). The host rock correlation between depth and remanent magnetization (Figure 4.14) shows a medium negative correlation with a confidence level of 99% for pipe A154N, however, the 15 other pipes indicate a weak negative correlation with no confidence level. The crater zone results for both categories predict a negative medium correlation. On the other hand, the root zone results indicate that the density of pipe A154N has a weak negative correlation with depth while the other 15 pipes predict a medium positive depth dependence with a confidence level of 95%.

The results of the test between depth and magnetic susceptibility (Figure 4.15) reveals the host rock of pipe A154N as having a negative medium dependence with a confidence level of 99% and a host rock in the 15 other pipes category as having a weak negative dependence. The crater zone also displays a medium negative correlation for pipe A154N with a confidence level of 99%. The other 15 pipes category displays a positive weak correlation. The root zone results show a medium positive correlation with depth for all other pipes with a confidence level of 99%. The relationship between depth and resistivity shows a medium positive dependence with a confidence level of 99% for both host rock and crater zone for pipe A154N (Figure 4.16). The root zone results for both

categories and the crater zone for the other 15 pipes both have a non-significant number of samples and therefore are not considered to be relevant.

4.5.4 Depth Correlations Conclusions:

The same requirements for statistical relevance used in Subsection 4.5.2 apply here. The relationships between depth and each physical property are listed in Table 9.

Rock Type	Density		Remanent Magnetization		Magnetic Susceptibility		Resistivity	
	Pipe A154N	All Other Pipes	Pipe A154N	All Other Pipes	Pipe A154N	All Other Pipes	Pipe A154N	All Other Pipes
Host	Negative Weak	Negative Weak	Negative Medium	Negative Weak	Negative Medium	Negative Weak	Medium	Negative Weak
Crater	Negative Weak	Negative Weak	Negative Weak	Negative Weak	Negative Medium	Weak	Medium	N/A
Root	Negative Weak	Negative Medium	Negative Weak	Medium	Medium	Medium**	N/A	N/A

Table 9: Results by correlation strength for each physical property and rock type. Asterisks indicate the associated confidence level, where one asterisk indicates a 95% confidence level and two-asterics indicates a 99% confidence level. The green highlighted results indicate the correlation decided upon for each case.

Once again, when both categories for the same rock type show different results the case with a larger assigned confidence level is considered to represent the more accurate result. From the results of the Spearman rank tests between depth and physical properties it is expected that there is no correlation between depth and density for both the host rock and crater zone. The root zone displays differing results for each category; since neither result has an associated confidence level a visual inspection of their scatter plots (Figure 4.13) was performed. The root zone values for pipe A154N are more clustered

than the other 15 pipes and therefore its result of a weak negative correlation is taken as correct. Remanent magnetization vs. depth is expected to have a medium negative relationship for host rock, a weak negative correlation for the crater zone and a medium positive correlation for the root zone due to their respective confidence intervals. Magnetic susceptibility is predicted to have a medium positive dependence for both host rock and crater zone and a medium negative dependence for the root zone. Due to small sample sizes, the correlation for root zone vs. resistivity is unknown. However, resistivity correlation vs. depth for host rock and crater zone is a positive medium one.

4.5.5 Final Note on Correlation Testing

By comparing the results of both correlation tests it can be concluded that the majority of correlation results are drawn from pipe A154N. As seen in Section 4.4 combined data from the other 15 pipes in the area has a larger range in values. The larger range causes a larger dispersion in the data, making it harder for the Spearman rank test to assign confidence levels. There is one exception where a correlation value was taken from the of the other 15 pipes category over the pipe A154N category. This was the correlation between depth and remanent magnetization in the root zone. Since the bulk of the conclusions were based on A154N it is felt that this strengthens the argument that this pipe is representative of all sampled pipes in the Diavik area.

It should be noted that the medium strength predictions suggest that there is dependence between those aforementioned physical properties. This will be kept in mind when

making models for pipe A154N. It should be stressed, however, that there is no evidence to support a “strong” correlation between any of the measured physical properties with depth or density.

4.6 Comparison of Previous Studies to this Study

The results from pipe A154N from this study can be generalized in a few sentences; the kimberlite zones have a higher remanent magnetization, higher magnetic susceptibility and higher resistivity values than host rock, while the density for host rock is lower than root zone kimberlite and higher than crater zone kimberlite. By comparing the kimberlite zones, the zones can be classified: the crater zone has a lower density, lower remanent magnetization, and lower magnetic susceptibility. The resistivity could not be compared between zones due to low sample sizes in the root zone.

The results of this study, compared to the previous studies conducted by Mwenifumbo et al. (1996) and Katsube and Kjarsgaard (1996), show similarities between the analysis for all three rock groups. Since the exact values for the previous studies were not listed the values measured cannot be compared, however the relative values of each study can be.

This comparison is performed in the following tables:

Kimberlite vs. Host Rock

	Kennedy	Mwenifumbo et al.
Density	Lower Crater Higher Root	Higher
Magnetic Susceptibility	Higher	Higher

Table 10: The relative relationships between physical properties of kimberlite and host rock in Mwenifumbo et al. (1996) were found to be similar to those presented during this study.

Crater Zone vs. Root Zone

	Kennedy	Katsube and Kjarsgaard
Density	Lower	Lower
Magnetic Susceptibility	Lower	No relation
Resistivity	N/A	Lower

Table 11: The relative relationship between the physical properties of the two kimberlite zones collected in this study seems to agree with Katsube and Kjarsgaard (1996) results. They however found that there was no relation between the magnetic susceptibility of the crater and root zone, which was not case during this study. The resistivity relationship could not be defined due to the small sample size.

4.6.1 Previous Results: Discussion and Conclusions

By comparing the pervious results from studies performed by Mwenifumbo et al. (1996) and Katsube and Kjarsgaard (1996) to this study the results do vary somewhat. The density differences seen when comparing kimberlites with host rocks could be related to the different host rock present at each location. Also the lack of distinction between the magnetic susceptibility values of the crater and root zone kimberlites in Katsube and

Kjarsgaard's study may simply be due to a difference due to differences in kimberlite magma with each location.

It is believed that the physical property values given in this thesis are accurate values for the Diavik area. Each kimberlite field is different and should be considered independent of other kimberlite fields.

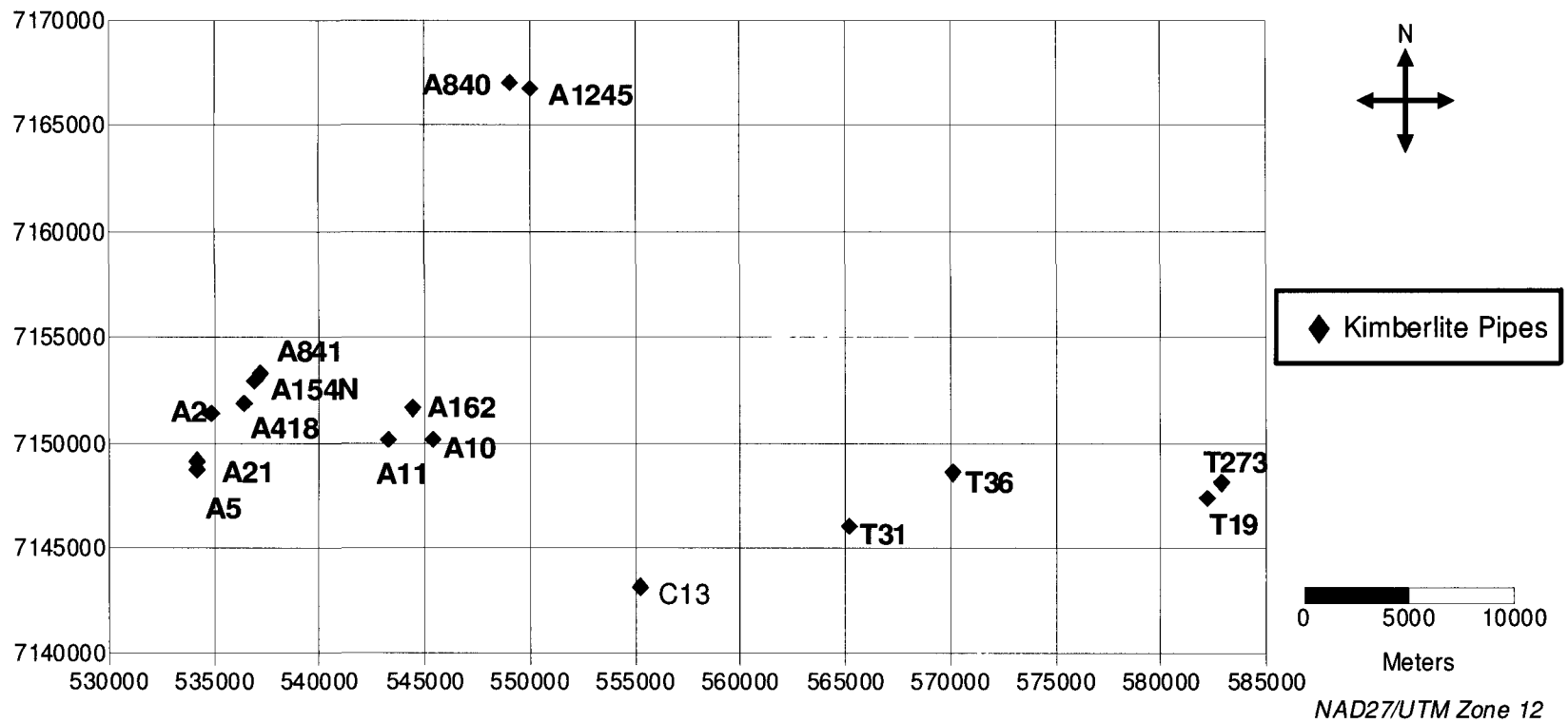


Figure 4.1: Map with locations of the 16-kimberlite pipes used for data collection. Red diamonds indicate the locations of kimberlite pipes.

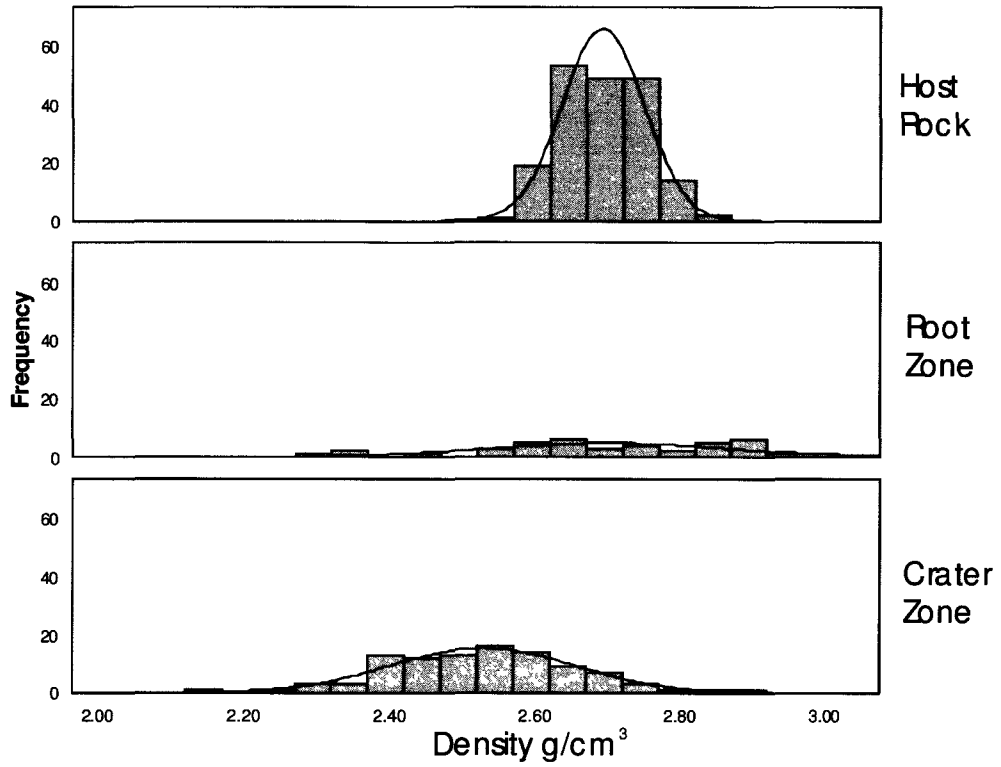


Figure 4.2: Density measurements for each rock type with normal distribution curves. The host rock and crater zone values are normally distributed whereas the root zone data is not.

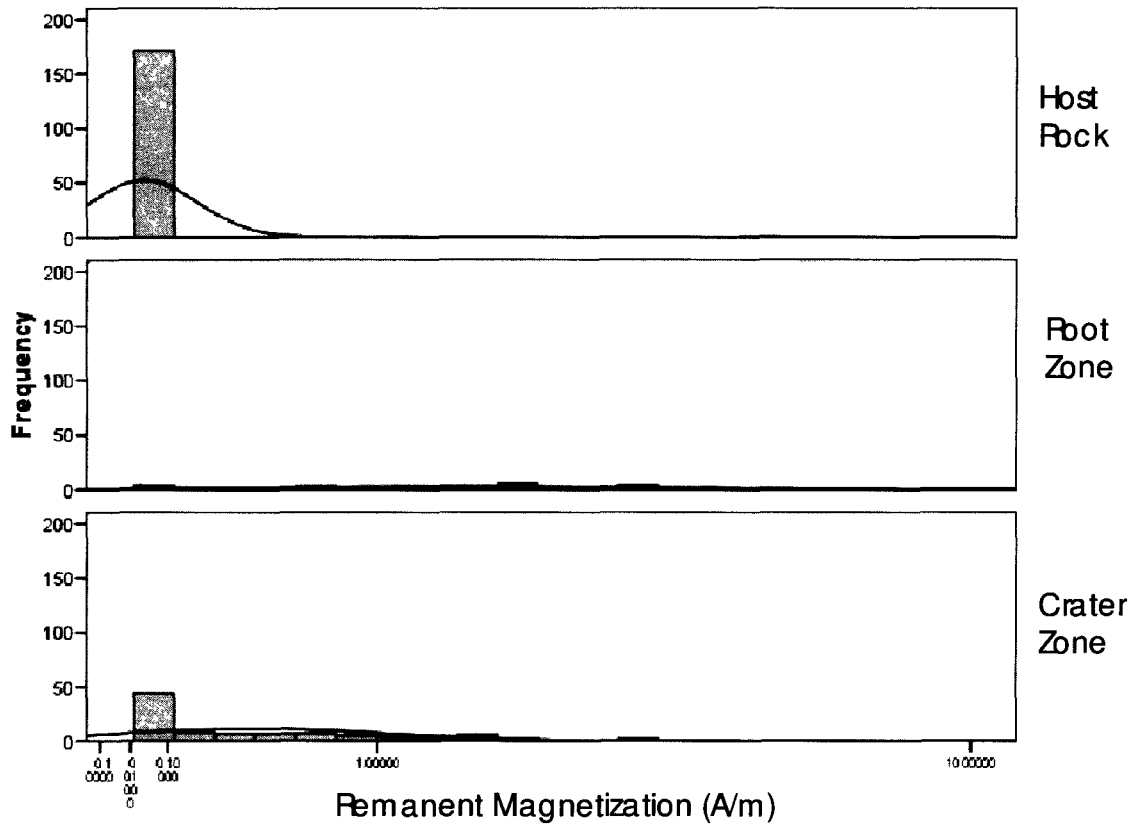


Figure 4.3: Remanent magnetization measurements for each rock type with normal distribution curves. None of the histograms show normally distributed data.

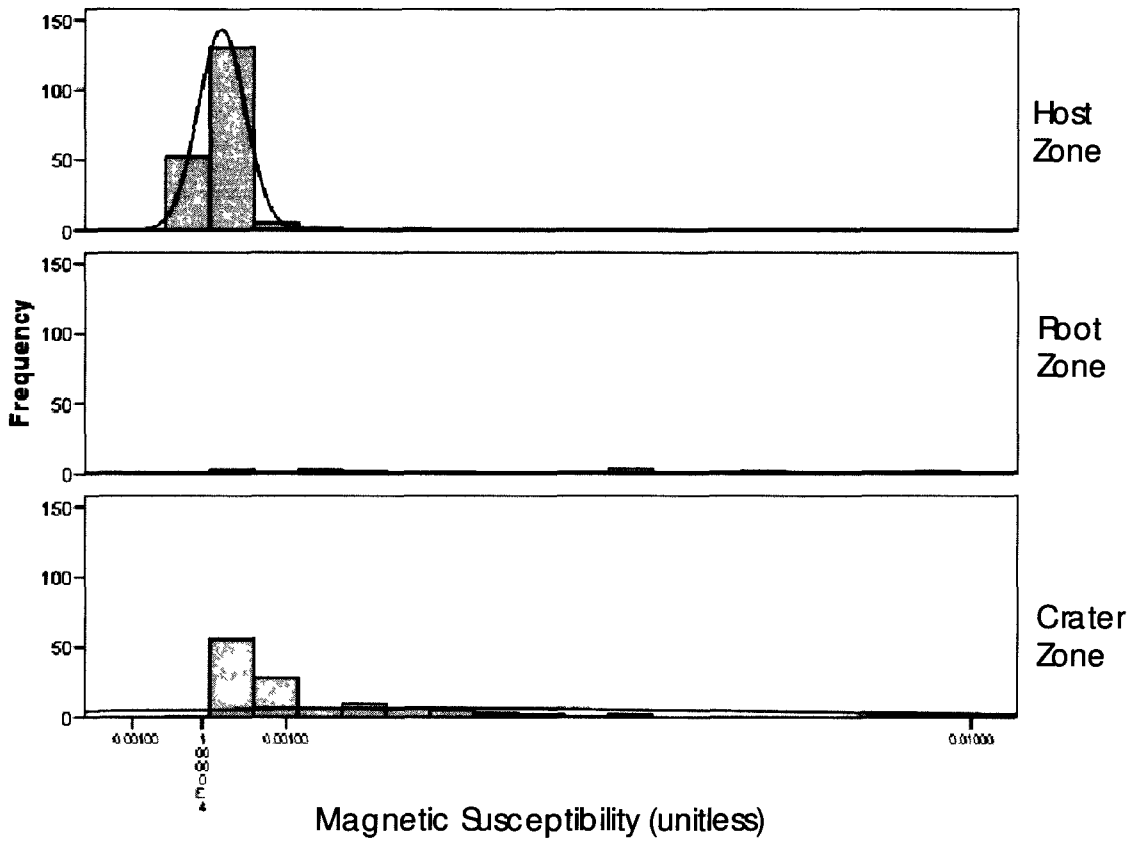


Figure 4.4: Magnetic Susceptibility measurements for each rock type with normal distribution curves. It appears that none of the magnetic susceptibility data is normally distributed.

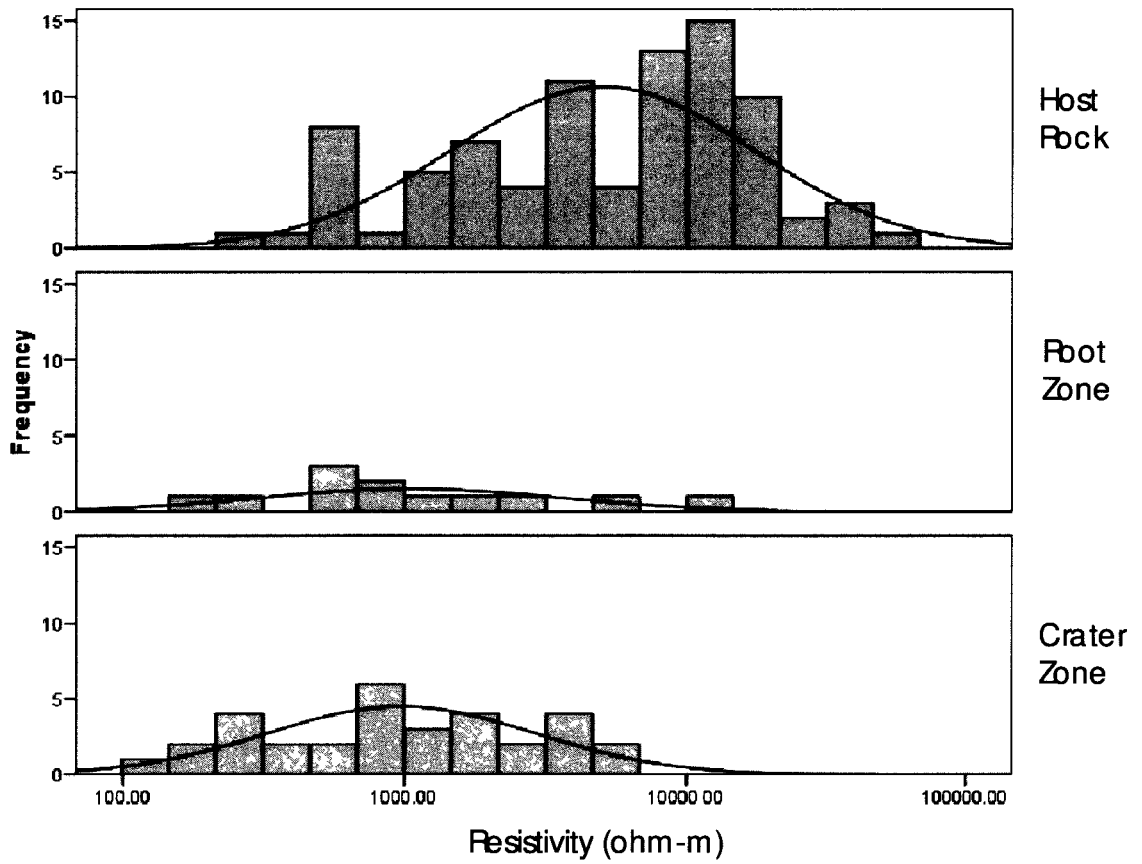
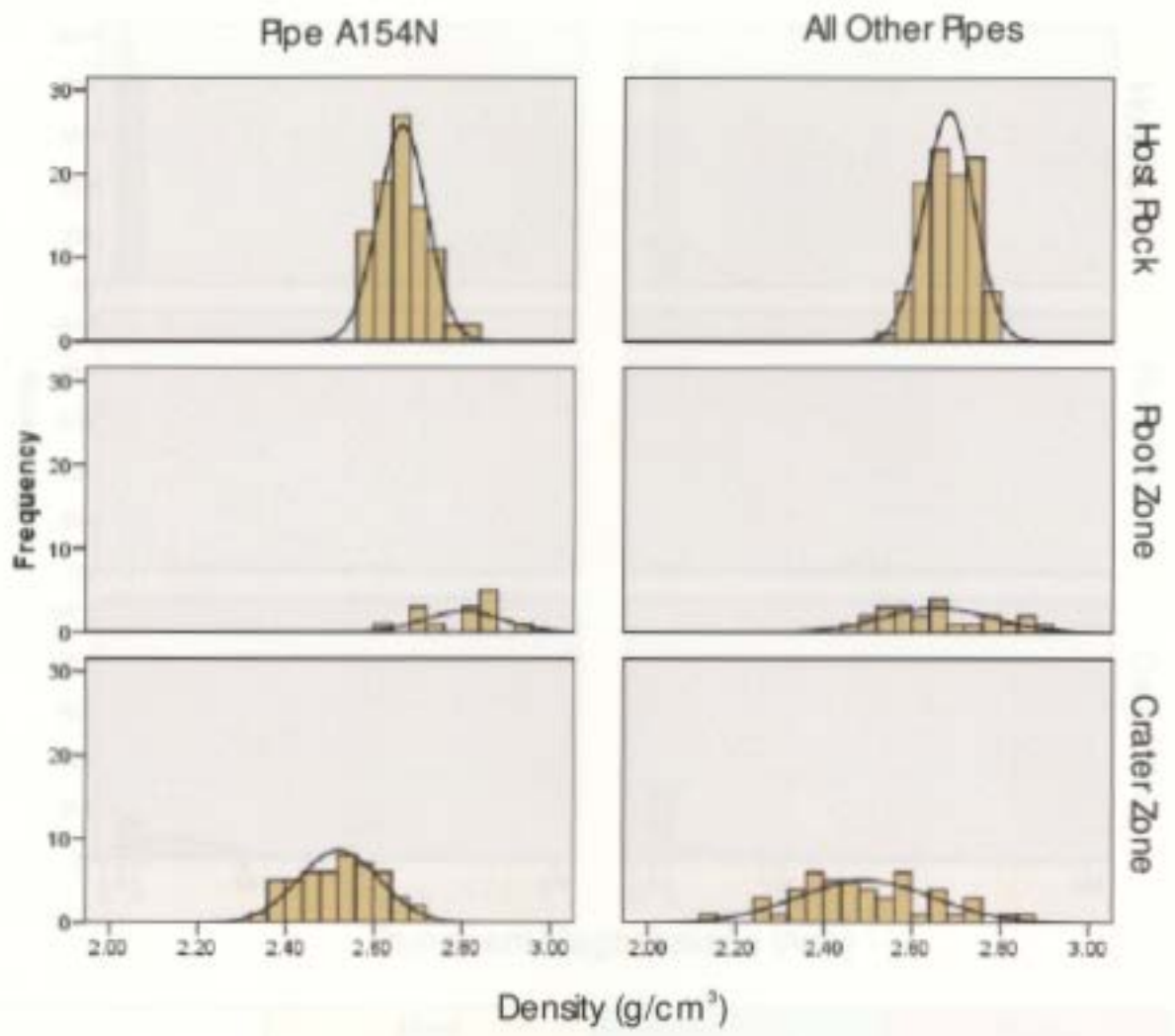
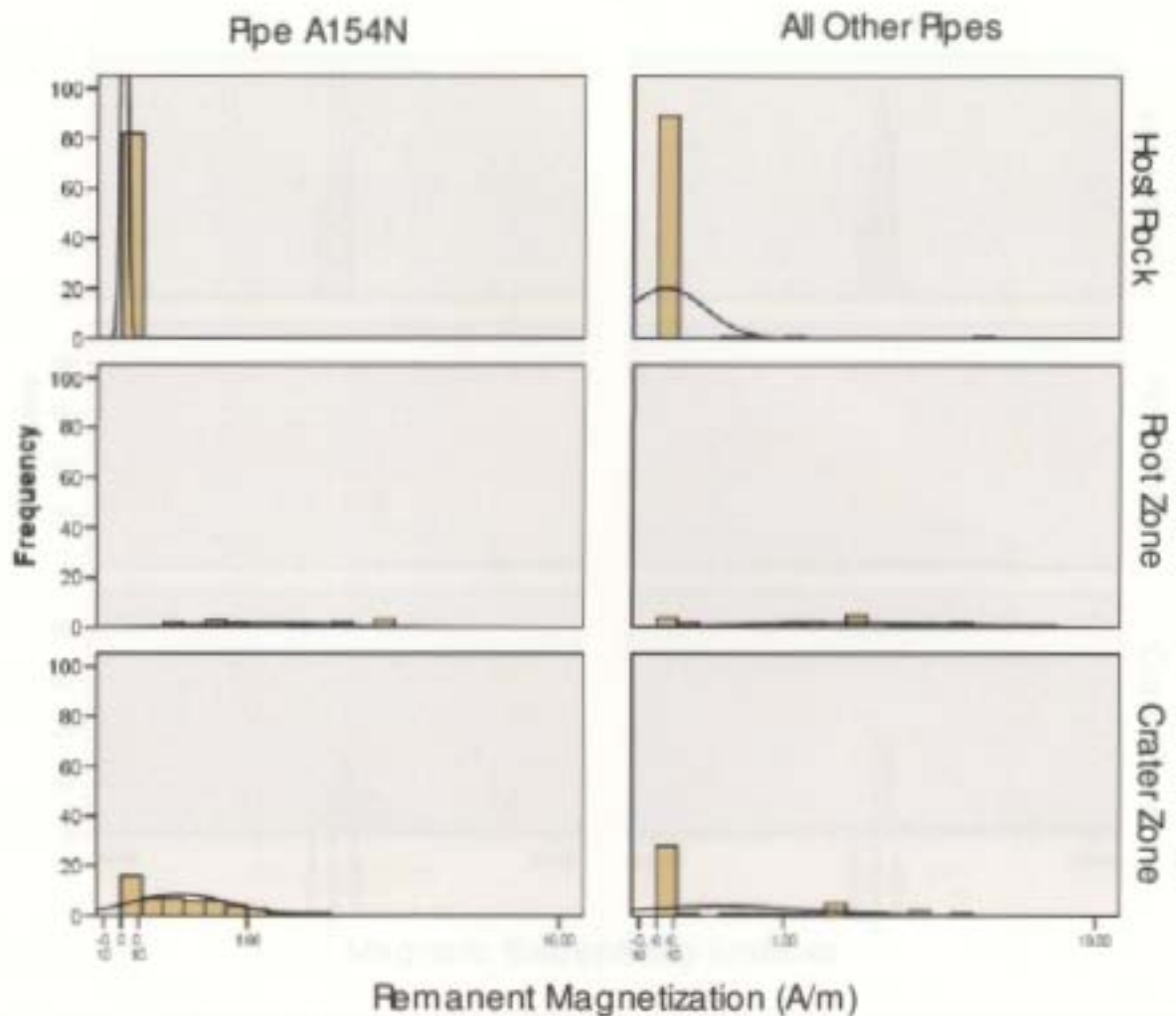


Figure 4.5: Resistivity measurements for each rock type displayed on histograms with normal distribution curves. The host rock, root zone and crater zone data seems to be somewhat normally distributed



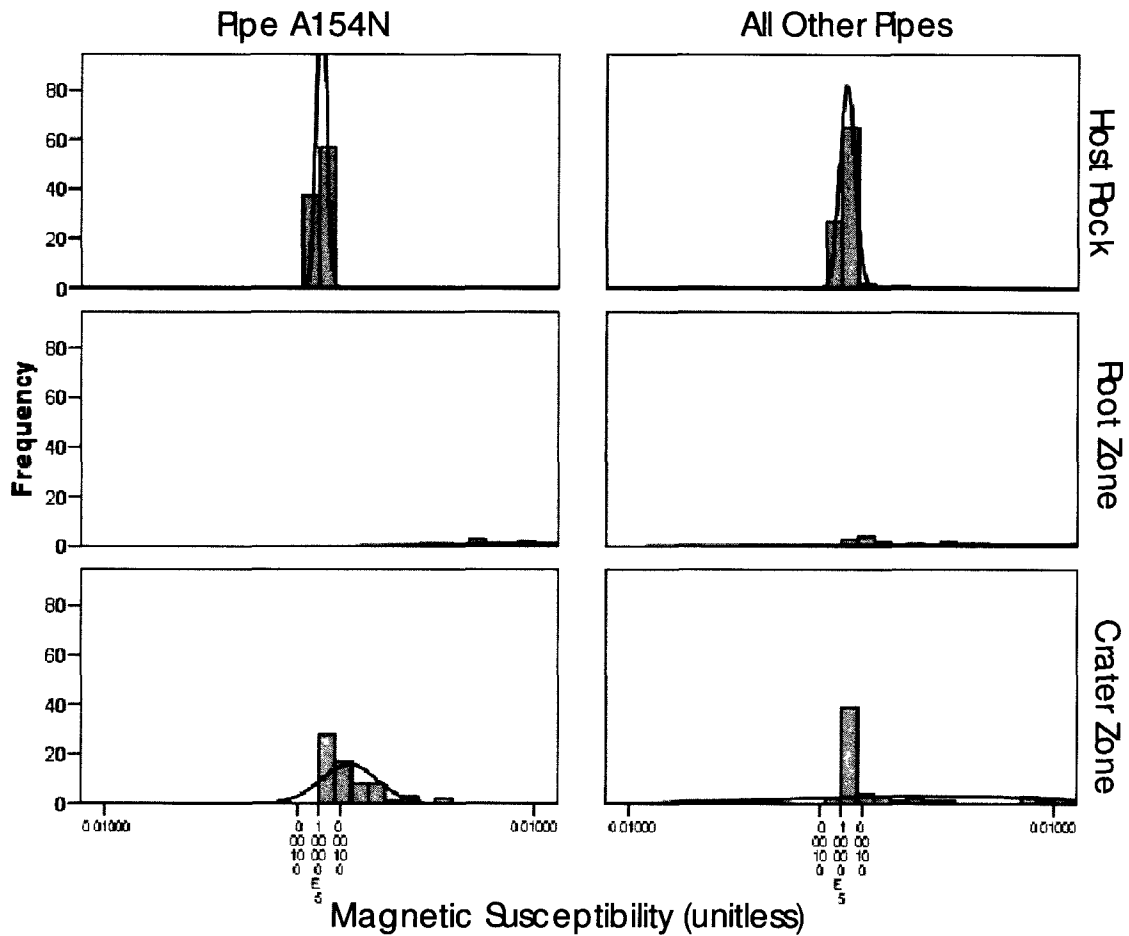
Density (g/cm ³)	Host		Crater		Root	
	Pipe A154N	All Other Pipes	Pipe A154N	All Other Pipes	Pipe A154N	All Other Pipes
N	90	97	49	49	14	23
Std. Dev	0.0556	0.0563	0.0910	0.1578	.0896	.125
Mean	2.66	2.68	2.52	2.49	2.80	2.66

Figure 4.6: Density histograms for both Pipe A154N and all other pipes with each rock type. The table at the bottom of the figure is a statistical summary of both categories; the summary includes sample size (N), standard deviation (Std. Dev), and mean. With the exception of the root zone, the host rock and crater densities are similar in both categories. Note that the histograms show a normal distribution curves with the pipe A154N data being more normally distributed than the all other pipes category.



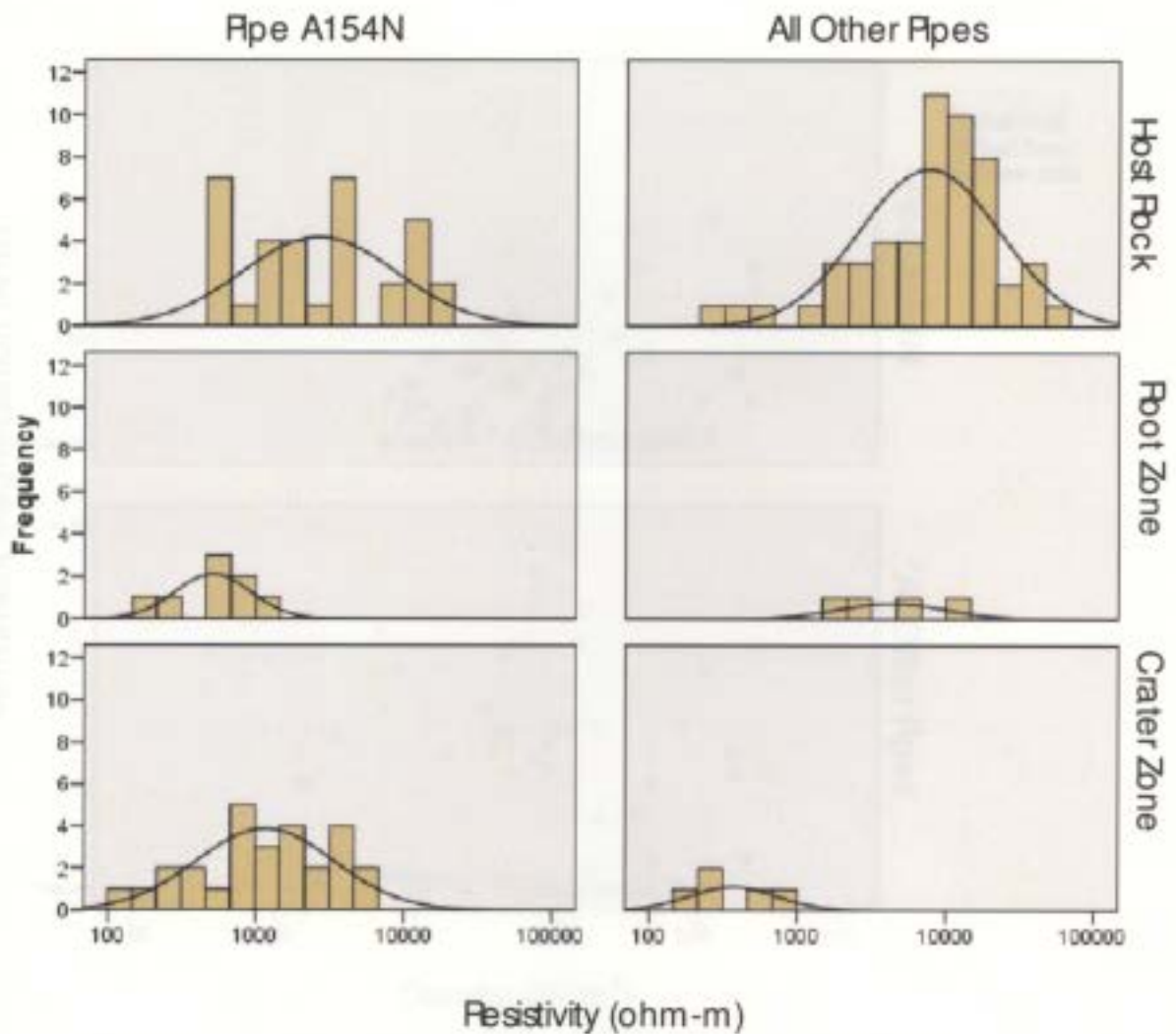
Remanent Magnetization (A/m)	Host		Crater		Root	
	Pipe A154N	All Other Pipes	Pipe A154N	All Other Pipes	Pipe A154N	All Other Pipes
N	82	93	52	44	14	24
Std. Dev	0.0173	0.5228	0.4394	1.077	1.11	2.10
Mean	0.0091	.0860	0.4340	0.6623	1.47	2.38

Figure 4.7: Remanent magnetization values for pipe A154N and all other pipes. Values are represented in histograms with the normal distribution curves. Except for the pipe A154N crater zone, none of the data seems to be normally distributed. The table at the bottom of the figure represents a statistical summary of both categories, which includes sample size (N), standard deviation (Std. Dev), and mean. By comparing the mean values it seems that the kimberlite zones are comparable with in the same order of magnitude whereas the host rock mean values are off by an order of magnitude. This difference is believed to be caused by the three different rock type groups that are included in the host rock group.



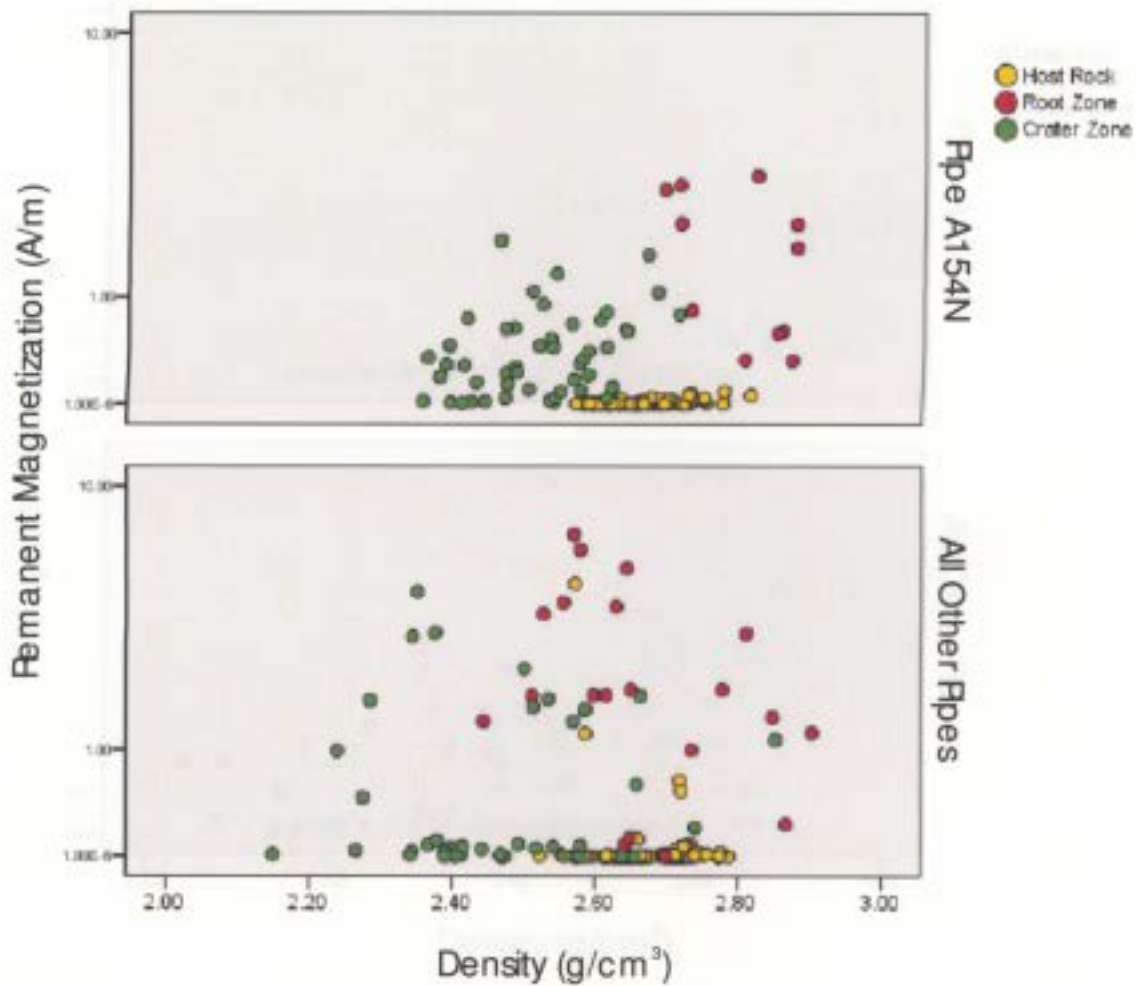
Magnetic Susceptibility (unitless)	Host		Crater	
	Pipe A154N	All Other Pipes	Pipe A154N	All Other Pipes
N	94	96	67	69
Std. Dev	.0002	.00035	.00130	.00665
Mean	.00008	.0002	.0014	.0041

Figure 4.8: Magnetic susceptibility histograms for both Pipe A154N and all other pipes with each rock type. The table at the bottom of the figure is a statistical summary of both categories; the summary includes sample size (N), standard deviation (Std. Dev), and mean. With the exception of the host rock mean values, the root zone and crater zone densities are comparable in both categories with the same orders of magnitude. Note that the histograms show a normal distribution curves with the pipe A154N data being more normally distributed than the all other pipes category.



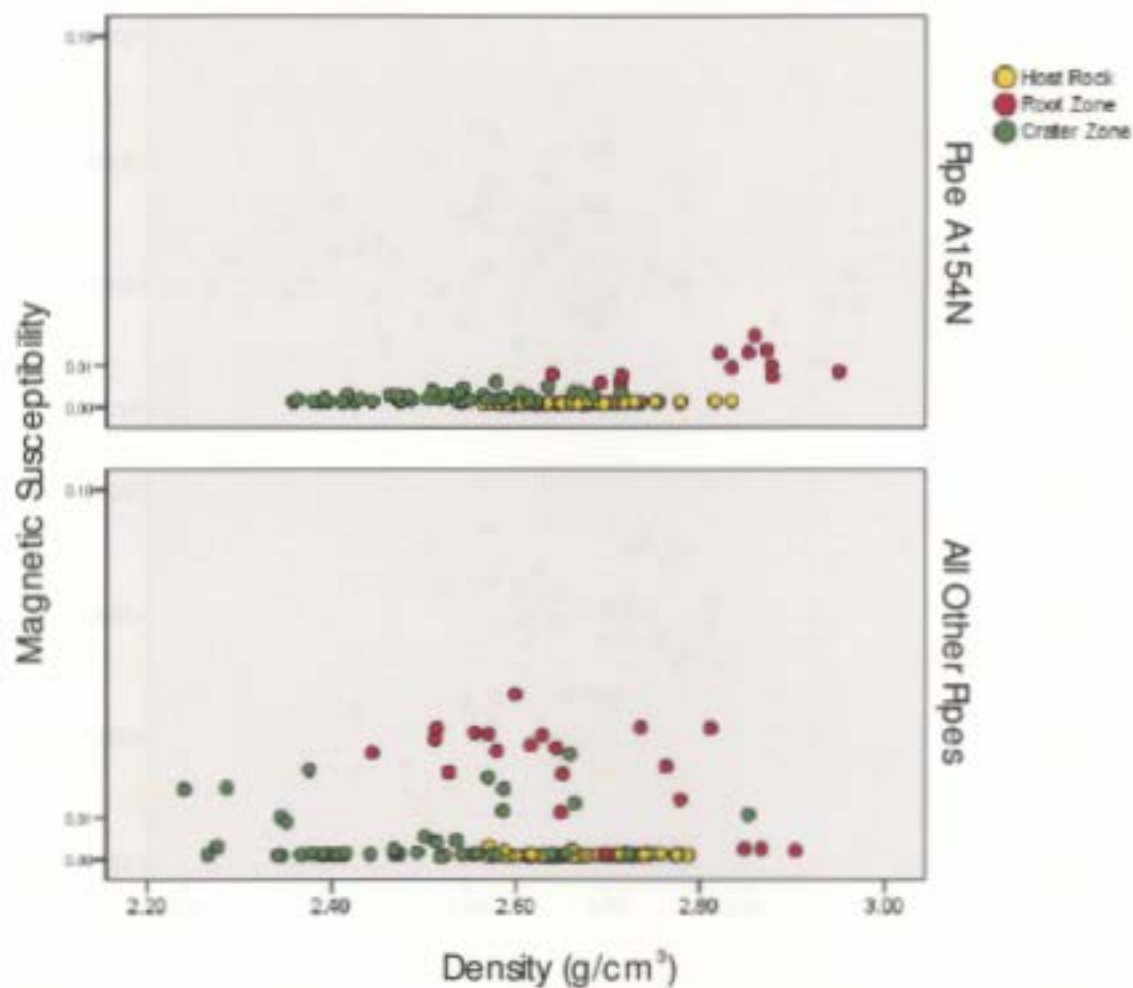
Resistivity (ohm-m)	Host		Crater		Root	
	Pipe A154N	All Other Pipes	Pipe A154N	All Other Pipes	Pipe A154N	All Other Pipes
N	33	53	27	5	8	4
Std. Dev	5480.49	9893.42	1730.09	325.11	296.3	4321.79
Mean	4969.6	11500.29	1858.19	449.77	583.1	5526.4

Figure 4.9: Resistivity values for pipe A154N and all other pipes and are represented in histograms with the normal distribution curves. The table at the bottom of the figure represents a statistical summary of both categories, which includes sample size (N), standard deviation (Std. Dev), and mean. Due a small sample size the resistivity of the kimberlite zones a comparison cannot be made. The differences seen in the host rock zone are believed to be caused by the different rock types placed in the host rock group.



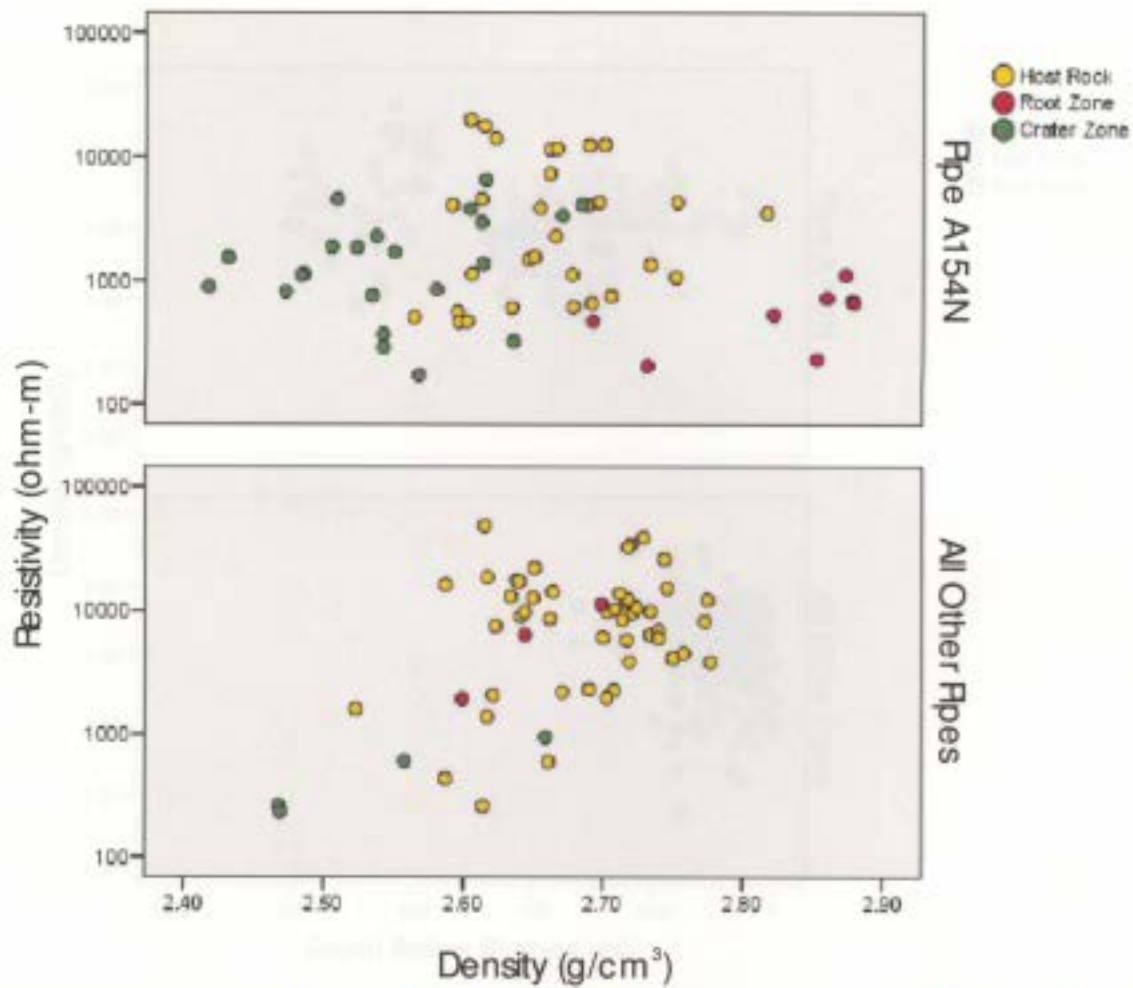
Density vs. Remanent Magnetization	Host		Crater		Root	
	Pipe A154N	All Other Pipes	Pipe A154N	All Other Pipes	Pipe A154N	All Other Pipes
Correlation Coefficient	.373 ^{***}	.256 [*]	.303 [*]	-.026	-.315	-.226
Number of Samples	79	92	47	44	12	24

Figure 4.10: Scatter plot and Spearman statistical results for density vs. remanent magnetization for pipe A154N and the other pipes. Note asterisks indicated associated confidence level.



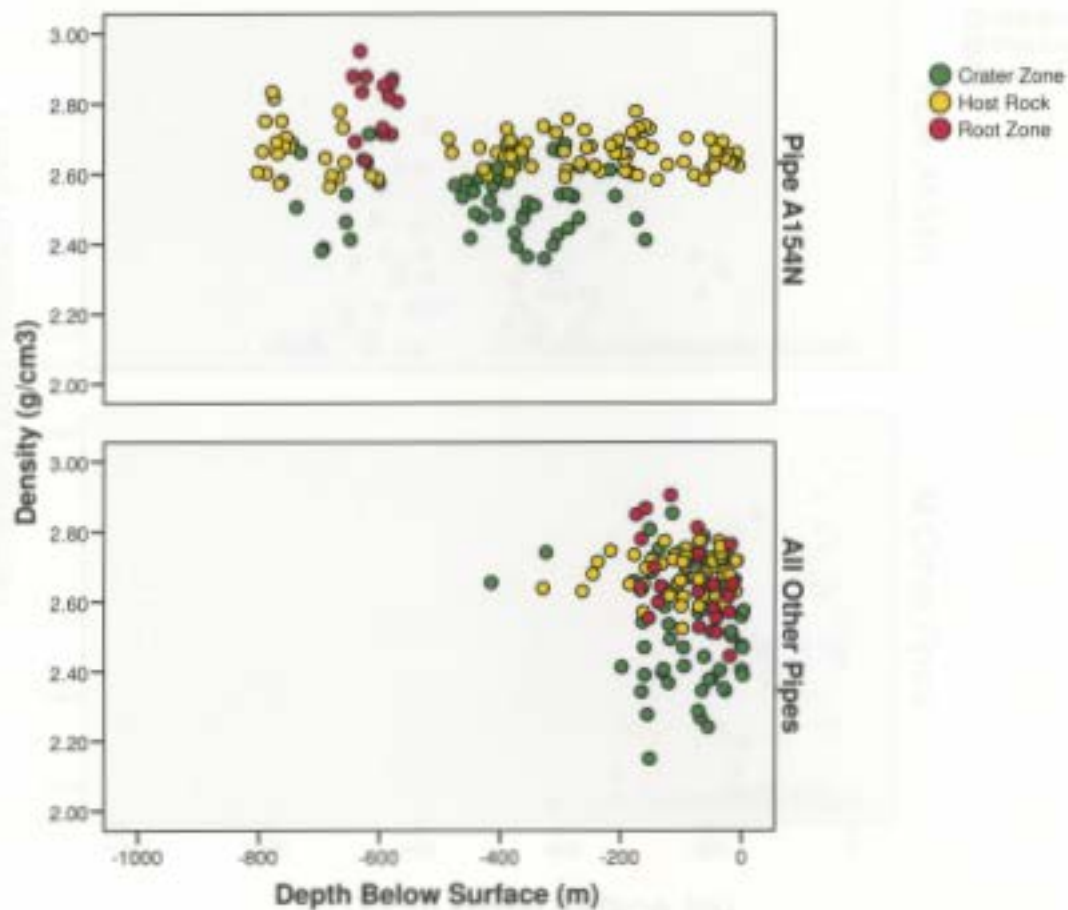
Density vs. Magnetic Susceptibility	Host		Crater		Root	
	Pipe A154N	All Other Pipes	Pipe A154N	All Other Pipes	Pipe A154N	All Other Pipes
Correlation Coefficient	.612**	.580**	.477**	.144	.413	-.276
Number of Samples	81	88	47	42	12	26

Figure 4.11: Scatter plot and Spearman statistical results for density vs. magnetic susceptibility for pipe A154N and the other pipes. Note asterisks indicated associated confidence level.



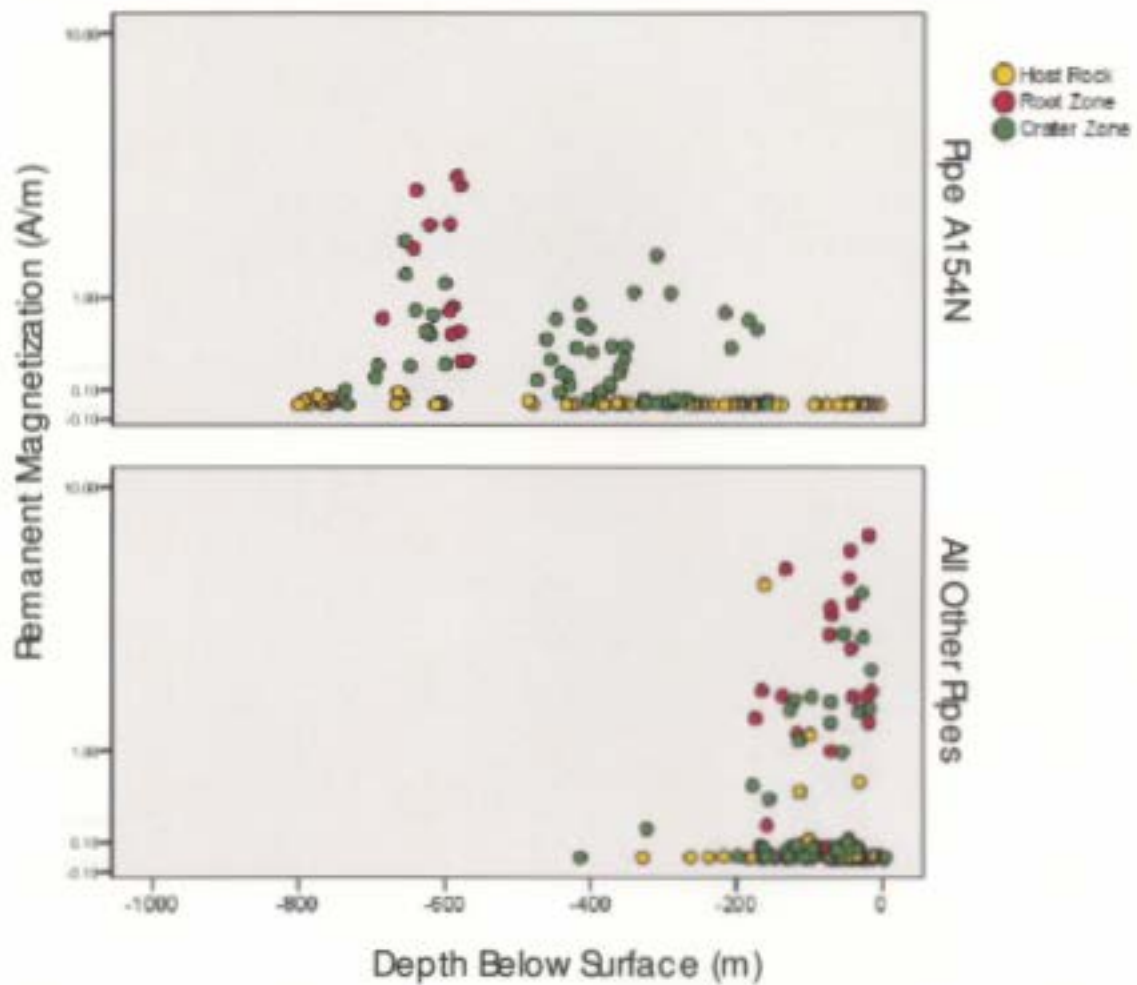
Density vs. Resistivity	Host		Crater		Root	
	Pipe A154N	All Other Pipes	Pipe A154N	All Other Pipes	Pipe A154N	All Other Pipes
Correlation Coefficient	.161	.089	.254	.8	.667	1.00 ^{***}
Number of Samples	30	50	22	4	8	3

Figure 4.12: Scatter plot and Spearman statistical results for density vs. resistivity for pipe A154N and the other pipes. Note asterisks indicated associated confidence level.



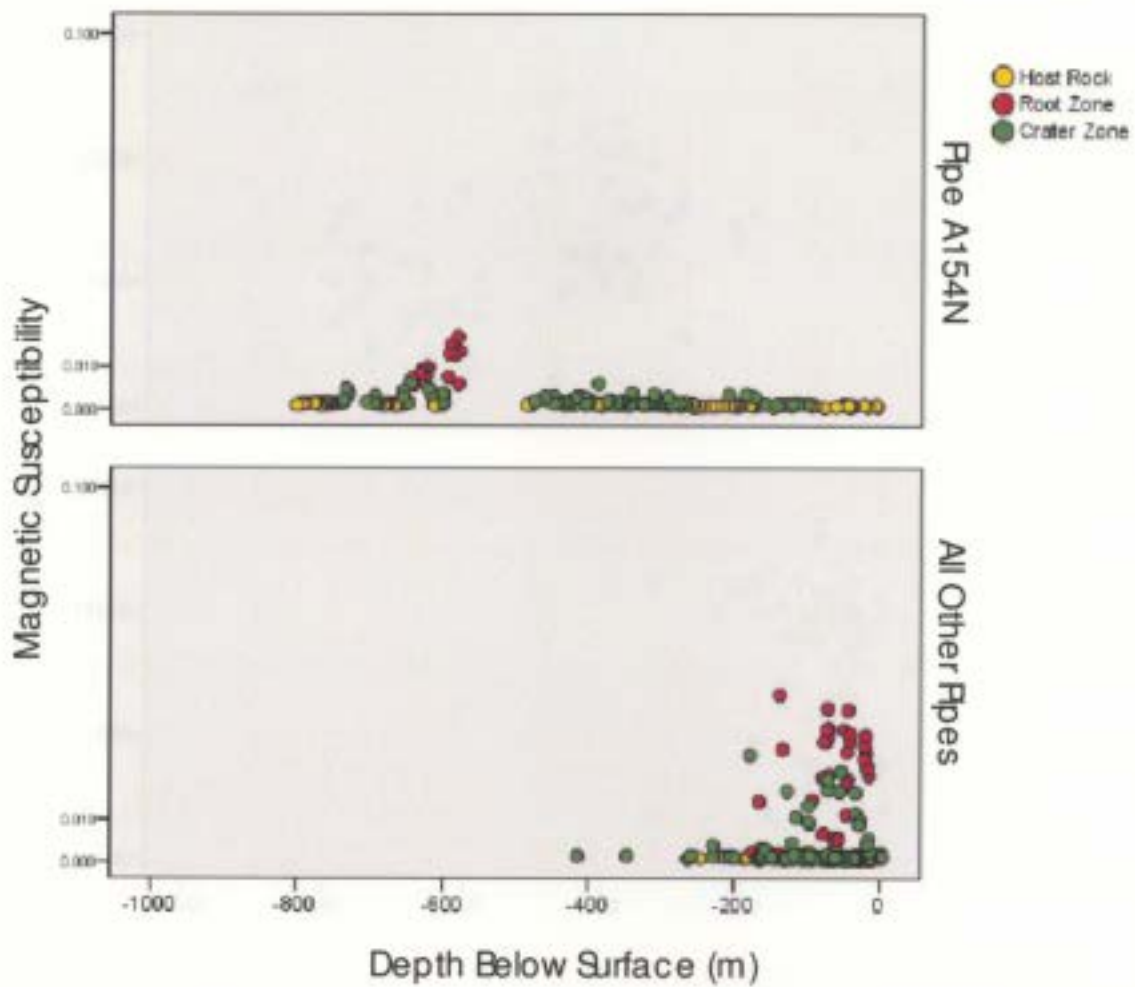
Depth vs. Density	Host		Crater		Root	
	Pipe A154N	All Other Pipes	Pipe A154N	All Other Pipes	Pipe A154N	All Other Pipes
Correlation Coefficient	-.058	-.015	-.102	-.223	-.124	-.435
Number of Samples	90	97	49	49	14	23

Figure 4.13: Scatter plot and Spearman statistical results for depth vs. density for pipe A154N and the other pipes. It should be noted that in pipe A154N that some crater zone material has been found deeper than the root zone material. Note asterisks indicated associated confidence level.



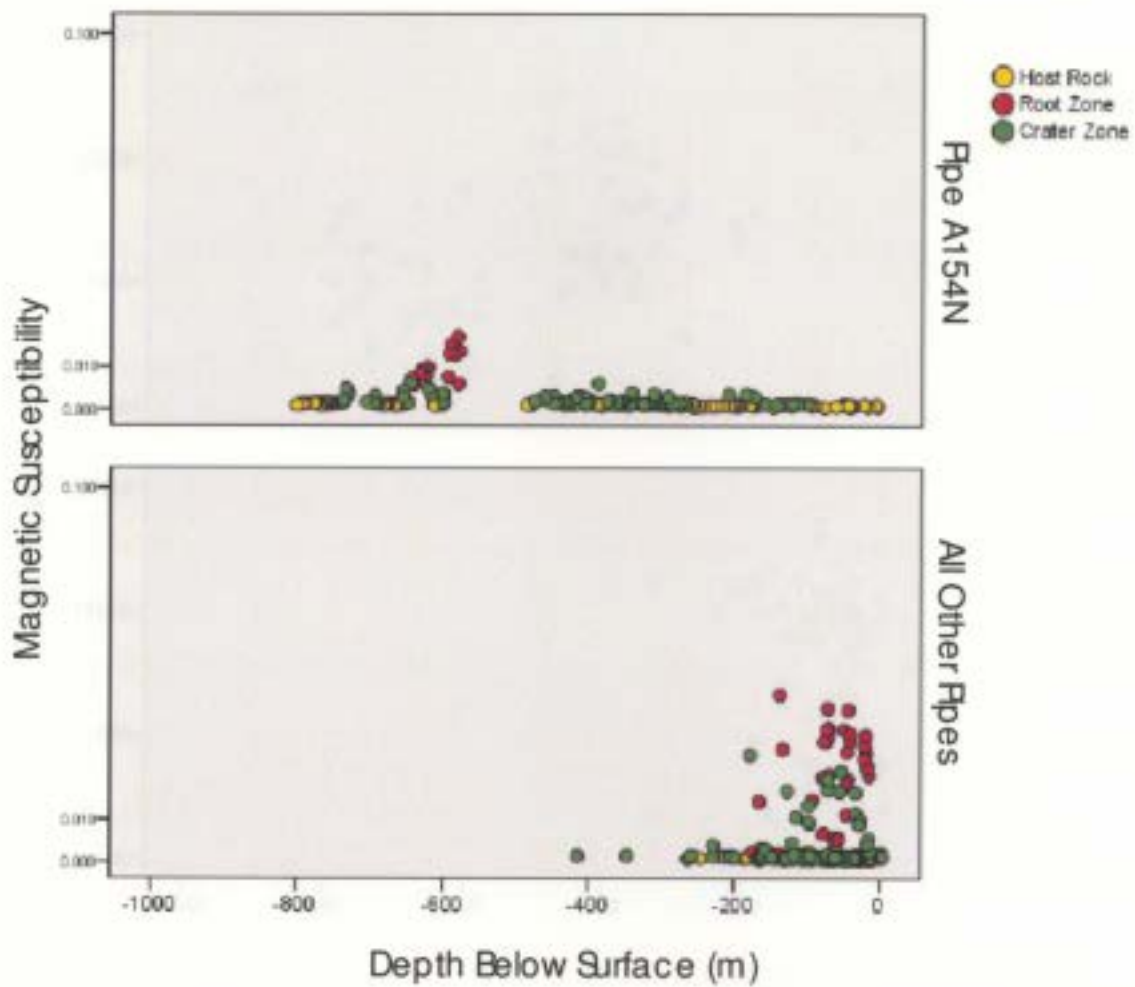
Depth vs. Remanent Magnetization	Host		Crater		Root	
	Pipe A154N	All Other Pipes	Pipe A154N	All Other Pipes	Pipe A154N	All Other Pipes
Correlation Coefficient	-0.517**	-.057	-.226	-.020	-.270	.429*
Number of Samples	82	92	52	44	14	24

Figure 4.14: Scatter plot and Spearman statistical results for depth vs. remanent magnetization for pipe A154N and the other pipes. It should be noted that in pipe A154N that some crater zone material has been found deeper than the root zone material. Note asterisks indicated associated confidence level.



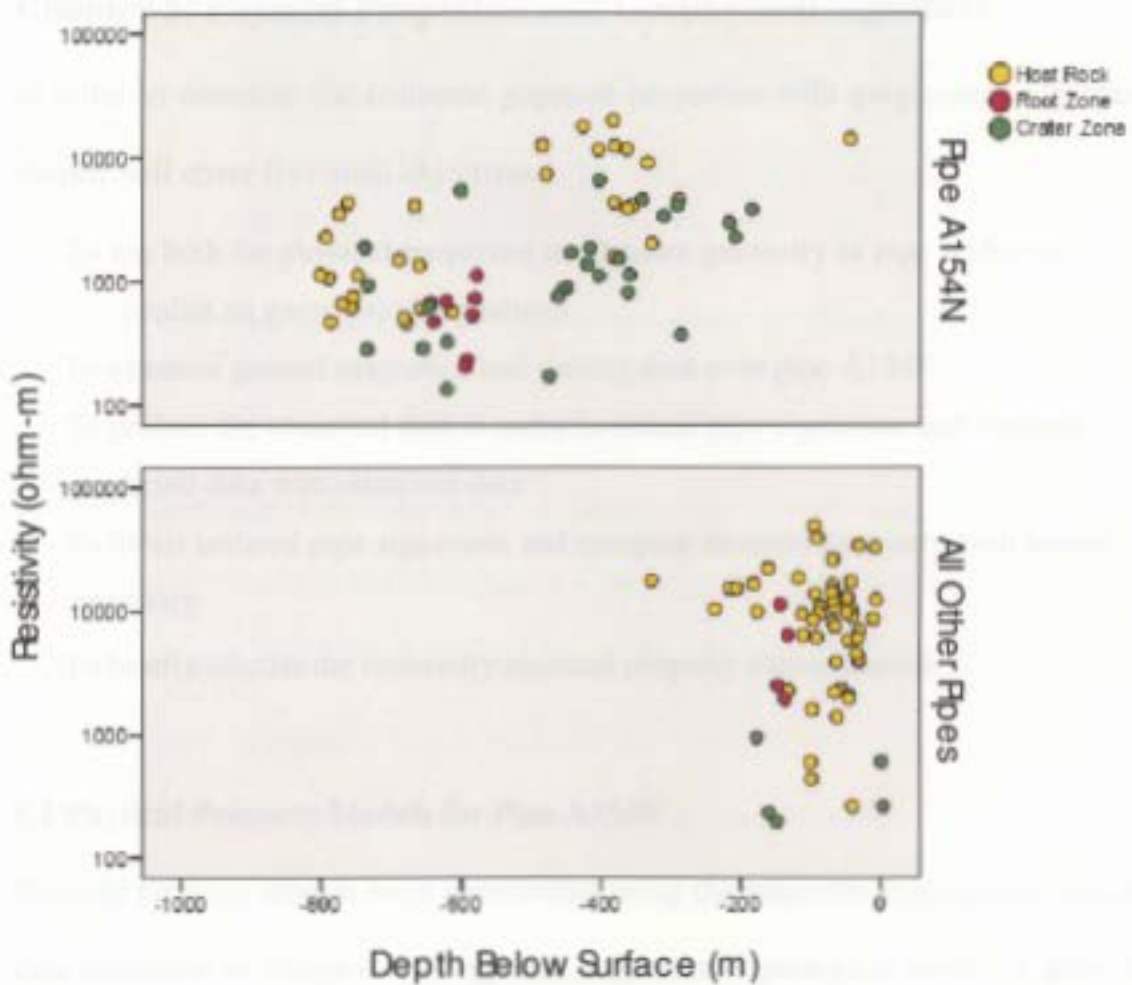
Depth with Magnetic Susceptibility	Host		Crater		Root	
	Pipe A154N	All Other Pipes	Pipe A154N	All Other Pipes	Pipe A154N	All Other Pipes
Correlation Coefficient	-.489**	-.099	-.486**	.133	.566	.490**
Number of Samples	94	96	67	69	13	41

Figure 4.15: Scatter plot and Spearman statistical results for depth vs. magnetic susceptibility for pipe A154N and the other pipes. It should be noted that in pipe A154N that some crater zone material has been found deeper then the root zone material. Note asterisks indicated associated conference level.



Depth with Magnetic Susceptibility	Host		Crater		Root	
	Pipe A154N	All Other Pipes	Pipe A154N	All Other Pipes	Pipe A154N	All Other Pipes
Correlation Coefficient	-.489**	-.099	-.486**	.133	.566	.490**
Number of Samples	94	96	67	69	13	41

Figure 4.15: Scatter plot and Spearman statistical results for depth vs. magnetic susceptibility for pipe A154N and the other pipes. It should be noted that in pipe A154N that some crater zone material has been found deeper than the root zone material. Note asterisks indicated associated confidence level.



Depth with Resistivity	Host		Crater		Root	
	Pipe A154N	All Other Pipes	Pipe A154N	All Other Pipes	Pipe A154N	All Other Pipes
Correlation Coefficient	.597	-.205	.542	-.2	.429	N/A
Number of Samples	33	52	27	5	8	4

Figure 4.16: Scatter plot and Spearman statistical results for depth vs. resistivity for pipe A154N and the other pipes. It should be noted that in pipe A154N that some crater zone material has been found deeper than the root zone material. Note asterisks indicated associated confidence level.

Pipe A154N	Magnetic Susceptibility (unitless)	Density (g/cm ³)
Host Rock	0.00008	2.66
Crater Zone	0.0014	2.522
Root Zone	0.0103	2.8

Table 12: Values used to represent the magnetic susceptibility and density models for pipe A154N.

As previously stated, pipe A154N was discovered under Lac de Gras. The thickness of the lake sediment over the pipe is unspecified; Diavik staff estimated it to be approximately 5m. Further assumptions are that the magnetic susceptibility of this sediment is negligible or at most the same as that of the host rock, and that the density of the sediment is equivalent to that found in the density table in Telford et al. (1990) for wet overburden: 1.97g/cm³. It could be argued that it is unlikely that the sediment layer would be of uniform thickness throughout the area, due to the slight bowl shape in the topography of an average kimberlite pipe. However, the sediment thickness in the area is unknown and it was felt that if a thicker layer of sediment was arbitrarily placed on top of the pipe it might significantly affect the size and shape of the resultant magnetic and gravity anomalies. To that end, all models used a 5m thick homogenous sediment layer throughout the survey area.

5.2 Forward Modeling

Physical property models of pipe A154N were used to generate gravity and magnetic forward models. These forward models represent the expected magnetic and gravitational signatures of the A154N pipe and were used to investigate the contributions of each

kimberlite zone to the geophysical anomaly over the pipe. The forward models were generated using GRAV3D version 3.1 (UBC-GIF 2002) and MAG3D version 2.0 (UBC-GIF 2002) software packages.

GRAV3D and MAG3D software packages use a mesh that discretized the subsurface and share similar forward modeling techniques. They are both based on formulae for gravitational and magnetic responses of a rectangular prism (Li and Oldenburg 1996). They operate using a principle of superposition, whereby every cell throughout the mesh is cycled through, adding their cumulative effects together to compute the forward model response at a signal observation point (Li and Oldenburg 1996). This is performed at every observation point on a grid.

MAG3D software package has noteworthy limitations. When using MAG3D there is an assumption made that the magnetic data is only caused by induced magnetization and there is no effect from remanent magnetization or demagnetization (Li and Oldenburg 1996). Since MAG3D is only designed to handle susceptibility and not remanent magnetization, it cannot handle large negative reduced to pole data making positivity an issue.

The subsurface mesh used for gravity and magnetic forward models is defined using a left handed coordinate system. During this thesis the mesh used was as 33 cells in the x direction, 29 cells in the y direction and 32 cells in the z direction. The cells in the x and

y directions are 25m wide, whereas the first layer of cells in the z direction are 5 m wide with the remaining 31 cells being 25m wide. The southwest corner of the mesh starts at the UTM coordinate 536328N, 7152421N (NAD 27). Both physical property models were made to fit inside this mesh.

As seen in Figures 5.3, the model of pipe A154N is confined to a box. This box is made up of a 3D mesh with each cell in the mesh equaling a finite relative density value, however the area outside the box is equal to zero. When the forward modeling process tries to evaluate the values at the edges of the box large gravitational anomalies are generated due to the sharp density discontinuity. To avoid this problem (as seen in Figure 5.3) the host rock value was set to zero and all kimberlite densities are given as densities relative to the average host rock value. These density contrast values are presented in Table 14 in Section 5.4.

5.3 Forward Modeling– Magnetic Field

The size of a kimberlite anomaly depends, in many cases, upon the relative strength and direction of remanent magnetization. This phenomenon is believed to be caused by the reversal of magnetic polarity in the region during the time of the kimberlite eruptions, that is if the total field magnetic response of the kimberlite pipe is dominated by remanent magnetization (Lockhart et al. 2004). As stated in the Section 5.2, MAG3D software does not account for remanent magnetization. However, remanent magnetization intensity data was collected for many of the physical property samples,

and a brief investigation into the importance of remanent magnetization in relation to magnetic modeling was conducted.

5.3.1 Investigation into Remanent Magnetization

The influence of reversed polarity remanent magnetization on a kimberlite pipe in the Northwest Territories was summarized by Keating and Sailhac (2004). If a kimberlite possesses remanent magnetization of sufficient strength, oriented in opposition to the present day field, the kimberlite anomaly will stand out as a negative anomaly against a background field (Keating and Sailhac 2004). However, if the remanent magnetization is oriented roughly parallel to the present field, the kimberlite anomaly will be positive relative to the background.

The Koenigsberger ratio for the samples of pipe A154N (Section 3.3, Eqn. 5) was calculated using a geomagnetic field of 47.77 A/m (60043nT) and the respective remanent magnetization intensity and magnetic susceptibility that was collected for each rock sample for pipe A154N. The Koenigsberger ratios for each rock type are shown as histograms for each rock type in Figure 5.4. By reviewing this figure it can be seen that each rock type shows ratios both below and above 1.0. The majority of the host rock samples are characterized by a value lower than 1.0. Remanent magnetization is therefore not considered to be important for most host rocks. Conversely, the two kimberlite zones (crater and root) show a higher percentage of samples with a ratio greater than 1.0. The kimberlite zones are therefore considered to possess a remanent magnetization that has a

significant effect on the magnetic anomaly. The small number of samples available for the root zone (N=14) may bias this result, however, the number of crater zone samples (N=52) is considered large enough to produce an accurate result. The Koenigsberger ratios of the crater zone samples seem to have a larger range than the root zone and should perhaps be considered more predominated by remanent magnetization than the root zone.

The results of this brief investigation into remanent magnetization has shown that the effects of remanent magnetization in Diavik kimberlites should not be ignored. Unfortunately, no other 3D inversion software package was available therefore MAG3D was used even with its limitations.

5.3.2 Magnetic Forward Modeling Discussion

The magnetic forward modeling processes require background information about the local geomagnetic field values. These values in the area of pipe A154N at the time of data collection were (Table 13):

Geomagnetic Field Values	
Inclination	84 decimal degrees
Declination	26 decimal degrees
Geomagnetic Total Field	60043 nT

(Geological Survey of Canada 2007)

Table 13: Geomagnetic field values for the location of A154N in 1994. These values were used during the magnetic forward modeling processes to account for location.

The forward modeling of pipe A154N generated a positive magnetic anomaly that is centered over the pipe location (Figure 5.5). The magnetic susceptibility model seen in Figure 5.2 was dissected into two separate models: a model of the crater zone (Figure 5.6) and a model of the root zone (Figure 5.8). The corresponding forward modeling results for each zone are seen in Figure 5.7 and 5.9 respectively.

The magnitude of the magnetic signature of a body is dependent on the depth at which the body is buried. The magnetic field strength of a dipole decreases at a rate of $1/r^3$, where r is equal to the separation distance between an observer and the dipole source (Telford et al. 1990). This dependence on depth can be seen in pipe A154N when comparing the signature of the crater zone (Figure 5.7) to the signature of the deeply buried root zone (Figure 5.9). It should be noted that the magnetic response of the root zone is not centered over the pipe location; this is believed to be caused by an effect of the depth of burial in combination with the magnetic inclination in the area. The crater zone, root zone and full model signatures are displayed as profiles (Figure 5.10). For pipe A154N, the shallow crater zone has a magnetic susceptibility that is much smaller than the more deeply buried root zone however, the magnetic dipole dependence with depth ($1/r^3$) drastically reduces the effect of the root zone.

The full model profile seen in Figure 5.10 displays a peak approximately 175m in width across the center of the pipe that reaches a maximum strength of 40nT. The crater zone profile displays a peak in the same area. This anomaly ramps slightly faster than the full

model profile, is about 175m wide, and reaches a maximum strength of 38nT. In contrast the root zone profile shows a 400m wide, elongate response, with a maximum value of 2nT. While the full model response is indeed a combination of the crater and root zone responses, the crater zone contributes the overwhelming majority of the full model response.

Recall in Section 5.3.1, the Koenigsberger ratio shows that the crater zone samples are predominated by remanent magnetization when compared to the root zone. Forward modeling has shown that the observed magnetic anomaly is mainly due to the crater zone which implies that remanence is considered as important as magnetic susceptibility in modeling the anomaly. Since the pipe A154N is considered to be from the Cenozoic Eon the remanence direction would be expected to be steep (Per. Comm., Hodych, 2007). The strength of the anomaly could be taken in to question since the forward modeling program does not take remanent magnetism in to consideration. This issue will also play a role in the inversion which will follow in a late section.

5.4 Forward Modeling - Gravity

As noted in section 5.2, the density models are constructed using density contrast values relative to the average density of the host rock (Table 14):

Rock Type	Measured (g/cm ³)	Contrast (g/cm ³)
Host Rock	2.66	0
Crater Zone	2.52	-0.138
Root Zone	2.8	0.14
Lake Sediment	1.92 ^{**}	-0.752

Table 14: Density contrast values used to represent the density properties of Pipe A154N. ^{**}The lake sediment values were not measured and are from Telford et al. (1990)

The forward model of the density data for pipe A154N generated a negative anomaly (Figure 5.11). Similar to the magnetic forward models (Section 5.1.1) the density contrast model (Figure 5.3) was split into two sections, the crater zone (Figure 5.12) and the root zone (Figure 5.14), with the corresponding forward modeling results shown in Figures 5.13 and 5.15.

5.4.1 Gravity Forward Modeling Discussion

The gravitational field strength of a point mass source decreases with burial depth according to an inverse square relationship when directly overtop the source (Telford et al. 1990). As seen in magnetic forward modeling (Section 5.1.1), this depth dependence is apparent when comparing the gravitational signature of the crater zone to that of root zone. The majority of the gravitational response from pipe A154N comes from the shallow crater zone and not the deeply buried root zone. The relative density contrast between root zone and host rock (0.14 g/cm³) is much less than that of the crater zone and host rock (-0.138 g/cm³), further reducing the root zone response.

The full model profile (Figure 5.16) displays a low across the pipe, which reaches a strength of -0.35 mGals. The crater zone profile in this figure displays a low that shadows the full model profile in width and strength. In contrast, the root zone profile shows a response that only differs from background the by $+0.01$ mGals. It is a wide response and does not seem to respond directly to the presence of the pipe. As in Section 5.1.1 for magnetics, if the gravity forward model maps are reviewed (Figures 5.11, 5.13, and 5.15) it can be concluded that the majority of the full model response is due to the contribution of the crater zone. This conclusion is reinforced by the profiles seen in Figure 5.16. It is due to the large density contrast between the host rock and the crater zone, and its relatively shallow burial depth. The root zone has only a slight density contrast to the host rock; combined with its greater burial it has very little impact on the gravity signature of the pipe.

5.5 Forward Modeling Conclusions

The magnetic and gravity forward modeling results for pipe A154N show the crater zone as contributing much more to the geophysical signature of the pipe than the root zone. If the physical properties in another pipe are similar to those seen in A154N, and the crater zone/root zone interface is as deep, then exploration should focus on finding the crater zone. However, the root zone may play a more important role in the discovery of other kimberlite pipes if the crater zone/root zone intersection is shallower.

From these forward modeling investigations, the size of the geophysical responses for various models can be estimated. Table 15 shows the size of each anomaly for the cases previously described for pipe A154N in Sections 5.3 and 5.4.

Model	Maximum Magnetic Anomaly Intensity (nT)	Maximum gravitational Anomaly Intensity (mGals)
Full Pipe	40	-0.35
Crater Zone	38	-0.35
Root Zone	2	~0

Table 15: The sizes of the anomalies seen in the forward models for magnetic field and gravity data.

It is proposed that the kimberlite signature of pipe A154N in survey data should be close in size to the forward modeling results. It should be emphasized that none of the forward models included noise and are simplified models of a complex area. Recall once again that remanent magnetization has not been properly accounted for during the forward modeling of magnetics data. This may bias the magnetic forward model response.

5.6 Observed Geophysical Ground Data

Diavik provided ground total magnetic field data and gravity data collected over pipe A154N in 1994 and 1995. Since A154N is located under Lac de Gras, the survey data was collected over the lake while it was frozen, providing a flat and relatively stable surface upon which to collect data.

5.6.1 Total Magnetic Field Data

Total magnetic field data over A154N was collected at a 50m-line spacing and 10m-station spacing by a contracted company (Figure 5.17). A visual inspection of the data leads to the conclusion that there is no clear anomaly present over the location of pipe A154N. The pipe signature could be hidden, either due to a strong regional field effect or a predominating remanent field. Unfortunately, the latter case cannot be fully explored since the direction for the remanent magnetization was not measured in the area due to a lack of oriented core samples. However since the location, magnetic susceptibility and geometry of pipe A154N are known, it provides an opportunity to explore methods that may be used to find pipes signatures that are masked by a strong regional field.

5.6.2 Gravity Data

The forward modeling results and the density data collected provide evidence to support the existence of a strong enough density contrast to differentiate between the host rock and the crater zone of the kimberlite in pipe A154N. Gravity data was collected on a 50m by 50m grid and all gravity corrections were completed at the time of collection by the contracted company (Figure 5.18). These corrections include drift, latitude, elevation and terrain. Since the diameter for a typical kimberlite pipe in the Diavik area varies from 75 to 150m, a grid spacing of a maximum of 25m by 25m would have been preferable. It is easier to constrain the maximal value of the pipe anomaly using a finer grid as opposed to a coarser grid. Spatial aliasing may also become a problem if any spectral filtering or analysis is performed on data collected using large grid spacing.

Gravity data is highly effected by topography (Telford et al. 1990), therefore bathymetry data were collected at the locations of each gravity data point in order to properly correct gravity data obtained over water (Figure 5.19). For quality control reasons, a colour map of the gravity data was overlain by contoured bathymetric data (Figure 5.20). To illustrate this point further, a profile was taken running west to east across line 7152950N (Figure 5.21). From Figures 5.20 and 5.21, it should be obvious that the bathymetry correlates too closely with the gravity data. Bathymetry corrections are absent from this dataset. In order to properly correct the gravity data, an infinite slab Bouguer correction was applied to the data using the following equation from Telford et al. (1990):

$$\Delta g = (0.04192mGal)\rho / d \quad (8)$$

where: ρ = density contrast (g/cm^3)
 d = bathymetric depth (m)

For the area over pipe A154N the density contrast between water ($1g/cm^3$) and host rock ($2.67g/cm^3$) is $1.67g/cm^3$. The correction was performed and added to the gravity dataset at each point. The results of this correction are displayed in map view in Figure 5.22, and in profile view in Figure 5.23. From Figure 5.22 it can be seen that the gravity data has been corrected over the bathymetric low centered at $\sim 536800E/7152950N$. However, by inspecting the profiles in Figure 5.23, it is argued that the Bouguer correction may have over-corrected the data. By reviewing the bathymetry measurements, it was found that there are only two points (50m apart) that define the extreme low in the lake. Coarse gridding of the data, in addition to the infinite slab assumptions associated with the Bouguer correction may be responsible for this over-correction.

To solve this problem it is suggested that by forward modeling an accurate subsurface model with appropriate bathymetry, a detailed bathymetry correction could be generated which would then remove the bathymetry effect more effectively (Personal Comm. Farquharson 2007).

A model of the bathymetry data was created (Figure 5.24) with the density of the host rock set at 0g/cm^3 and the density of the water set at -1.67g/cm^3 . The lake model was used to generate a forward model; the results the forward modeling were then added to the gravity dataset. The results of this correction can be seen as a map in Figure 5.25, and as profiles in Figure 5.26. As seen in the map view of the corrected data a gravity low (Figure 5.25) is now located roughly over the top of pipe A154N. The lake model corrected data profile seen in Figure 5.26 shows a gentler correction over the deepest part of the lake when compared with the Bouguer corrected data. This method appears to give a more accurate bathymetry correction than the Bouguer slab method, and therefore it is the preferred method used to correct the dataset.

5.7 Regional Residual Separation

Most magnetic and gravity surveys are used to find near surface features. The effects of deep masses and regional variations in rock types are called regional effects and can mask the effect of these near surface bodies. The problem comes in separating the anomalies of interest from the overlapping effects of the regional features (Telford et al. 1990). There are various techniques that can be used to remove regional effects,

classified as regional-residual removal techniques. Three removal techniques were used during this thesis to remove the regional effects. These include: upward continuation, low order polynomial removal and Li and Oldenburg regional/residual separation.

5.7.1 Upward Continuation

Upward continuation is a digital filtering method based on removing certain wavelengths from the data. The concept of upward continuation comes from the fact that the higher up the survey is taken, the less effect a small near surface body will have on a reading, leaving only the effects from deeper bodies. Long wavelengths are associated with regional fields and short wavelengths are associated with near surface bodies (Telford et al. 1990). Upward continuation is effectively a smoothing of the data where short wavelength anomalies are removed (Telford et al. 1990). After data has had an upward continuation applied, these results are then subtracted from the dataset producing a residual data set. Removal of long wavelengths from the data means the residual data is (in general) less smooth than raw data. For both gravity and magnetics data, the regional field was approximated using an upward continuation algorithm to a elevation of 25m, 50m, 100m and 150m . .

5.7.2 Second Order Polynomial

This method involves the estimation of the regional field by a least squares fitting of a second order polynomial to the collected data (Telford et al. 1990). Polynomials fitting to the 1st to 3rd order was used on both magnetic and gravity data to approximate the

regional field which was then removed to leave a residual considered to be due to the kimberlite.

5.7.3 Li and Oldenburg Separation Method

Unlike other methods, the Li and Oldenburg method does not assume that the regional field is smooth. When data is collected over a topographic surface then the regional field would not be smooth and this assumption would be inaccurate (Li and Oldenburg 1998^b). This method will be discussed in more detail in a Subsection 5.7.4.

Inversions are performed on residual data (Section 5.4), therefore the reliability of any subsequent interpretations and models depends highly on the accuracy of the regional/residual separation technique (Li and Oldenburg 1998^b). Note that no matter which technique is used, the separation will never be 100% effective because both regional and residual are distorted by each other's effect (Telford et al. 1990).

All methods produced reasonable regional fields, however, it was felt that after analyzing the results of all methods that the Li and Oldenburg (1998^b) produced the regional field that allowed for the best isolation of the pipe A154N anomaly. The Li and Oldenburg regional residual removal method and results will be displayed and discussed here for both magnetics and gravity.

5.7.4 Magnetism: Regional/Residual Removal Method

The Li and Oldenburg method applies both the method of stripping and their 3D inversion algorithm to a dataset. To begin with, the average geomagnetic field in the area at the time of collection must be determined. The geomagnetic field in this area at the time of data collection, as stated earlier in Section 5.1.1, was 60043nT. This value was removed from all data points as the MAG3D program requires a base line magnetic field value to be removed before the inversion will run (Figure 5.27). More detail about the inversion process will be discussed in Section 5.4. For now it is asked that it be accepted that the magnetic inversion process generates a model of the magnetic susceptibility characteristics of the subsurface beneath a given observed dataset. The Li and Oldenburg removal was performed using the following steps:

- 1) The observed magnetic dataset seen in (Figure 5.27) was used to perform a default inversion.
- 2) From this inversion a susceptibility model of the subsurface was generated.
- 3) The susceptibilities values in the area of pipe A154N, from the surface down to the bottom of the model, were set to zero (Figure 5.28). This process is referred to by Li and Oldenburg (1998^b) as stripping.
- 4) A forward model is then run over this stripped model. The resulting dataset produced by the forward model is considered to be the regional field of the area (Figure 5.29).
- 5) The regional field was then subtracted from the observed dataset, resulting in the residual dataset for pipe A154N (Figure 5.30)

5.7.5 Comparing Magnetic Residual Results with Forward Modeling

The forward model of the magnetic susceptibility of the full pipe model (Figure 5.5) appears to have a sharper anomaly than the residual data (Figure 5.30), however the widths of the anomalies are consistent with each other (at approximately 150m). As seen in Table 15 (Section 5.1.4), the maximum anomaly magnitude for the full model is 40nT, whereas the maximum magnitude of the anomaly in the residual data is 55nT (Figure 5.30). However, the shape of both anomalies are similar. The difference in anomaly magnitudes could be caused by the strong kimberlite remanent magnetization in the kimberlite, which was discussed in Section 5.1.2. It is felt that since remanent magnetization is not taken into account, and since no noise was added to the forward model, that the differences between the residual and forward model are acceptable.

The process of removing the regional field by way of the Li and Oldenburg method (1998^b) could have some questionable implications, particularly “stripping”, which are presented in three parts in Figure 5.31. Figure 5.31 (part a) represents a subsurface magnetic model with a constant magnetic susceptibility that is greater than zero. When the area of interest is stripped out and set to zero (part b) the total field over the stripped area drops. The resulting residual field is plotted (part c). The total magnetic field is zero everywhere except over the stripped region. This resulting anomaly is due to the stripping process. However, going back to the discussion of the magnetic results, since the data shown in the forward model is an acceptable match with the residual data given the lack of data on remanent magnetization direction, the Li and Oldenburg removal was still used

to generate residual data. This residual data will be used during inversions presented in Section 5.7.

5.7.6 Gravity: Regional/Residual Removal

Similar steps to the regional/residual separation for magnetics data were carried out on the gravity data for pipe A154N. First, a constant value of 57mGal was removed from all data points (Figure 5.32). This value was chosen, as it is the minimum value over the corrected dataset. The stripped area is shown in Figure 5.33. From this, a forward model was generated creating a dataset considered to be the regional field of the area (Figure 5.34). This regional data set was then subtracted from the corrected gravity dataset. The result is the residual gravity data for the A154N gravity dataset (Figure 5.35).

5.7.7 Comparing Residual Results with Gravity Forward Model

The forward model of the full pipe density contrast model (Figure 5.11) shows a sharper, rounded anomaly over the pipe than the residual data (Figure 5.35). The forward model predicts a pipe anomaly of -0.58mGals , with the residual data showing a pipe anomaly of -0.35 mGals . This difference may be caused by the lack of noise in the forward model, plus average values are being used to represent the kimberlite zones and host rock. These averages values are representative of a wide range of values, which were measured for each rock type. Even though there was no monotonically correlation found between the density values and depth during the Spearman test (Section 4.5.4) it is reasonable to think that the density values will change somewhat throughout the pipe. The same questions

The objective function is broken down into two parts as defined by Farquharson (2006) in Eqn. 9 :

$$\Phi = \phi_d + \mu\phi_m \quad (9)$$

where: ϕ_d = measure of data misfit

ϕ_m = measure of the amount of structure in the model

μ = regularization or trade-off parameter that controls the contributions of the data misfit and model complexity terms.

5.8.1 Data Misfit

The first part of the objective function is the data misfit, which is the measure of error between the predicted data and the observed data (Eqn. 10):

$$\phi_d = \left\| W_d (d - d^{obs}) \right\|_2^2 \quad (10)$$

where: d^{obs} = data vector

d = predicted data vector

$W_d = \text{diag}\{1/\sigma_1, \dots, 1/\sigma_N\}$ and σ_i is error standard deviation of the error associated with the i^{th} datum

ϕ_d = data misfit

$\| \cdot \|^2 = L_2$ Norm of a vector

5.8.2 Measure of Structure in the Model

The second part of the objective function is the model objective function (Eqn. 11), a key component in the inversion process as it works to reduce the structural complexity of the model (Li and Oldenburg 1998). The model objective function is problem dependent, is

relatively smooth in three dimensions, and is flexible enough to construct different models.

$$\phi_m(m) = \alpha_s \int_V w_z \{w(z)[m(r) - m_0]\}^2 dv + \alpha_x \int_V w_x \left\{ \frac{\partial w(z)[m(r) - m_0]}{\partial x} \right\}^2 dv + \alpha_y \int_V w_y \left\{ \frac{\partial w(z)[m(r) - m_0]}{\partial y} \right\}^2 dv + \alpha_z \int_V w_z \left\{ \frac{\partial w(z)[m(r) - m_0]}{\partial z} \right\}^2 dv \quad (11)$$

where: w_s , w_x , w_y , and w_z = spatially dependent weighting functions

α_s , α_x , α_y , and α_z = coefficients that affect the relative importance of different components in the objective function

m_0 = reference model

$w(z)$ = depth weighting

A reference model can also play an important role in the objective function (term m_0). A reference model is a mesh of physical property values provided by the interpreter based upon known geological features and appropriate estimates of physical property values. Note that an initial model is used as a starting point for the inversion, and the reference model is compared to the inversion at each iteration. When a reference model is introduced, the nonuniqueness of the model is decreased because it works to constrain the inversion (Li and Oldenburg 1998).

As previously stated, potential field data have no inherent depth resolution; for example a dense (susceptible), deeply buried object or a less dense (less susceptible), near surface lens of material can in the right circumstances produce similar anomalies. Inversions tend to favor the latter; therefore structures tend to concentrate near the surface without regard to the true depth of the body (Li and Oldenburg 1998). To overcome this problem, a

posed concerning the Li and Oldenburg regional/residual separation discussed in the magnetic forward modeling section can be raised here. Once again, since the forward model and residual results are of comparable shapes and magnitudes, the regional removal is considered to have been correctly performed.

5.8 Inversions

Inversions are an important geophysical tool used to generate models of the subsurface under a selected dataset. Inversions were performed using the UBC-GIF inversion software on the residual data presented in Section 5.6. An initial model composed of a set of rectangular cells comprising an orthogonal 3D mesh is used to represent the subsurface. Each cell has a uniform magnetic susceptibility or density and the anomaly is located on the surface formed by the mesh. The same mesh that was used during forward modeling (Section 5.2) was used during the inversions.

The primary problem facing the inversion of potential fields data is its inherent nonuniqueness. In other words, there are an infinite number of subsurface solutions that could generate the known anomaly. MAG3D and GRAV3D use an objective function to minimize this problem. The objective function is defined as a combination of how well observations are reproduced, and a measure of how complicated the model is (Farquharson 2006).

depth weighting function ($w(z)$) is introduced to the objective function (Li and Oldenburg 1998) given as (Eqn 12):

$$w(z) = \frac{1}{(z + z_0)^{\beta/2}} \quad (12)$$

where $(z + z_0)^{\beta/2}$ is used to approximate the decay of the inversion kernel with depth directly under the observation point. The β term depends upon the inversion. Gravitational effects of a point mass decay with distance according to an inverse distance square relationship, in which cases the default value for β is 2. In contrast, the magnitude of a magnetic dipole decays according to an inverse cubic relationship; therefore the default value for β is 3. The default value of z_0 is 0 for both gravity and magnetic inversions. By adjusting the values of z_0 and β , a good match between this depth weighting function and the decay of the kernel for a given mesh and observation height can be achieved. Appropriate values used for z_0 and β will be discussed in further detail below.

5.8.3 Depth Weighting

To decide on model appropriate values for z_0 and β , an experiment was performed by varying both parameters independently and testing their effects upon the results of the inversion. This test was performed for both magnetics and gravity data and Figure 5.36 demonstrates the results. Values were assessed by running a magnetic and gravity inversion of the data using all program defaults. This produced a fuzzy blob near the top

of the subsurface model. Varying the depth parameters elongated the fuzzy blob so that it looked closer to the shape of a kimberlite pipe and was centered at a more appropriate depth. For magnetics it was decided that a z_0 value of 150 and β value of 3 should be used, whereas for gravity a z_0 value of 50 and β value of 3 should be used instead of the default values.

In conclusion, only when all steps of the inversion have been carefully considered will a physically realistic result be generated. More information about the inversion process can be found in Li and Oldenburg (1996/1998) and the manuals for UBC MAG3D and GRAV3D inversion software.

5.9 Gravity and Magnetic Inversion

Two inversions were performed for each dataset, including a *default mode* inversion using no user-defined parameters and all program defaults, and a *model mode* inversion where an initial and reference model, and appropriate depth weighting are used with all other parameters equal to default values. Both methods produced a dataset that was then compared to the residual dataset. The discussion of the results will be broken down into a section describing gravity and a section describing magnetics, with a general conclusion to follow describing the combined results. Note that the colour scales of all predicted models were changed to the same scale as that of the measured physical property models, in order to aid in comparison between models.

5.9.1 Gravity Inversion

Gravity inversion was first performed using the default mode and in this mode no problems were experienced. The predicted dataset (Figure 5.37) generated by the inversion is similar to the residual data (Figure 5.35). The density contrast subsurface model produced by this inversion can be seen in Figure 5.38. The figure is a depth slice of the inverted 3D density model along line 7152900N, which cuts across the location of pipe A154N. The model does show a lower-density body in the same area as the pipe. The width of this body is approximately 100m across and extends to a depth of approximately 200m.

In the *model mode* inversion, an initial model and reference model were input at the beginning of the inversion process. Both the initial and reference models are the same as those used in the gravity forward models of the previous section (Figure 5.3). The density contrast model produced by this inversion can be seen in Figure 5.40. This model bears a resemblance to the model seen in Figure 5.3. The density contrast of this model displays a low density layer extending down ~5m, and a low density pipe structure (crater zone) sitting in a background of relatively high density material (host rock). This pipe-like structure extends to a depth of approximately 400m, with a diameter of approximately 150m. The root zone appears at a depth of 400m with a homogenous density contrast value of 0.14 g/cm^3 . The heterogeneous density structure of the crater zone is obviously quite different from the reference model. However, if the pipe anomaly in the residual data (Figure 5.35) is reviewed, the anomaly is lopsided, with the eastern edge being much

more negative than the western edge. It is believed that this sharp change in the residual anomaly is forcing the east west dichotomy in the inverted subsurface density model (Figure 5.40). This change lopsided anomaly is indicating that there are variations in the density values of the crater zone. The variation in crater density with depth was not predicted in Subsection 4.5.3 to be depended as a monotonic function however, since mean density values were used to represent each rock types it is reasonable to expect that there are variations in the density of the crater zone. Especially since it is composed of backfill material, which causes inhomogeneity in the crater zone. From the *model mode* inversion a better understanding of the variation in crater density can be predicted. There is denser material located on the eastern half of the pipe, this variation in density continues to a depth of approximately 250m. Under this denser material less density material is found. It seems, however, that the depth weighting parameters and the initial and reference models were successful in constraining the pipe model more accurately when compared with the results of the *default mode* inversion (Figure 5.38).

5.9.2 Magnetic Inversion

The data used for the magnetic inversions were trimmed to remove areas of extreme values that were causing errors during the inversion process (Figure 5.41). These areas were not related to the pipe, but to other geological features in the area. However, certain data points in Figure 5.41 that are adjacent to the pipe anomaly have extremely low values (-20 to -35nT) compared with average pipe anomaly values of approximately 35nT. These points were not considered to be related to the pipe signature but rather with

some extremely near surface feature and it caused positivity problems for the inversion. It was decided to set the value of the points to zero (Figure 5.42). The trimmed and zeroed map was used for the subsequent magnetic inversions.

Inversion in this mode was performed without problems. The predicted dataset (Figure 5.43) appeared similar to the residual data (Figure 5.42). The magnetic susceptibility model produced by this inversion can be seen in Figure 5.43 as a depth slice that was taken along line 7152900N, which crosses the location of pipe A154N. The model shows a body of high susceptibility in the same area as the pipe. The diameter of this body is approximately 100 m, with high magnetic susceptibility that extends to a depth of approximately 200m. The area of extremely high magnetic susceptibility on the western edge of the model is either an artifact of the inversion, or some large-scale geological feature.

Running an inversion in the *model mode* consisted of inputting an initial model and reference model at the beginning of the inversion process to help constrain the inversion. Depth weighting was also applied as discussed in Section 5.4 ($z_0 = 150$ and $\beta = 3$). Both the initial and reference models were the same model as that used for the forward models of the previous section (Figure 5.2). The predicted dataset (Figure 5.45) appeared similar to the residual data (Figure 5.41). The magnetic susceptibility model created during the *model mode* (Figure 5.46) bears a close resemblance to the susceptibility model of the pipe seen in Figure 5.2 except that the top zone is discontinuous. This

inverted model displays a pipe structure that possesses high magnetic susceptibility to a depth of approximately 400m; at approximately 400m a material of higher magnetic susceptibility is seen that extends to a depth of approximately 750m. The inversion has broken the pipe into two zones: the top, or crater zone, and the bottom, or root zone. The crater zone here is discontinuous, which is believed to be caused by the slight lopsided magnetic anomaly (Figure 5.30) similar to that seen in the gravity model mode inversion. Once again this sharp change in the residual anomaly is forcing the east west change in the inverted subsurface model, the effects of which can be seen at depth. In Subsection 4.5.3 there was a medium decreasing monotonic function dependence found between magnetic susceptibility with all rock types. This relationship with depth supports the changes in magnetic susceptibility with depth. Once again the crater zone is predicted to be more susceptible to these changes due to the nature of its composition. It appears, however that the initial and reference models and the depth weighting parameters have accurately constrained the size and magnitudes of the kimberlite pipe.

5.9.3 Inversion Discussion and Conclusions

As with all inversions, there are an infinite number of subsurface models that can give rise to a dataset. It is felt that the two different inversions modes (*default* and *model*) performed on the gravity and magnetic data reinforce this point. For the gravity inversion processes, the predicted data for the *default mode* inversion (Figure 5.37) and the *model mode* inversion (Figure 5.39) are very similar, however their respective subsurface models are markedly different (Figure 5.38 and 5.40). This is also seen during the

magnetics data inversion processes (compare Figure 5.41 and 5.45 with Figure 5.44 and 5.46). The *model mode* models were generated using parameters that were specifically chosen to isolate pipe A154N after experimenting with the z_0 and β terms of the weighting function. The initial and reference models of pipe A154N played an essential role in constraining the inversion results.

It is felt that even though the inverted *default mode* models for both gravity and magnetics data do not show the same level of detail as the *model mode* models, they do show similar physical property patterns. This similarity consists for gravity data as a lower density material in the same location as the pipe, and for magnetics as a higher susceptibility material in the same location as the pipe. This means that results from *default models* cannot be completely dismissed. However, the *model mode* result is the preferred inversion since it takes into account the true physical properties and geometry of pipe A154N. The *model mode* also maps the variations in density and magnetic susceptibility in the crater zone. In this thesis there has been no mention of diamond content being related to the density or magnetic susceptibility however if there was a correlation found relating density or magnetic susceptibility to the percentage of diamond content this model mode inversion would prove to be useful.

5.10 Resistivity

The main focus of the investigation into the correlation between physical properties and geophysical signatures was spent on magnetization and gravitational fields. This detailed

investigation did not allow for a full investigation into resistivity signatures. Plus there was no access to a 3D EM forward modeling program. Despite this, it is felt that since resistivity data was collected, some comments should be made about the resistivity properties of each rock type. Resistivity data for pipe A154N does show a slight difference between host rock (average of 4969 ohm-m), crater zone (average of 1858 ohm-m) and root zone (unknown).

There has been debate amongst the geology staff at Diavik as to whether the resistivity signature of a kimberlite pipe is caused by the physical properties of the pipe itself, or by the lake sediment that is present on top of a pipe when found under a lake. The resistivity values measured do suggest that a kimberlite pipe could give rise to an EM anomaly. Unfortunately, no lake sediment samples were available for measurement. It has, however, been suggested that the resistivity of the sediments may be much lower than the surrounding host rocks due to assumptions about the lake sediment's composition (i.e. clay rich, water saturated) This issue that cannot be confirmed without direct measurements of the resistivity of lake sediments.



Figure 5.1: Geometric geology model of pipe A154N (south face). The geology layers used in this detailed model are not the same as those used in this thesis. The two kimberlite zones (cater and root) are marked on this model.

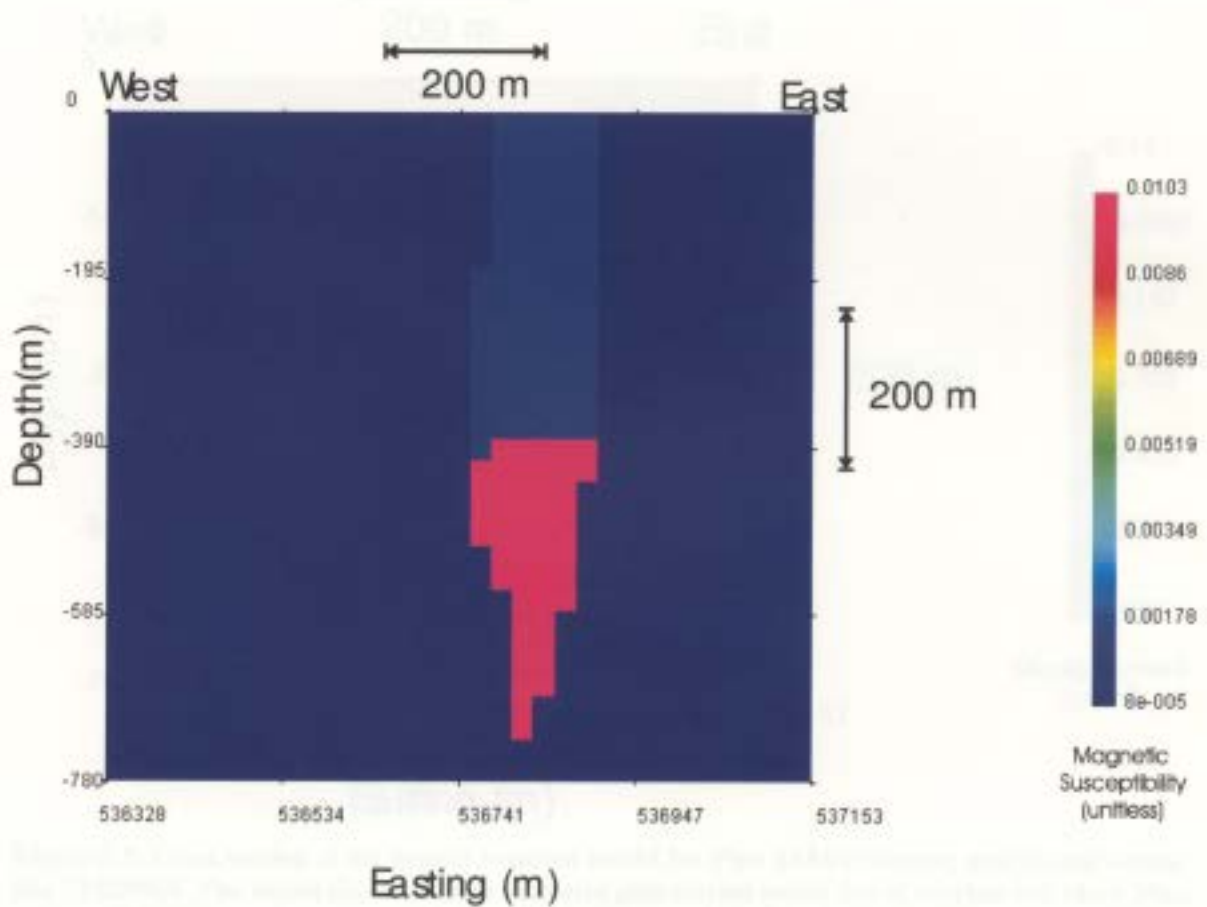


Figure 5.2: Cross section of the magnetic susceptibility model for Pipe A154N running west to east across line 7152896N. The model shows a 100m diameter pipe buried under 5m of overburden. The pipe is completely surrounded by the host rock group in dark blue. The crater zone (in light blue) intersects the root zone (in pink) at approximately 400m below surface.

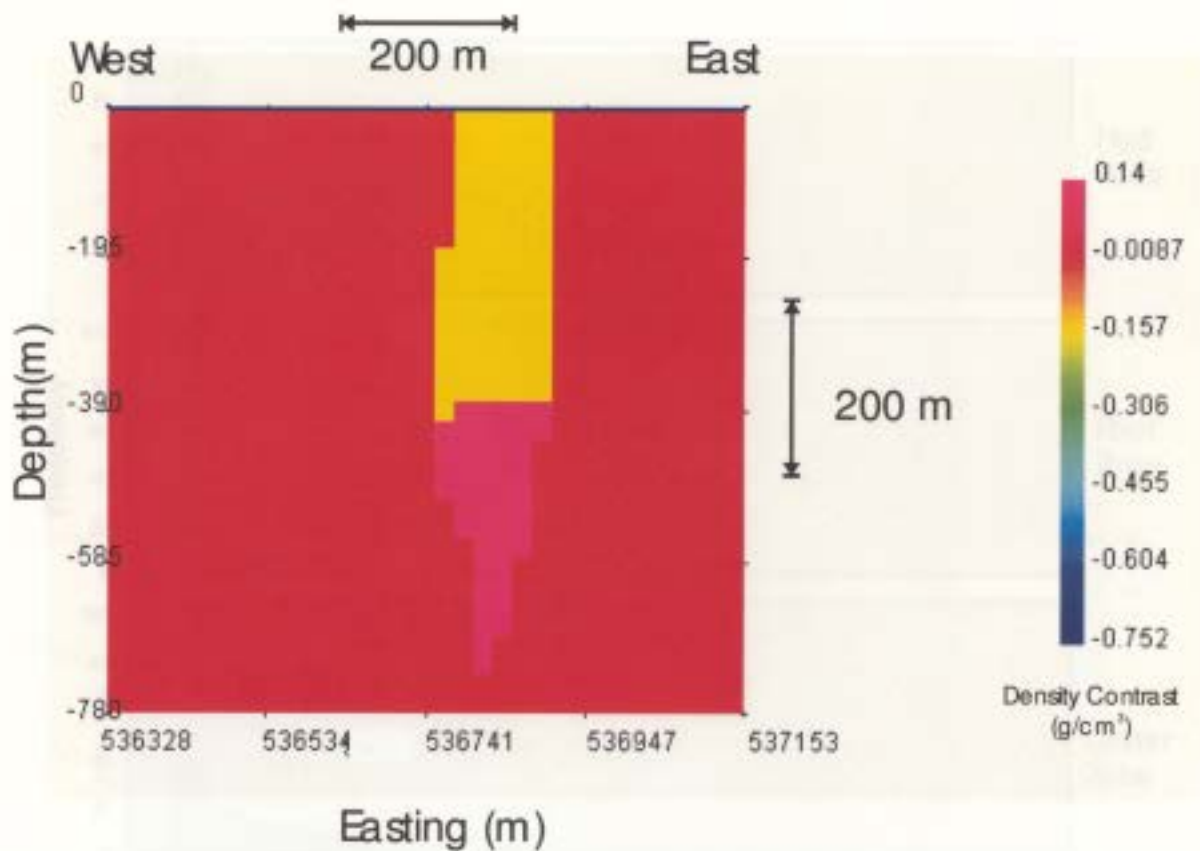


Figure 5.3: Cross section of the density contrast model for Pipe A154N running west to east across line 7152896N. The model shows a 100m diameter pipe buried under 5m of overburden (dark blue). The pipe is completely surrounded by the host rock group in red. The crater zone (yellow) intersects the root zone (light pink) at approximately 400m below surface.

Figure 5.3: Cross section of the density contrast model for Pipe A154N running west to east across line 7152896N. The model shows a 100m diameter pipe buried under 5m of overburden (dark blue). The pipe is completely surrounded by the host rock group in red. The crater zone (yellow) intersects the root zone (light pink) at approximately 400m below surface.

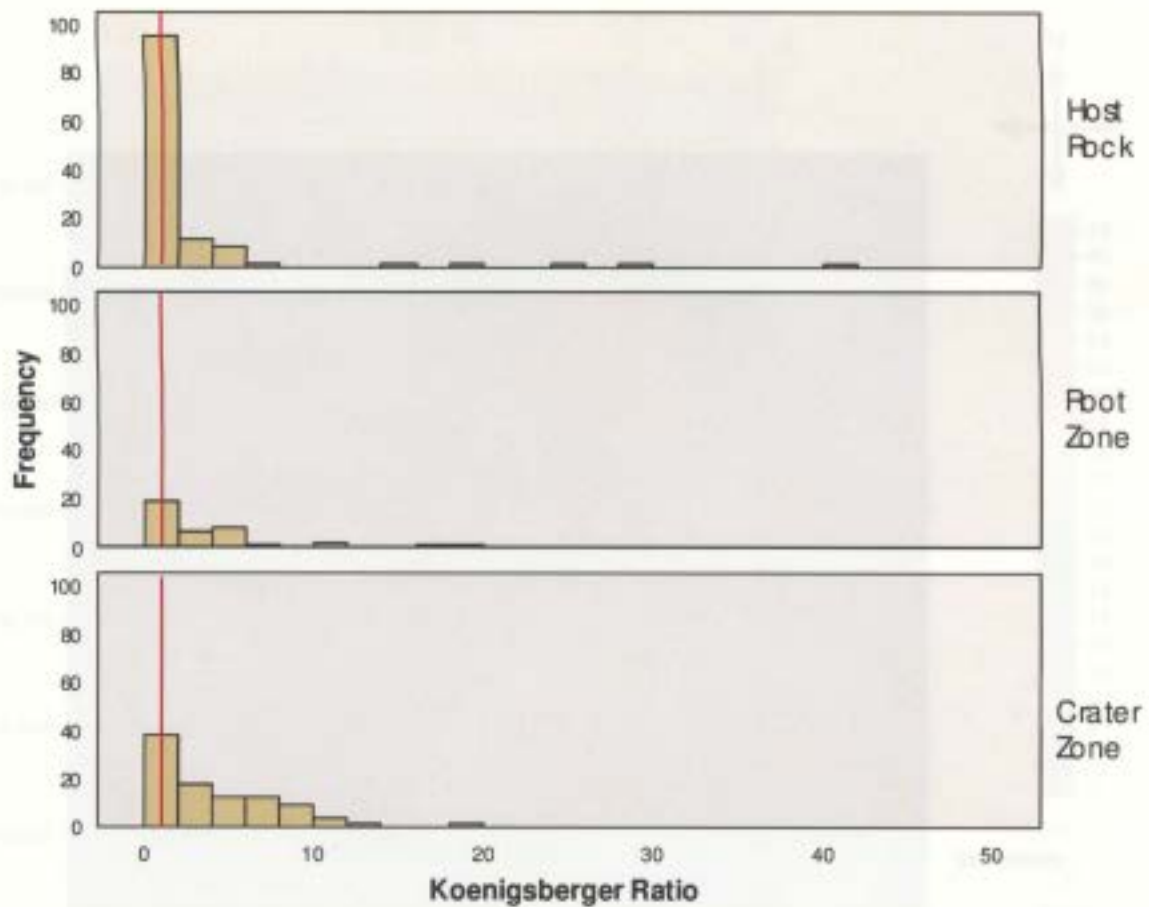


Figure 5.4: Histograms of the Koenigsberger ratio for each rock type. The red line on each graph marks the location the ratio when it is equal to 1. The host rock shows the majority of the samples have a ratio under 1, whereas both kimberlite zones have a larger variation of ratios.

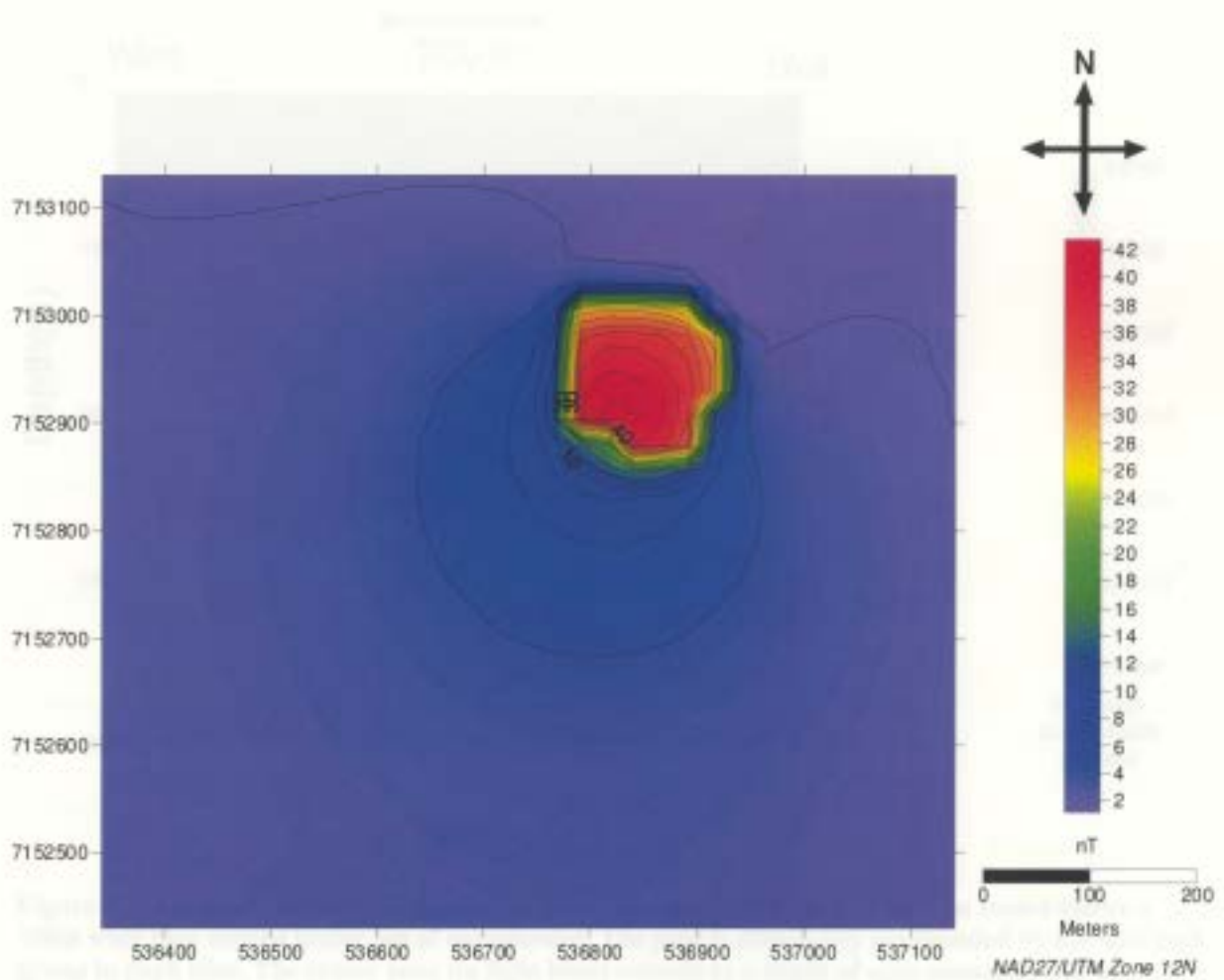


Figure 5.5: Forward modeling result of the magnetic susceptibility model of Pipe A154N as seen in Figure 5.2. This represents the signature of pipe A154N with no magnetic noise and no remanent magnetization. The pipe anomaly has a diameter of 150m with a maximum strength of 40nT.

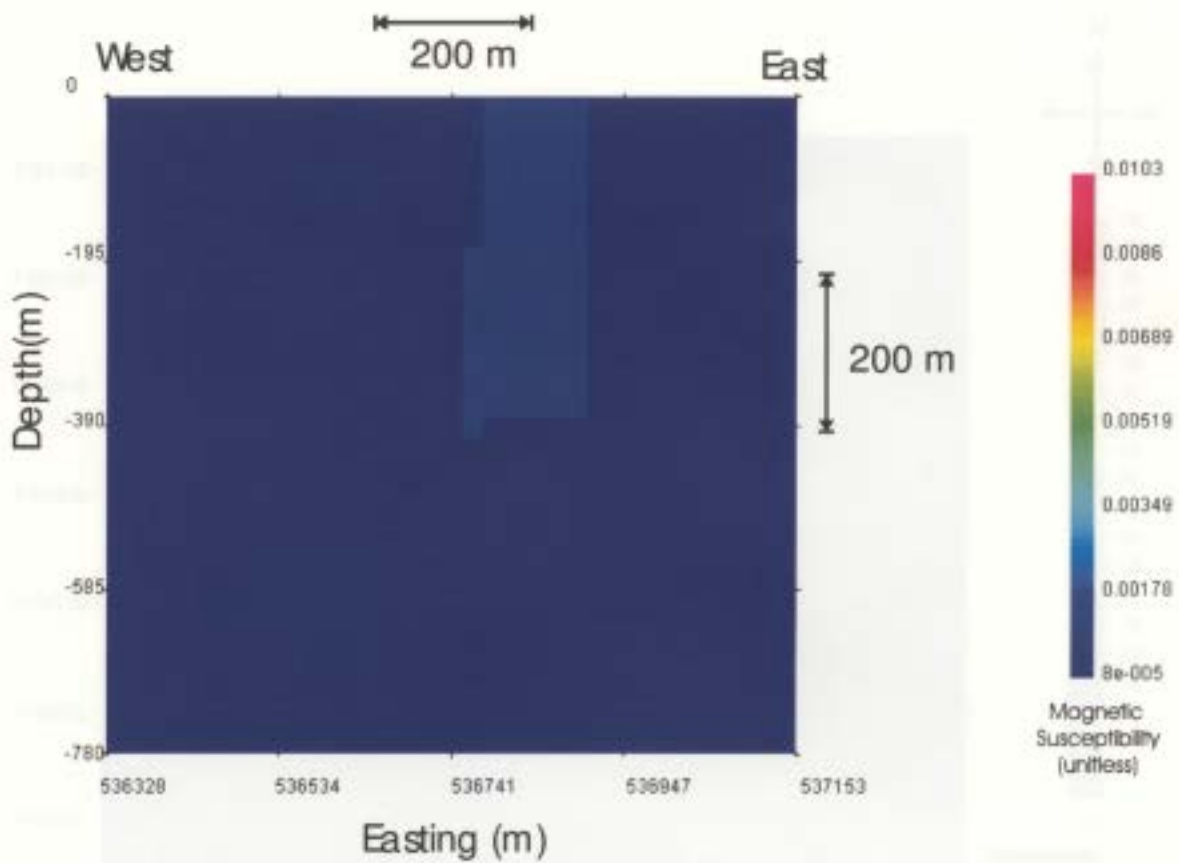


Figure 5.6: Magnetic susceptibility model of the crater zone for Pipe A154N. The model shows a 100m wide pipe buried under 5m of overburden. The pipe is completely surrounded by the host rock group in dark blue. The crater zone (in light blue) extends to a depth of approximately 400 m

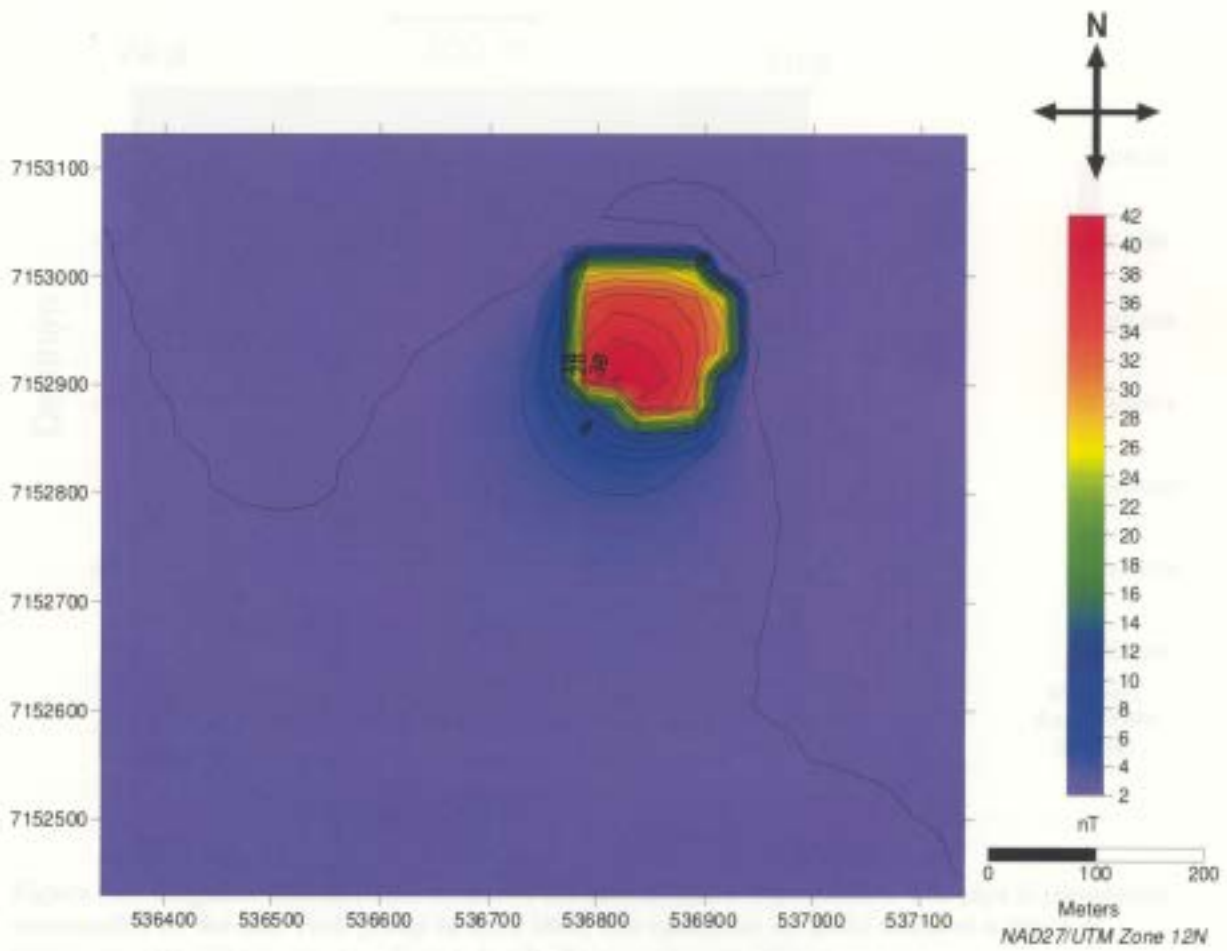


Figure 5.7: The forward modeling result of the magnetic susceptibility model (Figure 5.6) of the crater zone for Pipe A154N. This represents the ideal pipe signature with no magnetic noise. The pipe is shown as a 150m wide, positive anomaly with a maximum strength of 38 nT.

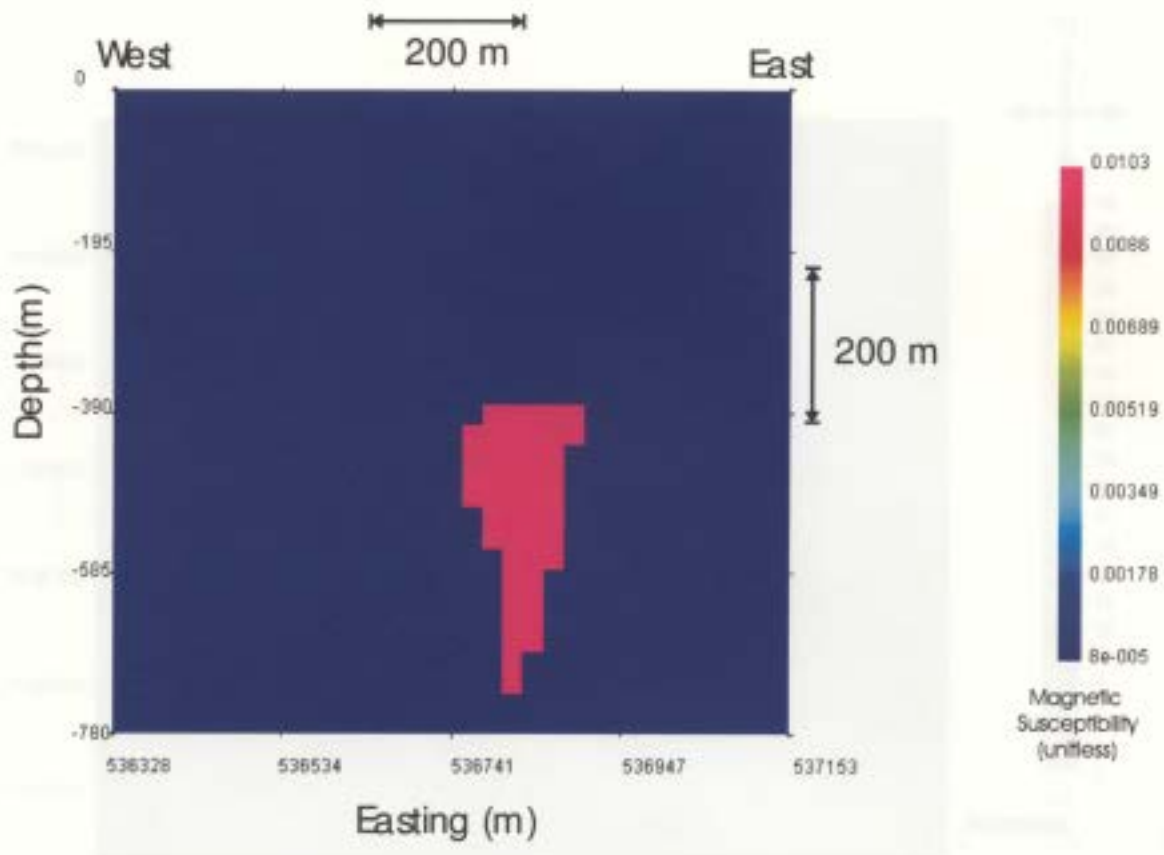


Figure 5.8: Magnetic susceptibility model of the root zone for Pipe A154N. The pipe is completely surrounded by the host rock group in dark blue. The root zone (in pink) starts at a depth of approximately 400 m and extends to a depth of approximately 750m.

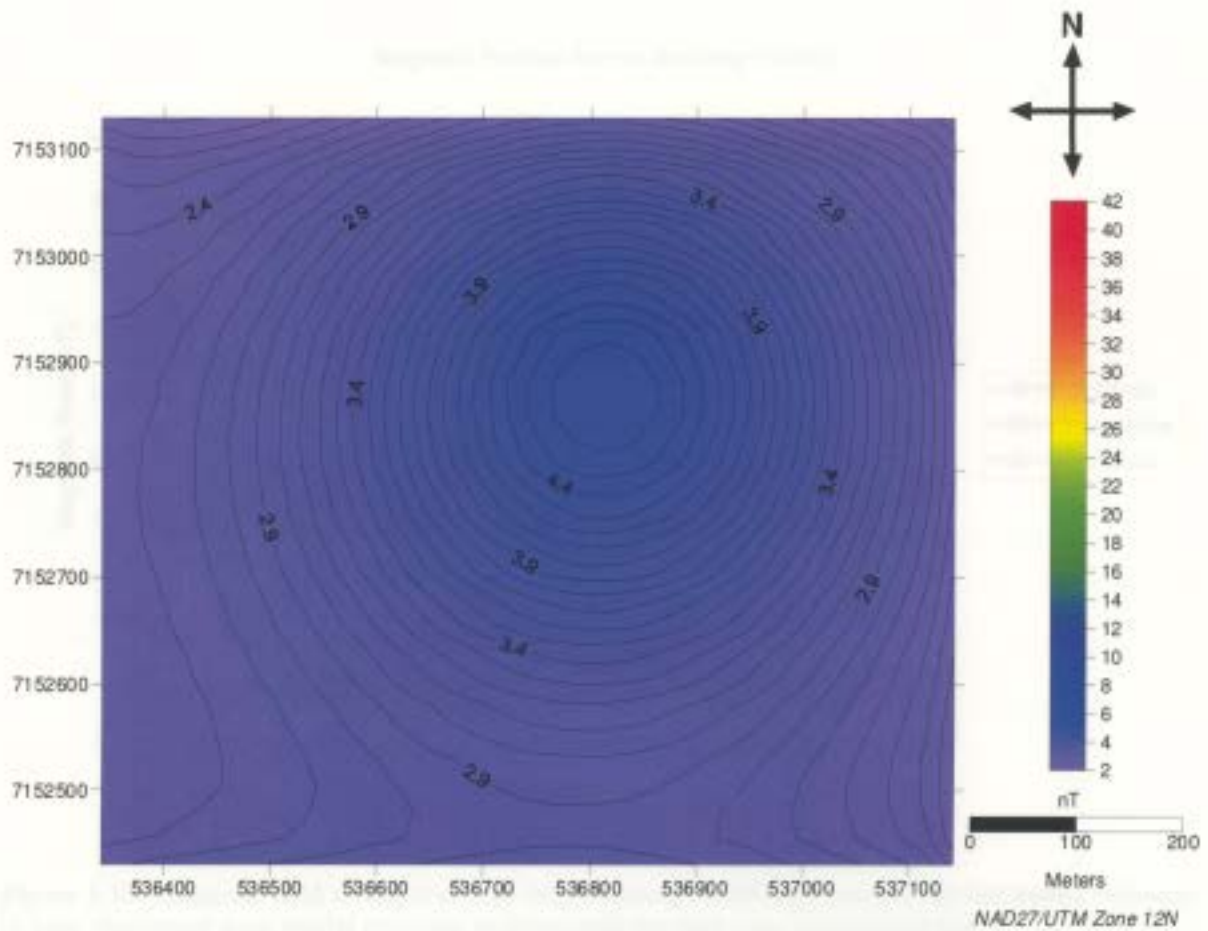


Figure 5.9: Forward modeling result of the magnetic susceptibility model of the root zone for Pipe A154N as seen in Figure 5.8. This represents the ideal pipe signature with no magnetic noise. The pipe is shown large, wide, low strength anomaly with a maximum strength of 2nT.

Magnetic Profiles Across Northing 7152910

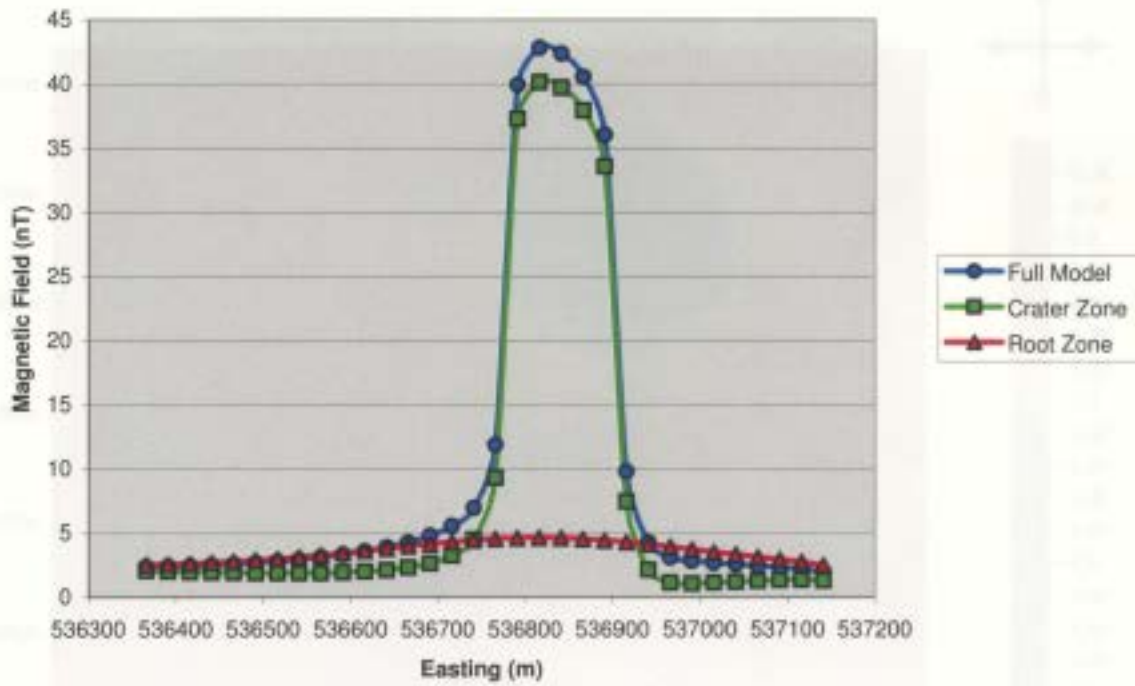


Figure 5.10: Magnetic field strength of pipe A154N along 7152910N showing the full model response in blue, the crater zone model response in green and the root zone response in red

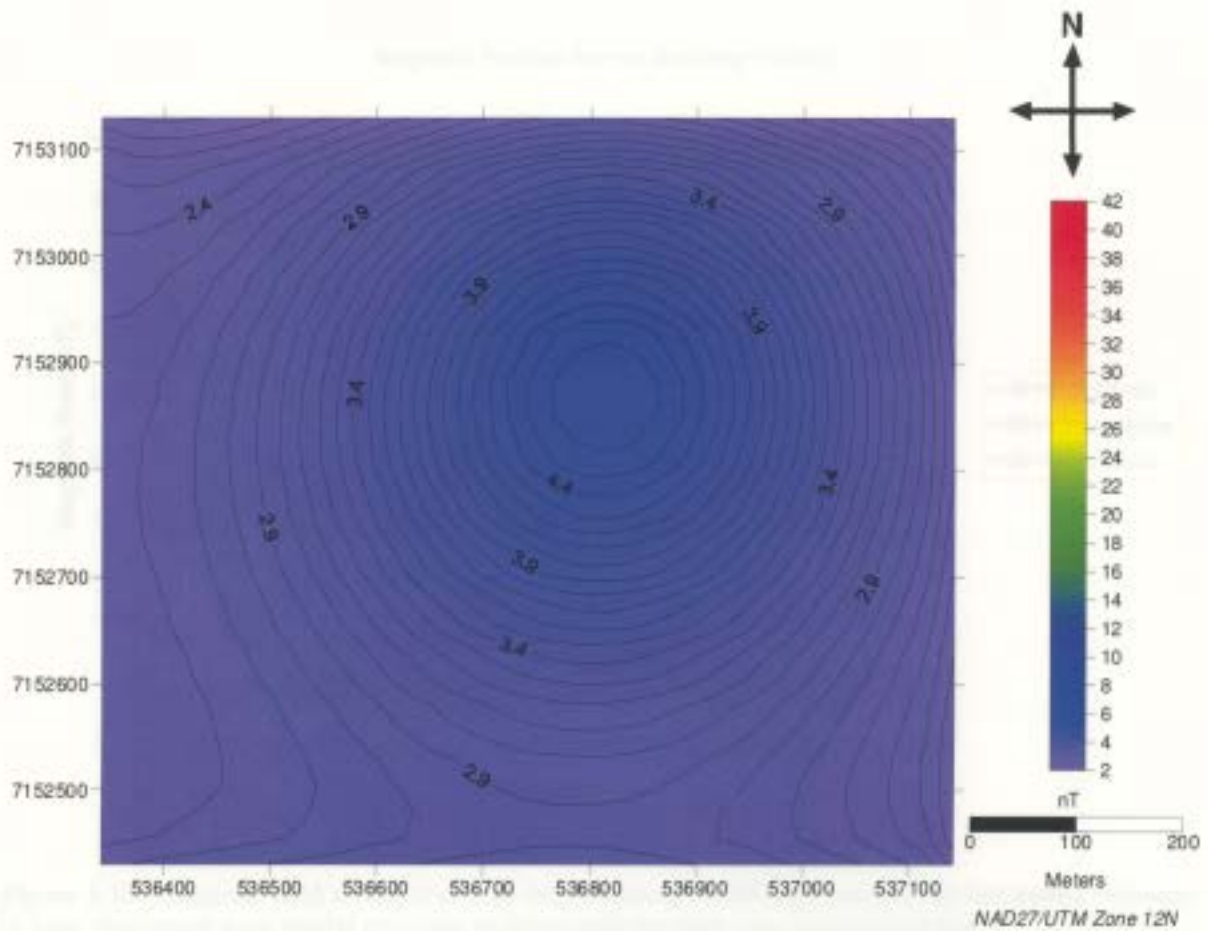


Figure 5.9: Forward modeling result of the magnetic susceptibility model of the root zone for Pipe A154N as seen in Figure 5.8. This represents the ideal pipe signature with no magnetic noise. The pipe is shown large, wide, low strength anomaly with a maximum strength of 2nT.

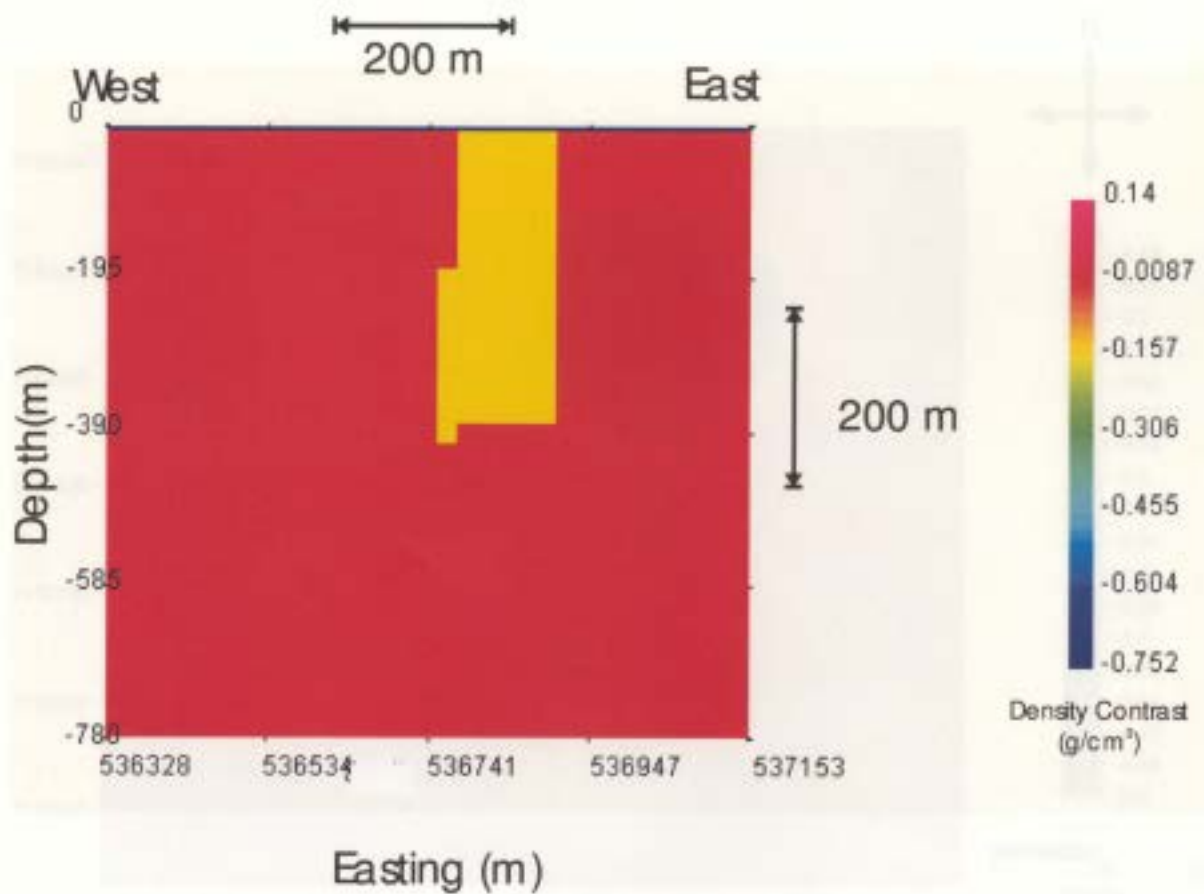


Figure 5.12: Density contrast model of the crater zone for Pipe A154N. The pipe is completely surrounded by the host rock group in pink. There is a 5m thick layer of lake sediment on top of the crater zone (dark blue), which extends to a depth of approximately 400m.

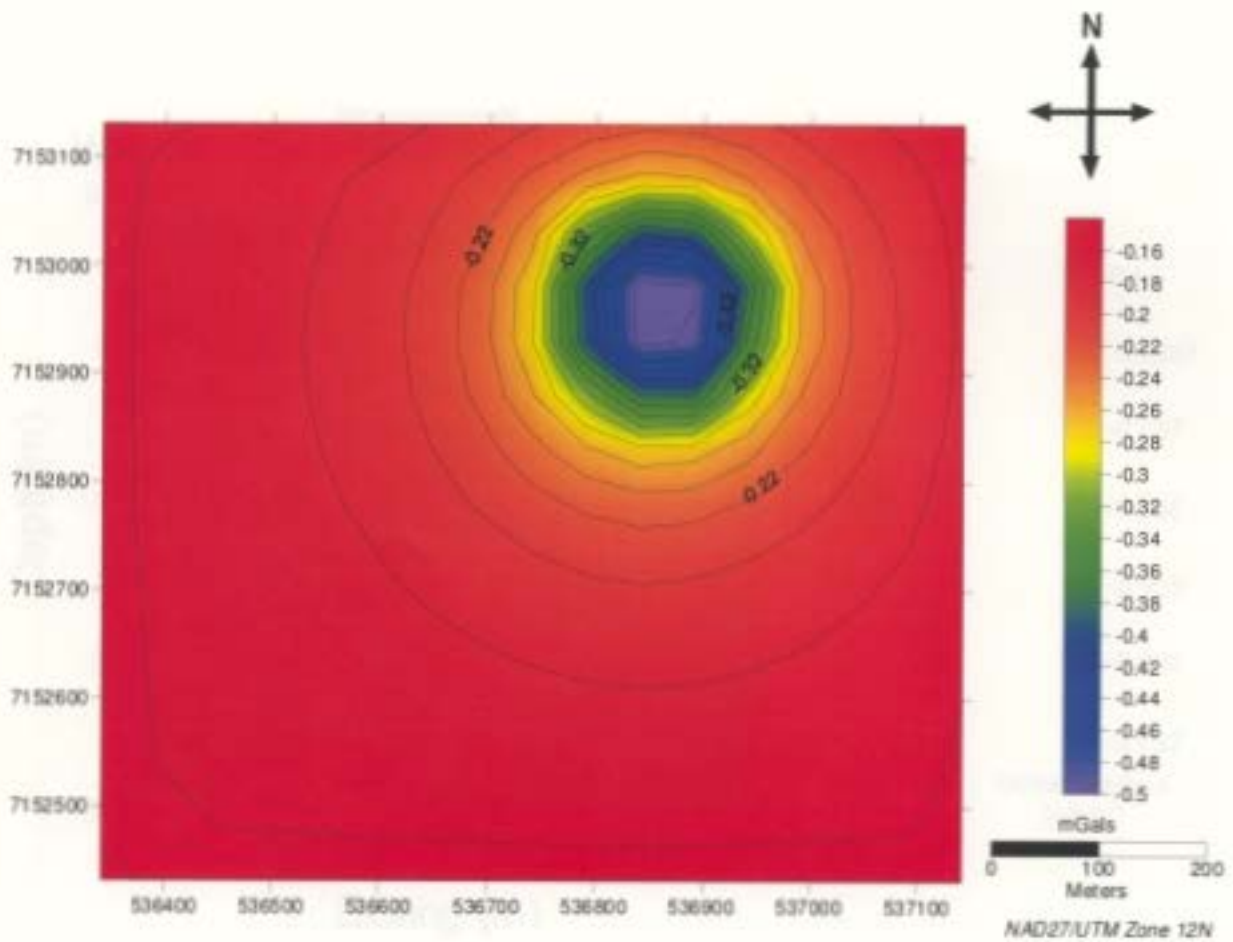


Figure 5.13: Forward modeling result of the density contrast model of the crater zone for Pipe A154N. This represents the ideal pipe signature with no noise. The pipe is shown as a 150m wide, negative anomaly with a maximum strength of -0.54 mGals.

Figure 5.13: Forward modeling result of the density contrast model of the crater zone for Pipe A154N, as seen in Figure 5.12. This represents the ideal pipe signature with no noise. The pipe is shown as a 150m wide, negative anomaly with a maximum strength of -0.54 mGals.

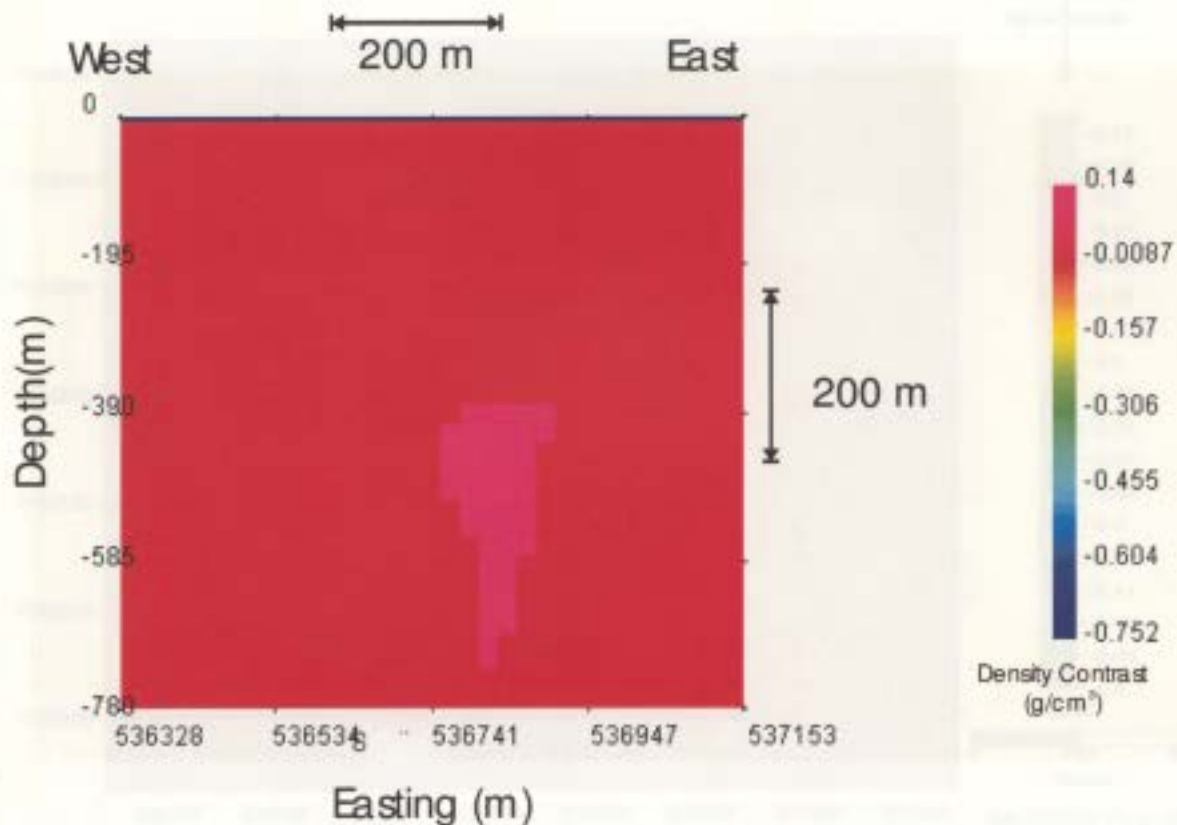


Figure 5.14: Density contrast model of the root zone for Pipe A154N. The pipe is completely surrounded by the host rock group in pink with a 5m thick layer of lake sediment on top of the host rock. The root zone kimberlite has a density that is slightly greater than the host rock leaving it difficult to discern therefore it was outlined in black. The root zone starts at approximately 400m and extends to a depth of approximately 750m.

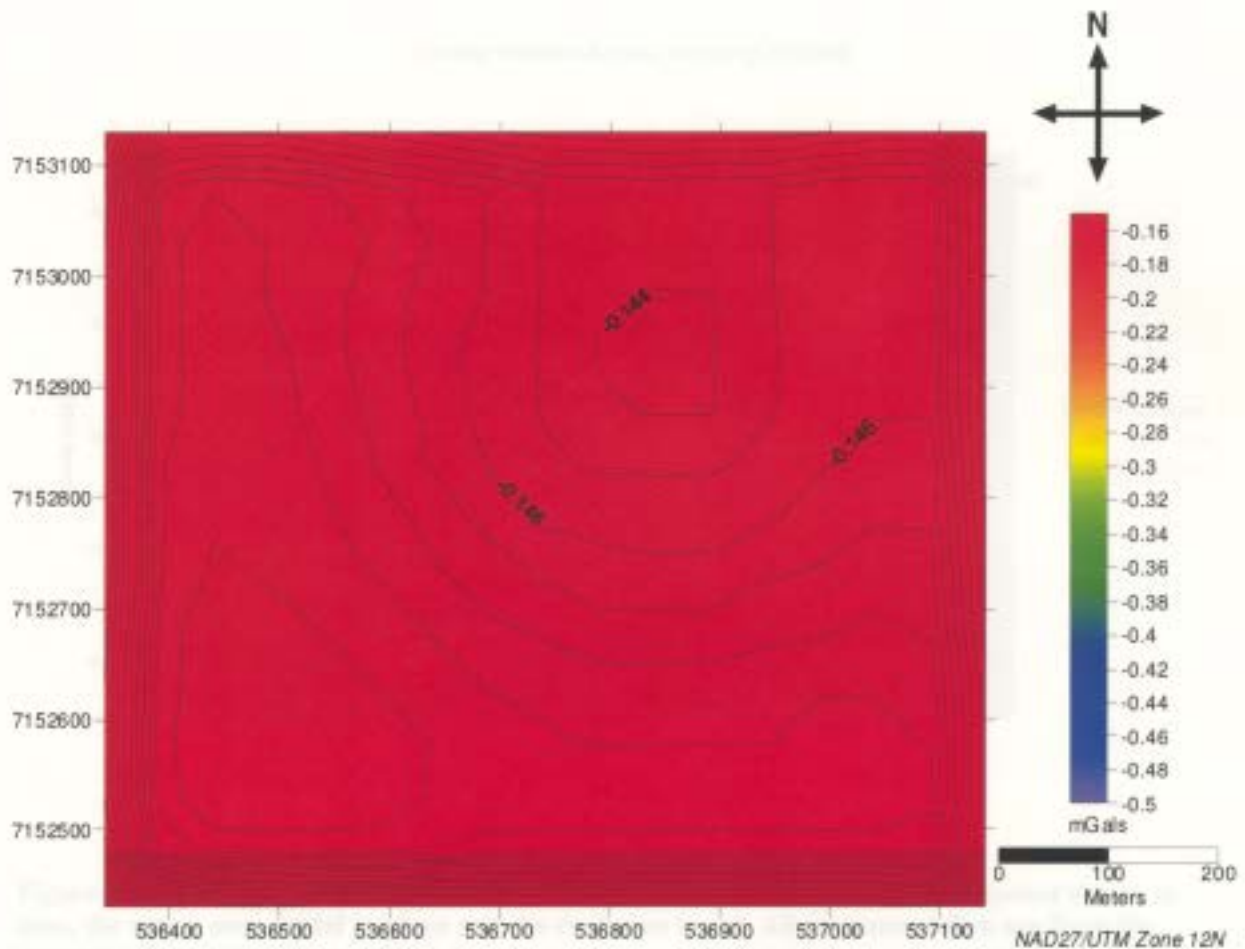


Figure 5.15: Forward modeling result of the density contrast model of the root zone for Pipe A154N as seen in Figure 5.14. This represents the ideal pipe signature with no noise. It provides little evidence to the existence of a subsurface kimberlite. It should be noted that the pattern seen in the contour lines around the edges the model limitations is caused by program limitations. Since the model used to represent pipe A154N is not infinite in size there is a contrast that occurs between where the model stops existing and infinite spaces begins. The presents of the pipe could be causing the circler contour lines that show a slight positive shift in the gravity response.

Gravity Profiles Across Northing 7152910

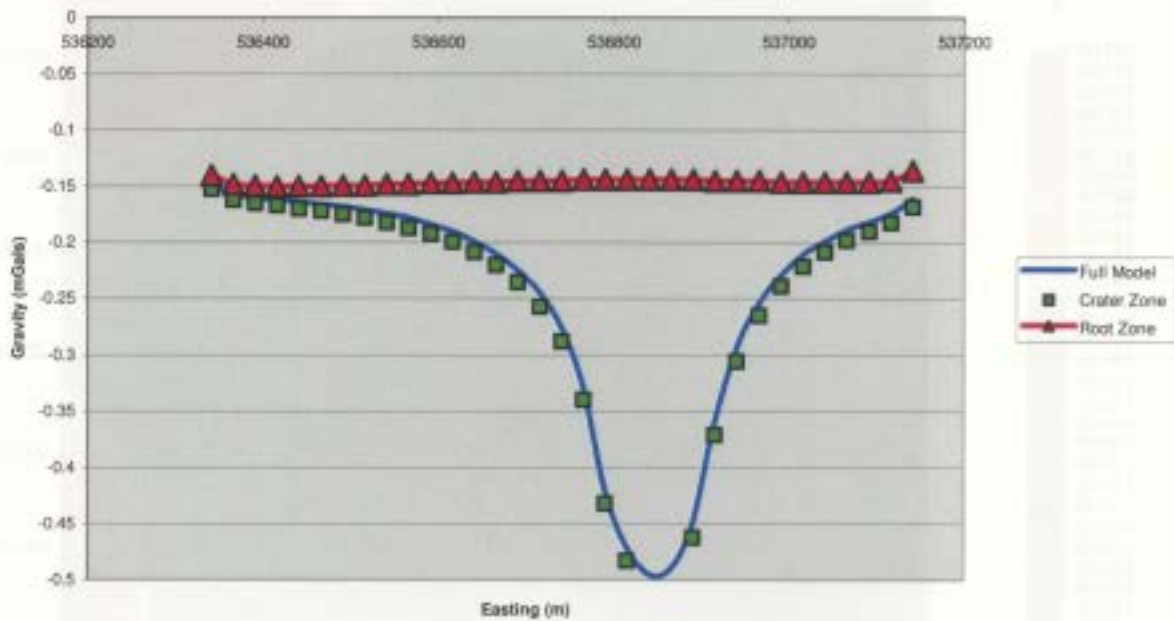


Figure 5.16: Gravity response of pipe A154N along 7152910N. The full model response shown in blue, the crater zone model in green and the root zone in red. All responses taken are from the respective forward model results.

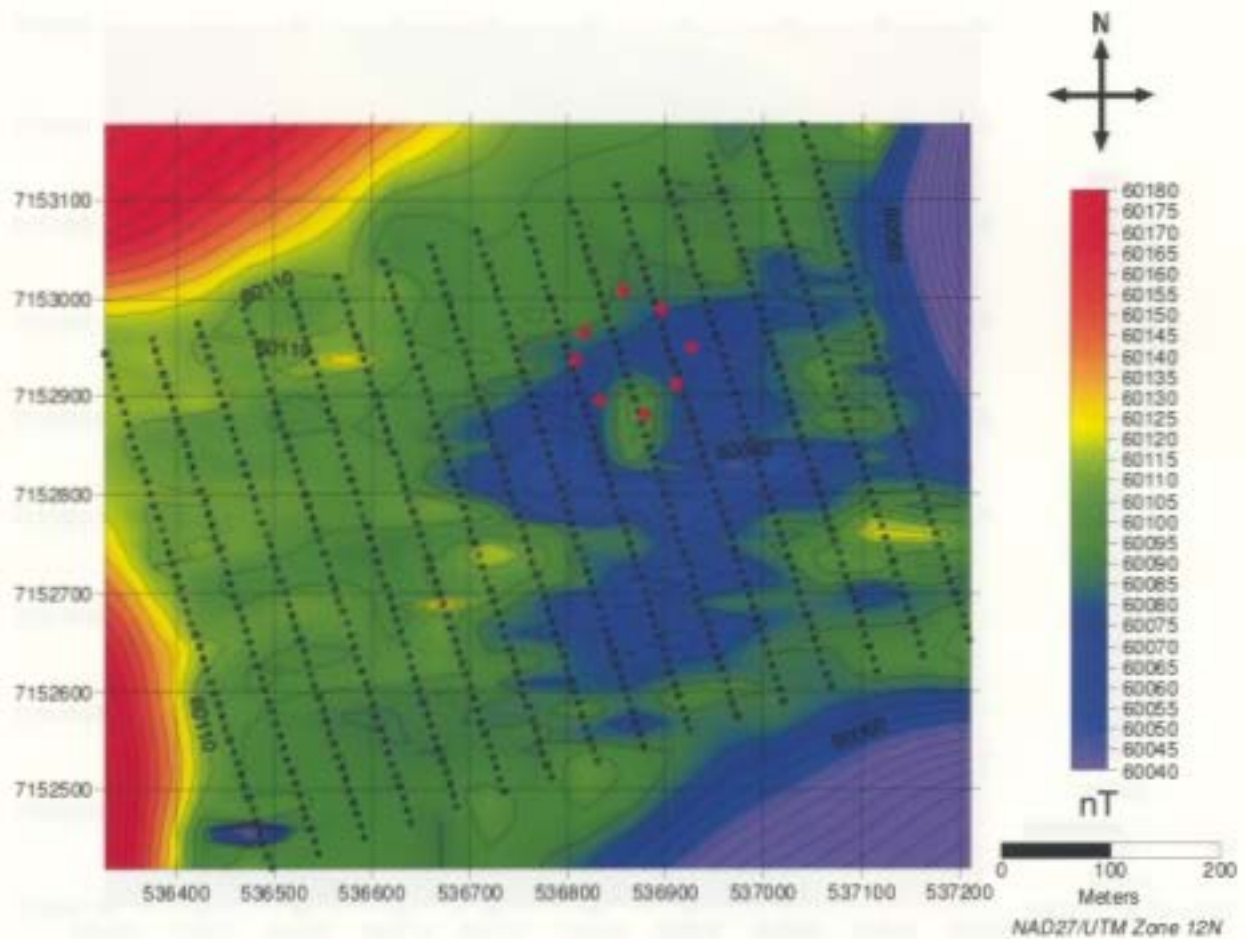


Figure 5.17: Total magnetic field data taken over pipe A154N. The outline of pipe A154N is marked with the red diamonds. The black boxes mark the data station locations.

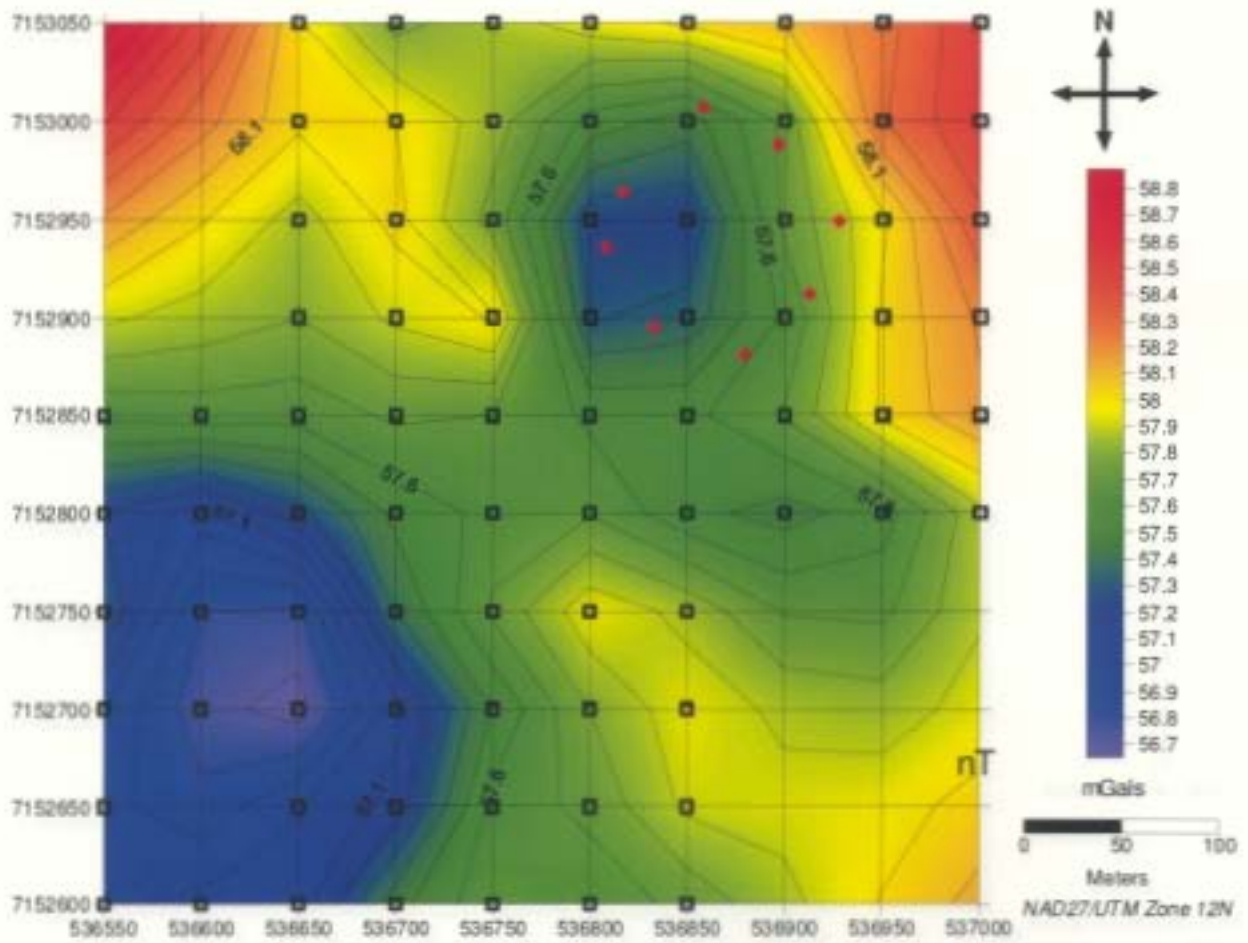


Figure 5.18: Gravity data collect on a 50m line by 50m station spacing grid. The outline of pipe A154N is marked with the red diamonds. The black boxes mark the gravity station locations.

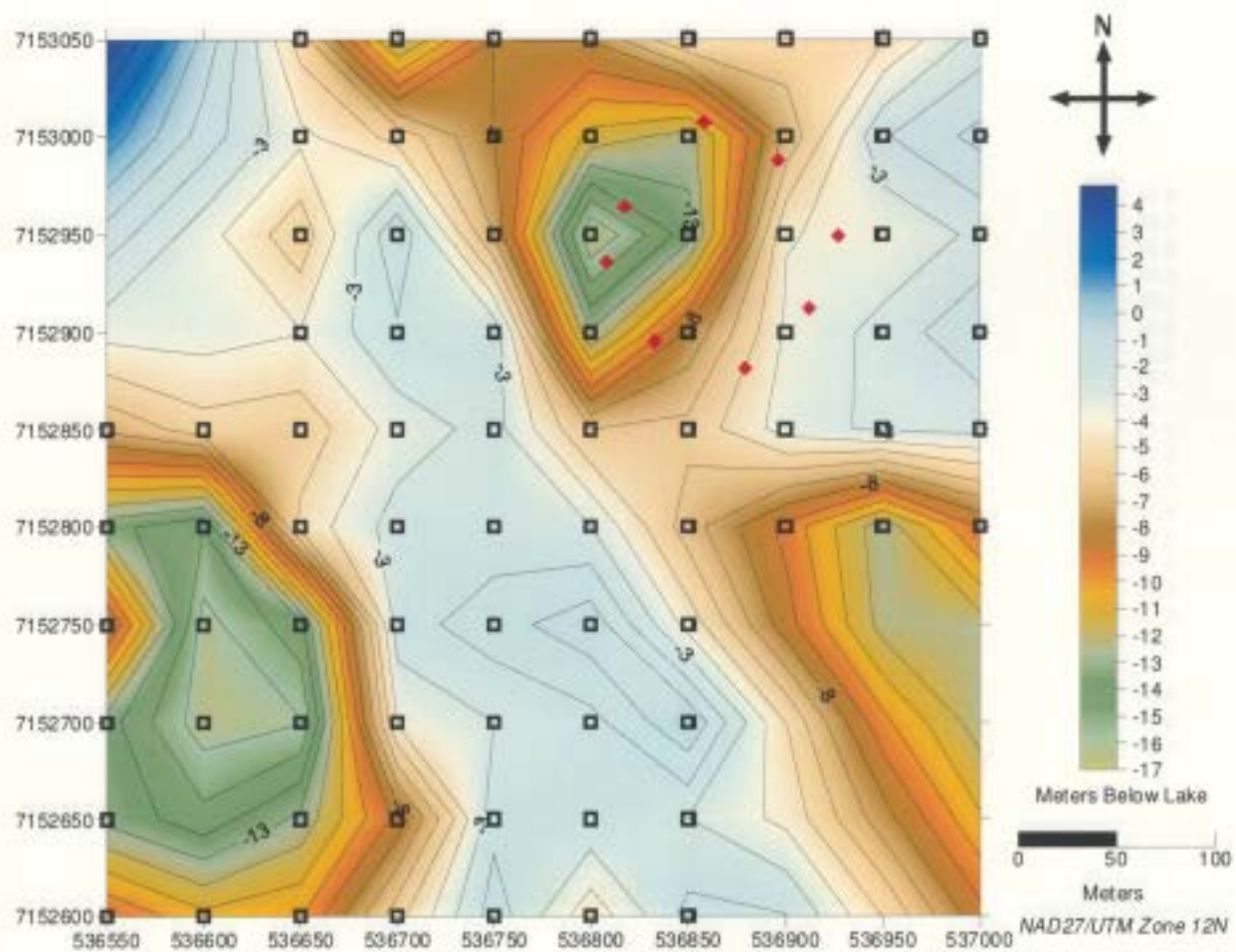


Figure 5.19: Bathymetry data collected at the same locations as the gravity data. The red diamonds indicate the location of pipe A154N and the locations of the bathymetry and gravity data collection stations are indicated by black boxes.

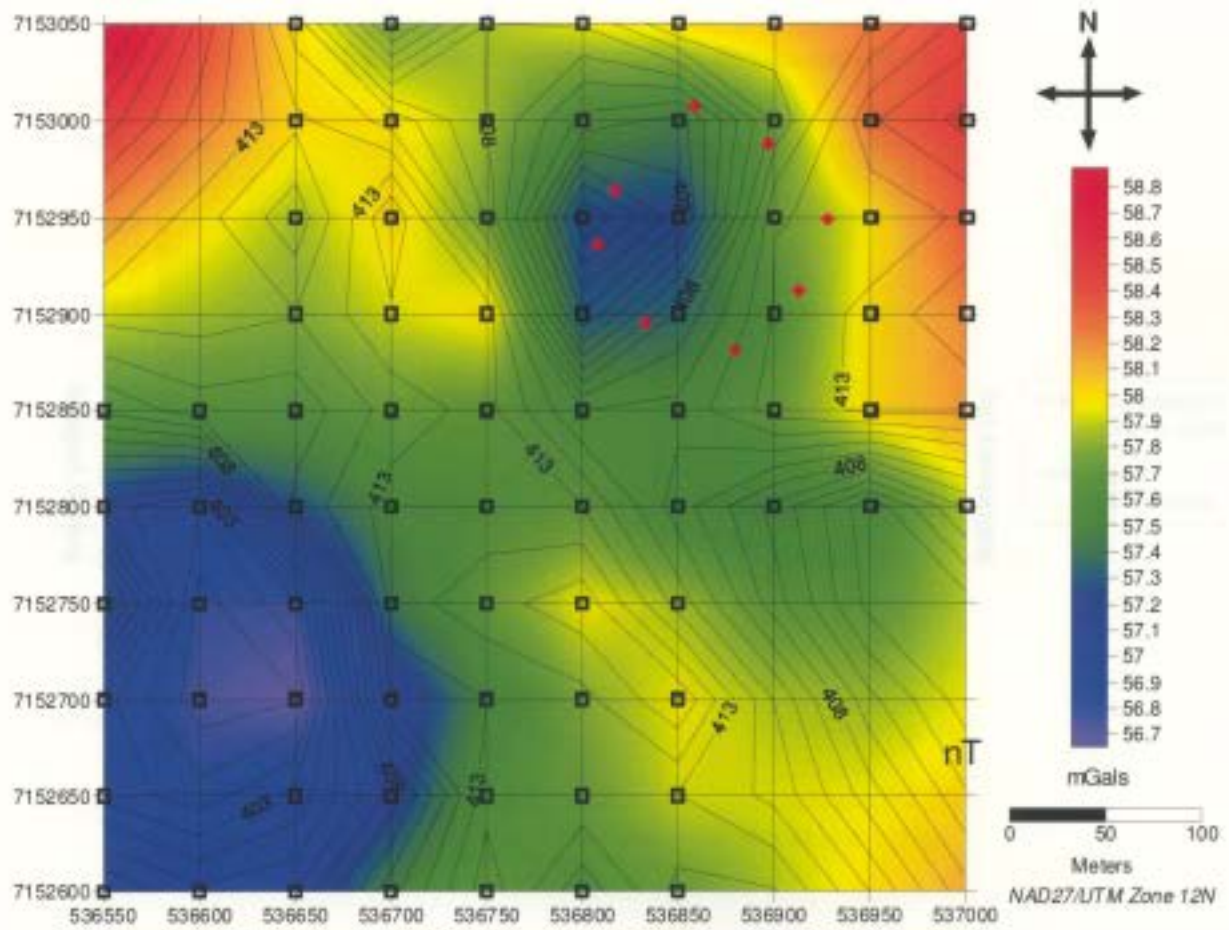


Figure 5.20: Colour gravity data map with bathymetry contours lines. The location of pipe A154N is indicated by red diamonds and the data collection location of gravity and bathymetry data are indicated by black boxes.

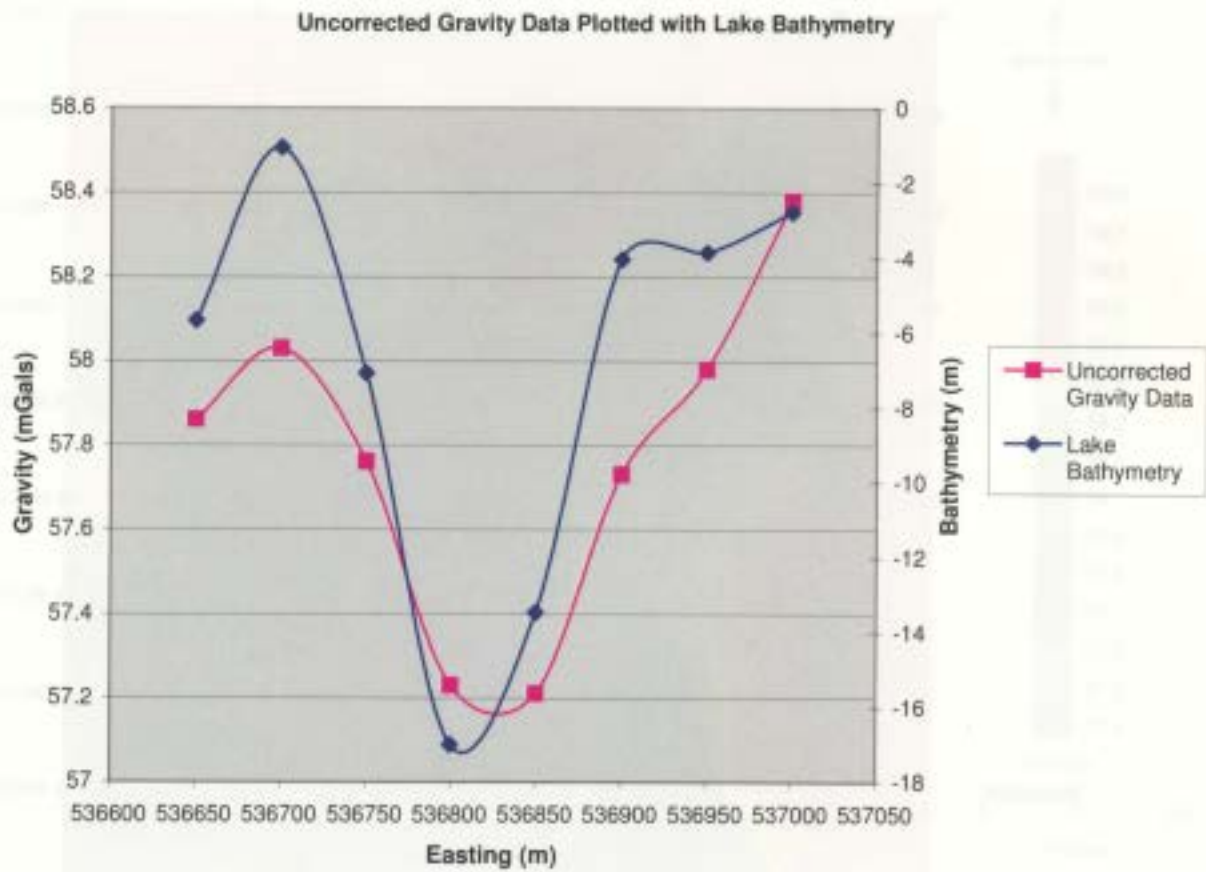


Figure 5.21: Profiles of gravity data and lake bathymetry running west to east across line 7152950N.

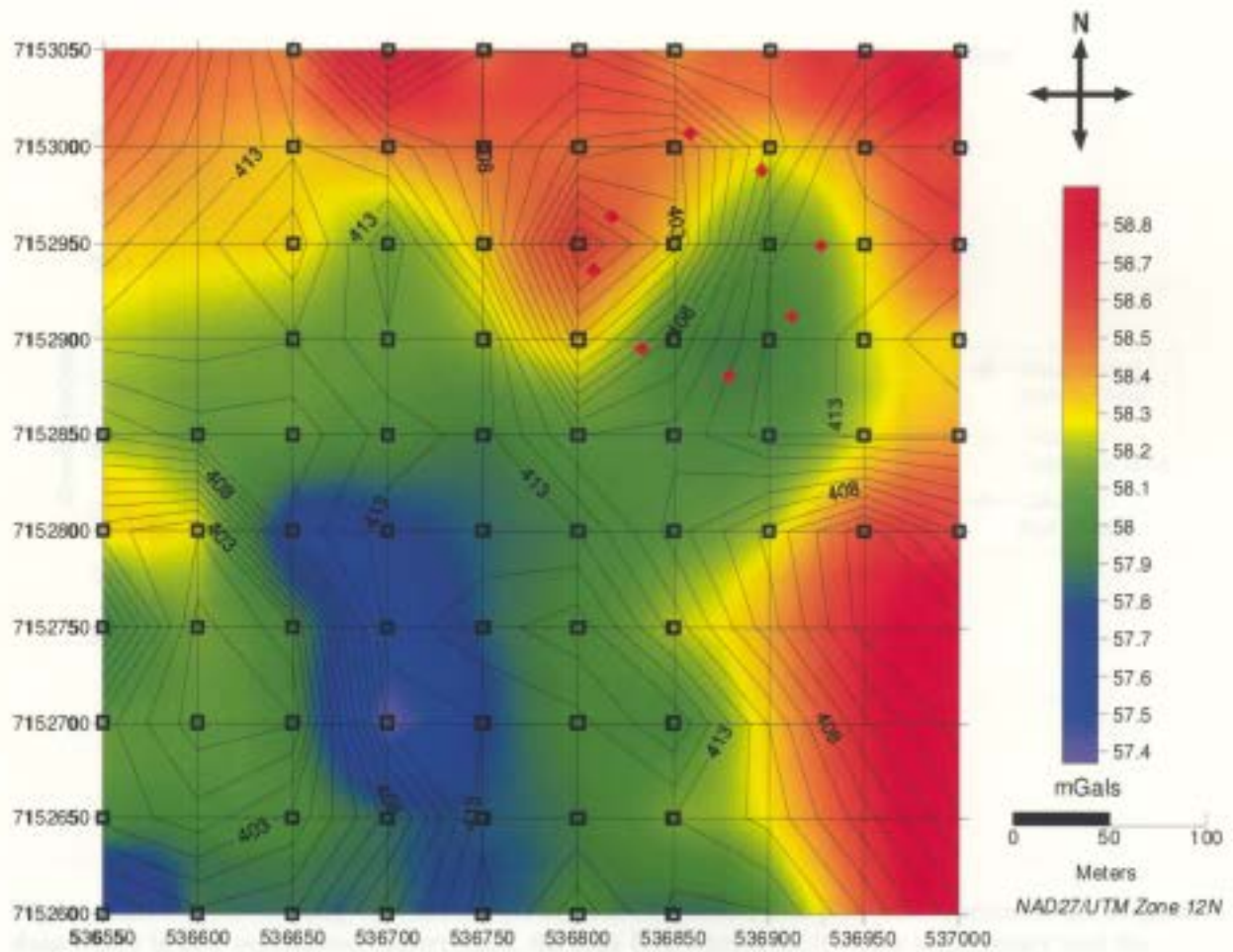


Figure 5.22: Bouguer corrected dataset with lake bathymetry contour lines. The location of pipe A154N is outline by red diamonds and the locations of the gravity data collect stations are marked with black boxes.

Uncorrected and Bouguer Corrected Gravity data with Lake Bathymetry Data

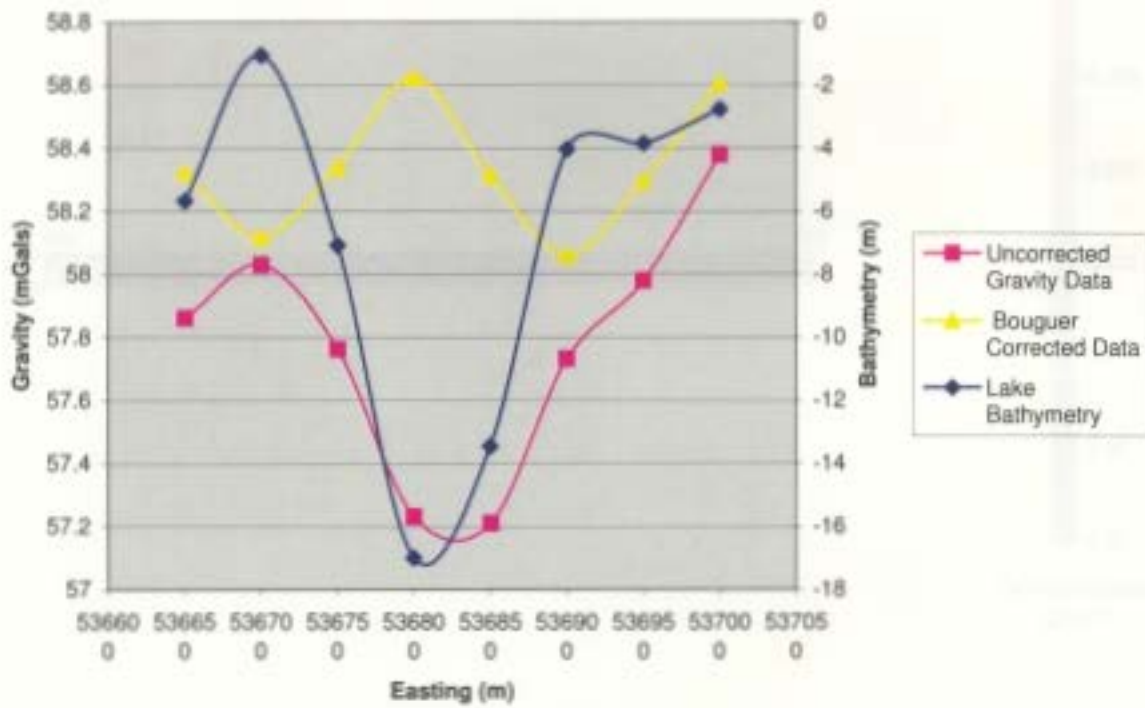


Figure 5.23: Profile running west to east across line 7152950N. The pink line represents the original data which is now considered uncorrected, the blue line represents the lake bathymetry and the yellow represents the Bouguer corrected data.

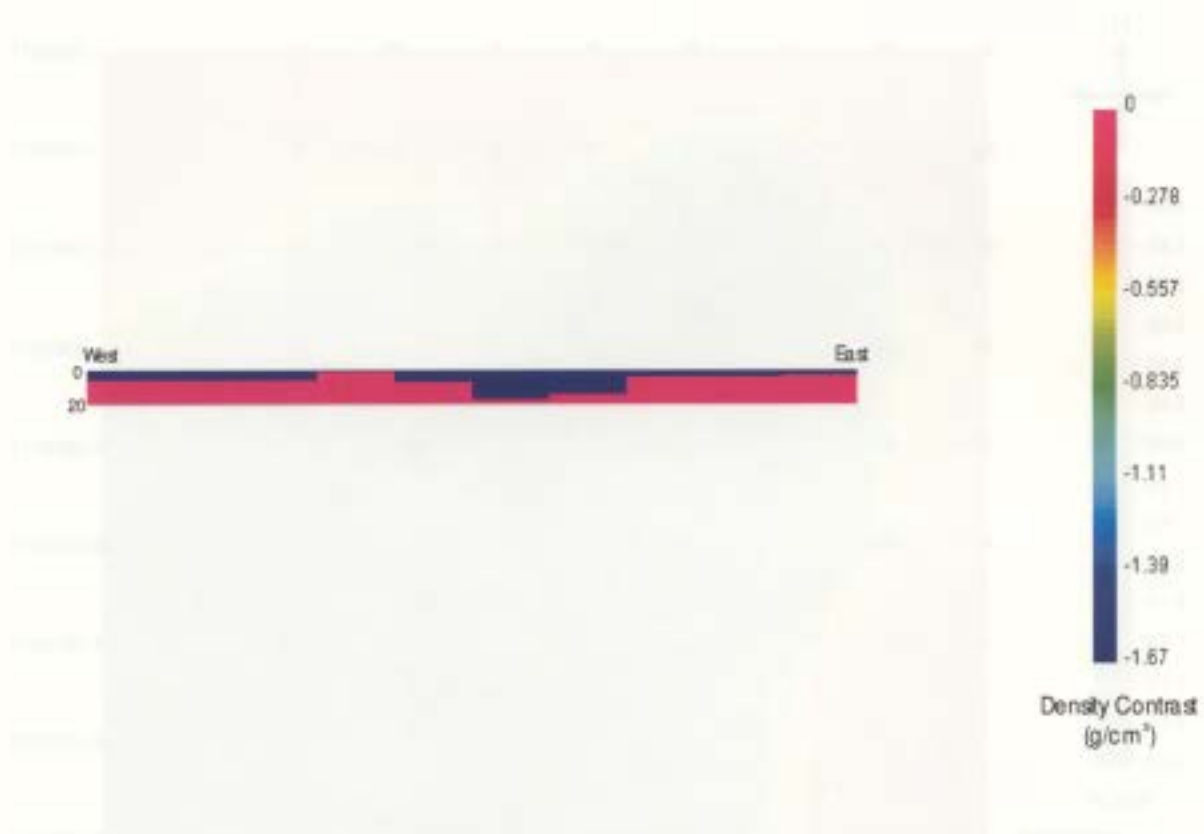


Figure 5.24: Density contrast model of the lake with water in blue and host rock in pink.

Figure 5.24: Density contrast model of the lake with water in blue and host rock in pink. The diagram shows a cross-section of the lake with a central channel and surrounding rock. The density contrast is highest in the central channel and lowest in the surrounding rock.

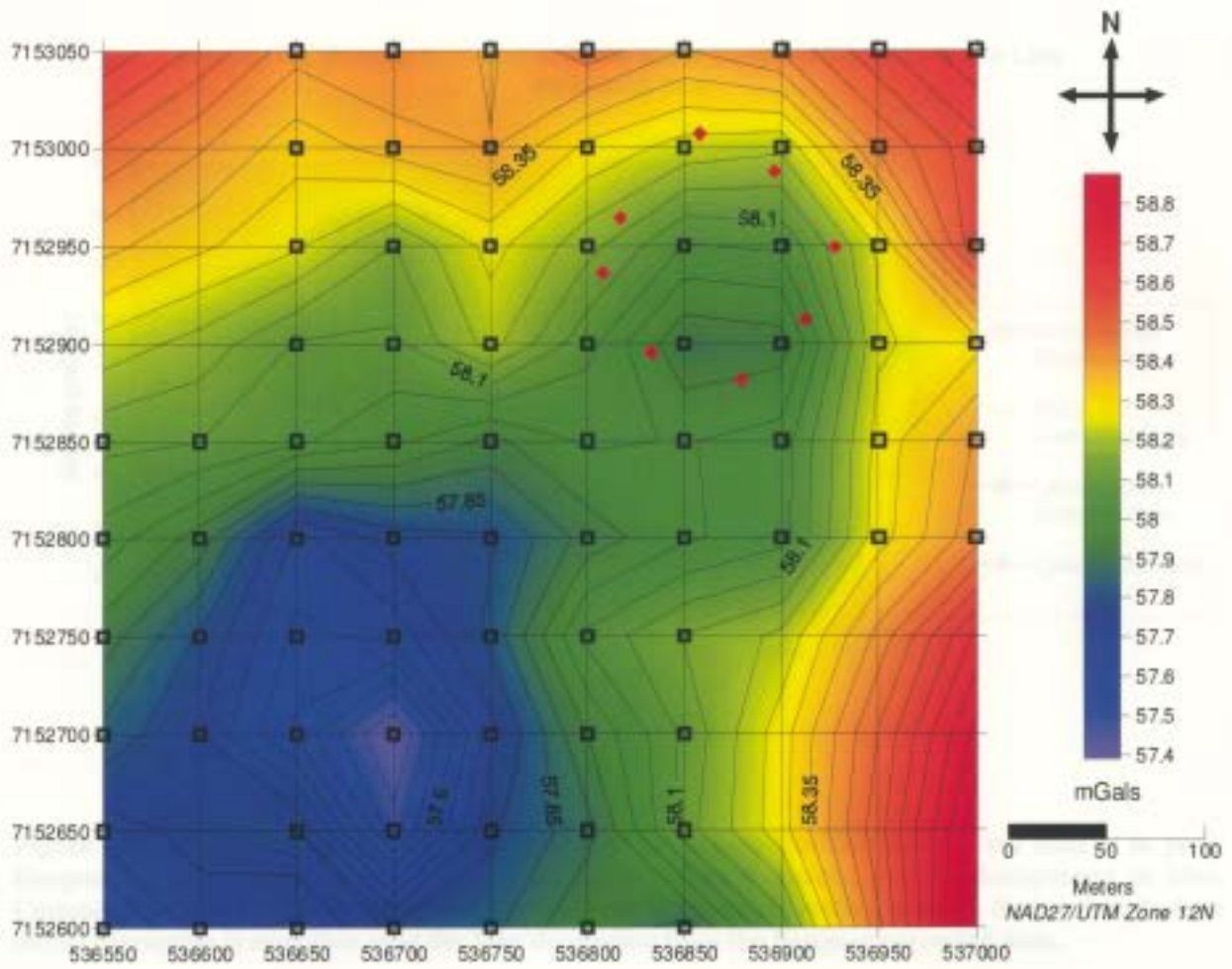


Figure 5.25: Gravity data after bathymetry corrections using the lake model method. The location of pipe A154N are indicated with red diamonds and the locations of the gravity and bathymetry data collection stations are indicated with black boxes.

Uncorrected, Bouguer Corrected and Lake Model Corrected Gravity Data with Lake Bathymetry Data

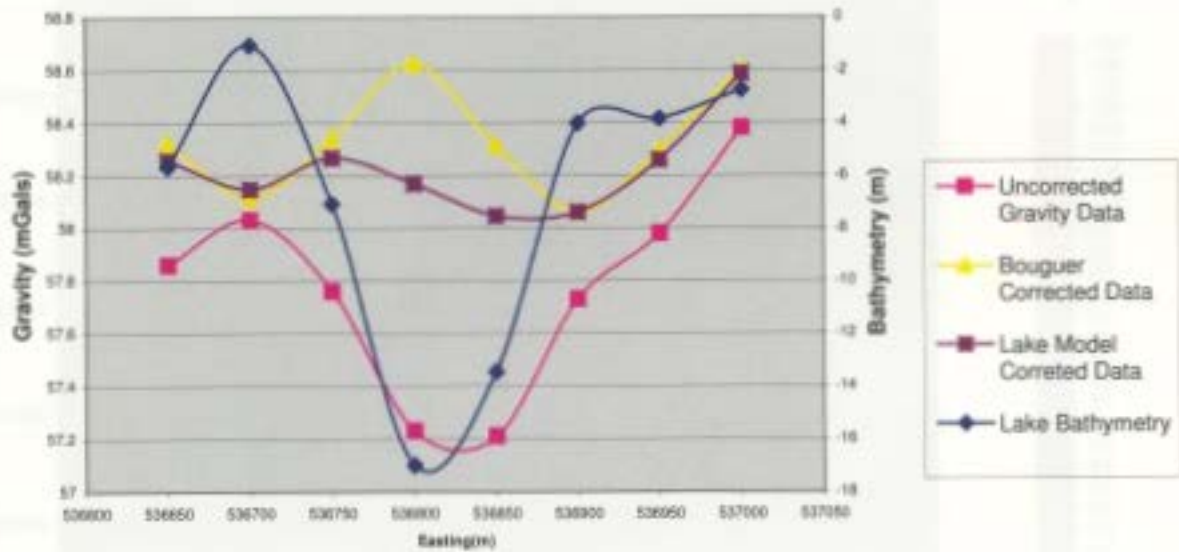


Figure 5.26: Profiles running west to east across line 7152950N. The uncorrected data is in pink, Bouguer corrected data in yellow, lake model correction in purple, and the bathymetry in blue. Compare the lake model correction method with the Bouguer correction method. Notice that the lake model correction is smoother over the lake depression than the Bouguer corrected data.

Figure 5.27: The contour map shows the gravity field of the lake. The map is derived from the data of Figure 5.26. It has contour lines that show the gravity field corrected to the lake level, which is available.

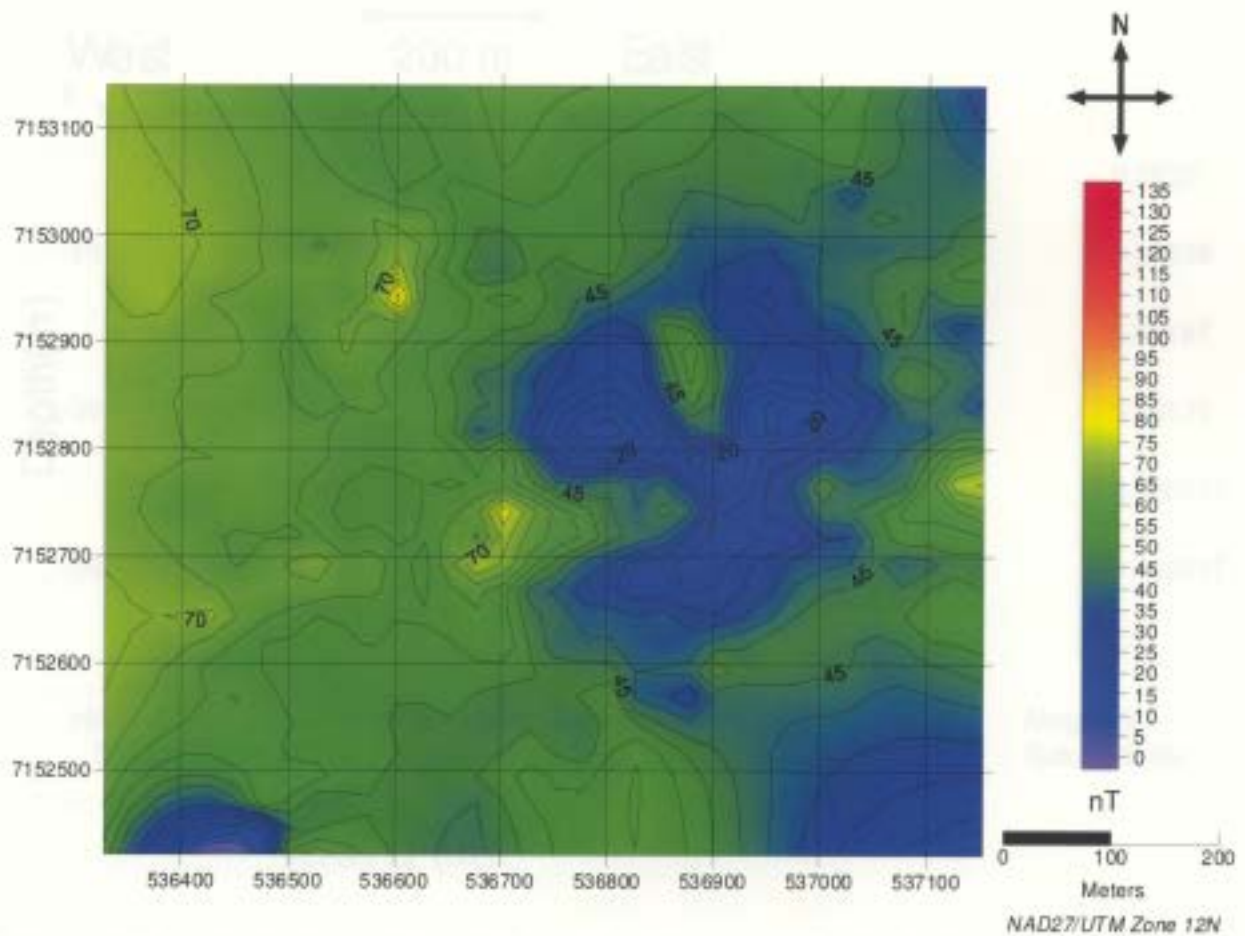


Figure 5.27: The observed magnetic dataset after removing the geomagnetic field of 60043nT. This map is a down scale revision of Figure 5.17. If you compare these two maps you will see slight changes due to gridding by Surfer which unavoidable.

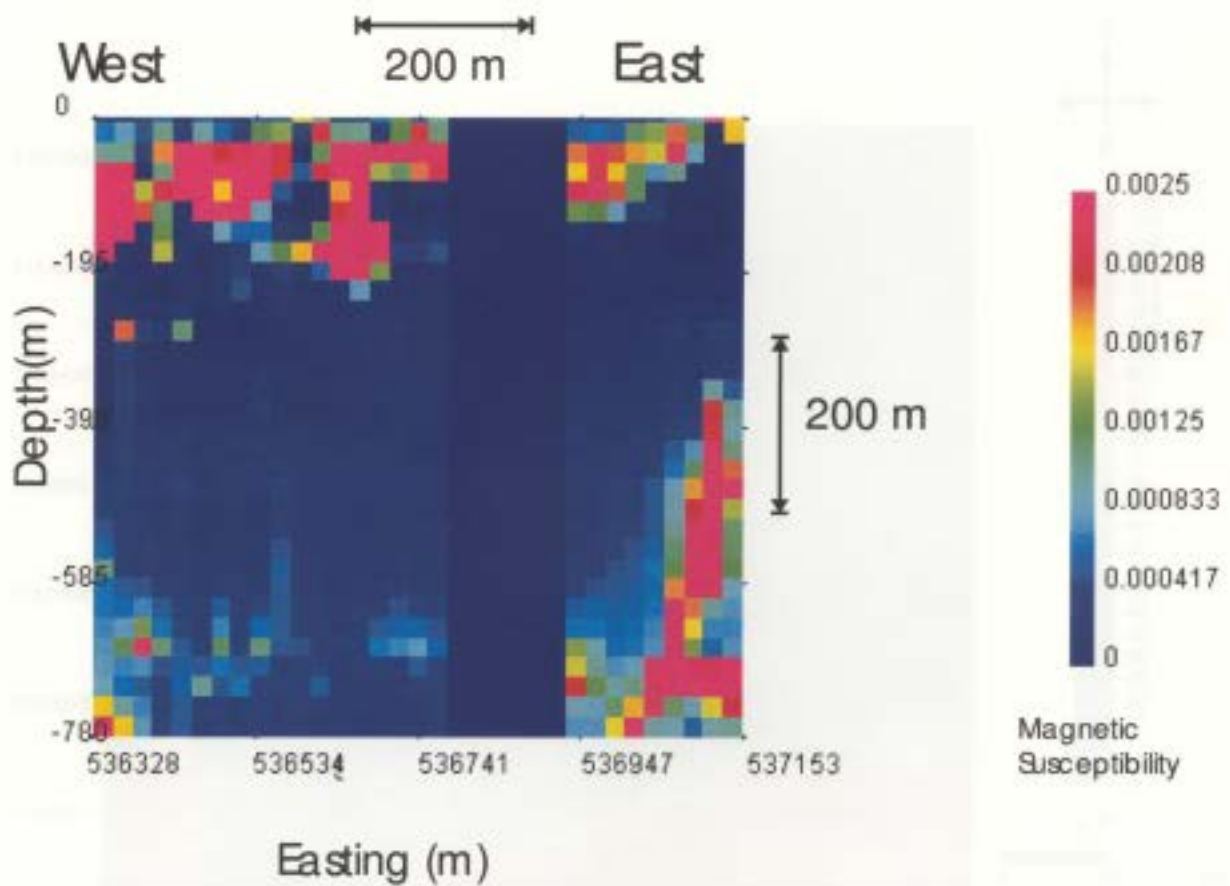


Figure 5.28: A depth slice running west to east across 7152900N with the location of pipe A154N zeroed or “stripped”. This model will be used to produce a forward model of the regional field.

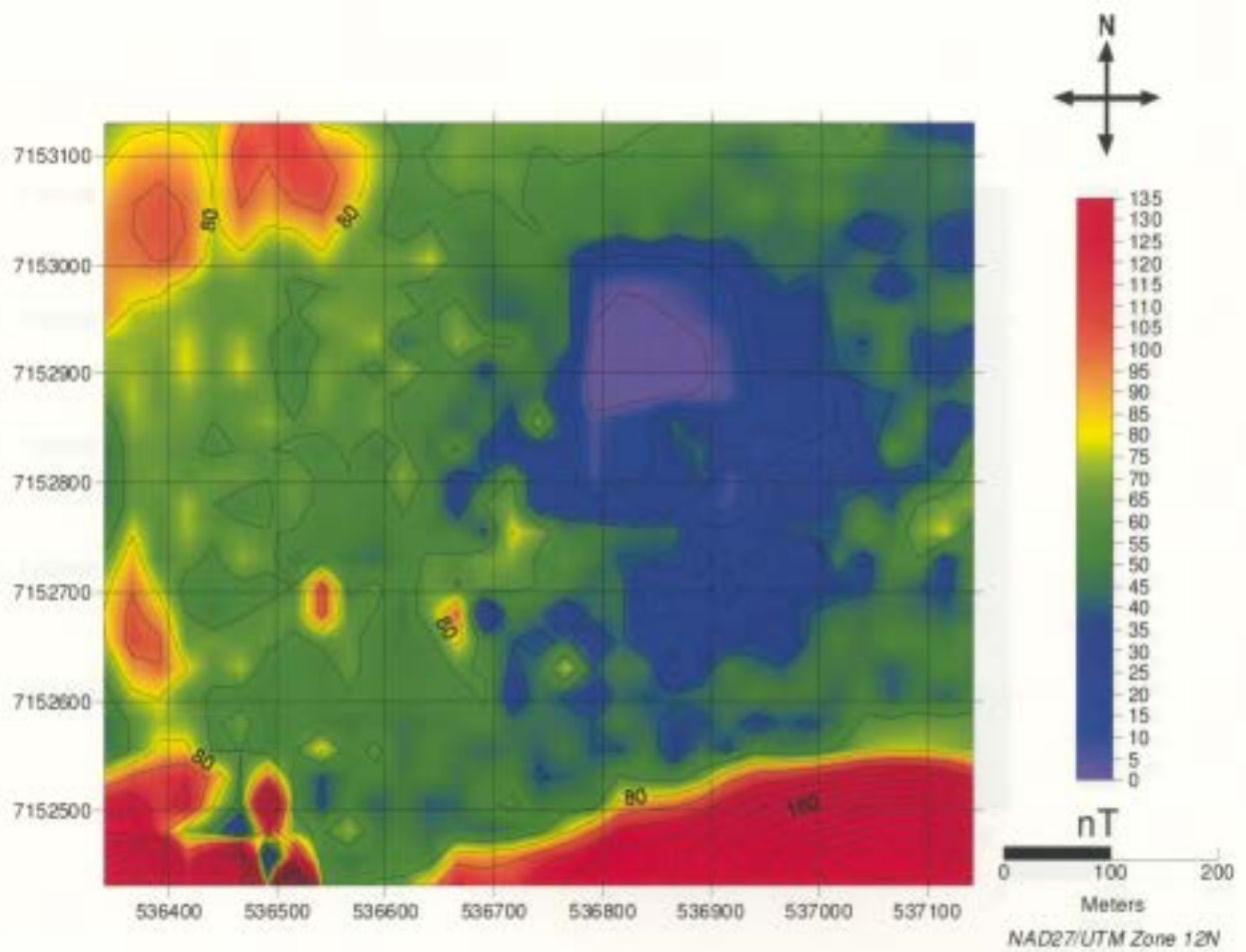


Figure 5.29: The resultant regional field produced from the model seen in Figure 5.28. This data is considered the regional field. It will be subtracted from Figure 5.27 resulting in the residual field seen in Figure 5.30.

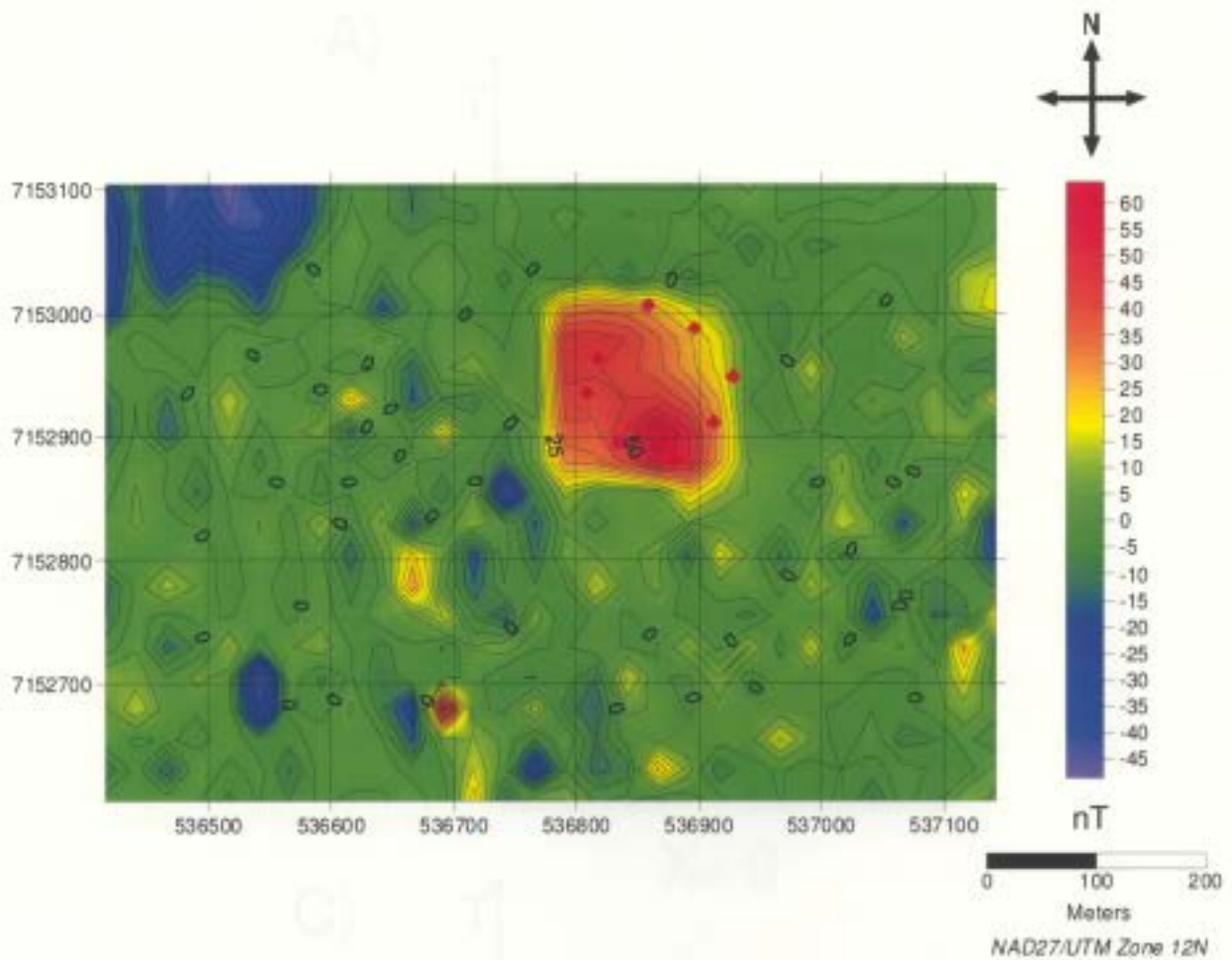


Figure 5.30: The residual field for pipe A154N. Note that the map was trimmed to focus on the pipe anomaly. Red diamonds outline the location of the pipe, which coincides well with the anomaly. The pipe anomaly has a maximum strength of 55nT.

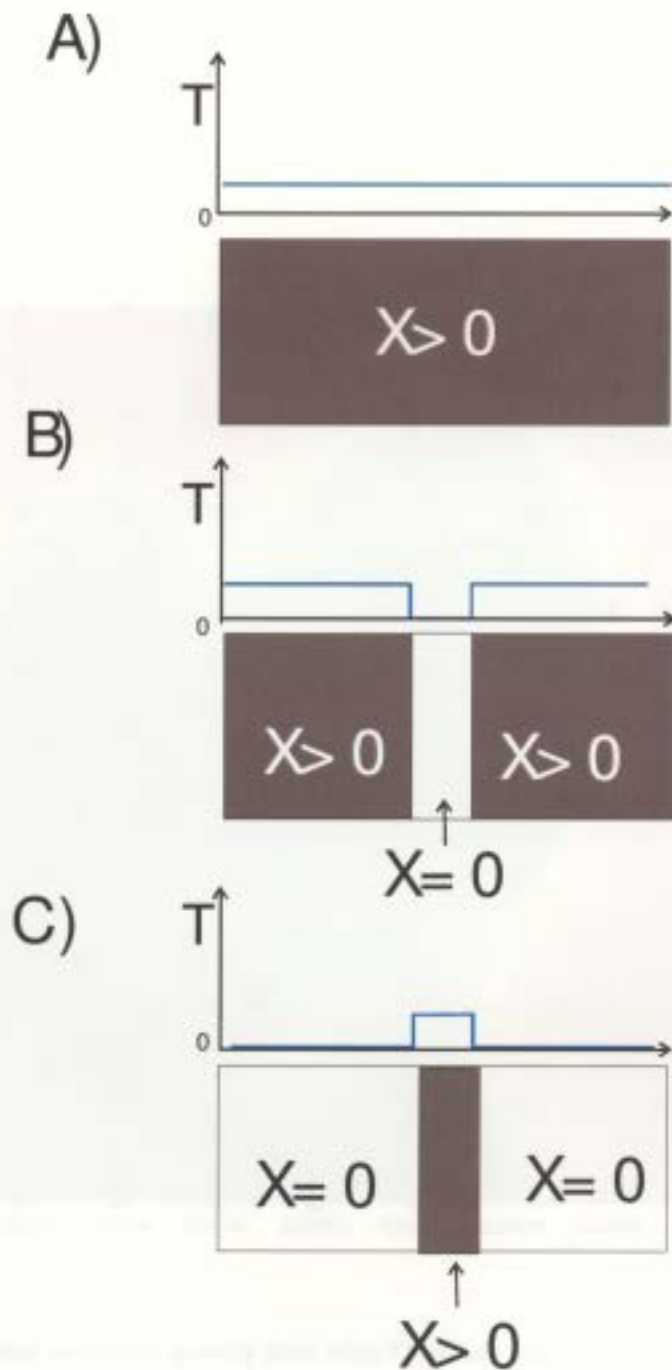


Figure 5.31: Cartoon to demonstrate the Li and Oldenburg regional/residual removal. A) The brown box represents a subsurface magnetic model with a constant magnetic susceptibility (X) of greater than zero. The resulting total magnetic field (T) is represent by the blue line, which is constant in A. B) The area of interest has been removed or "stripped" out with a susceptibility value equal zero. The resulting total magnetic field shows a drop over the stripped area. C) The box in A has been subtracted from the box in B. The result of this removal shows the stripped surface with susceptibility greater then zero and the surrounding areas are zero. The total magnetic field shows the resulting anomaly. The resulting anomaly is in-part due to the stripping process.

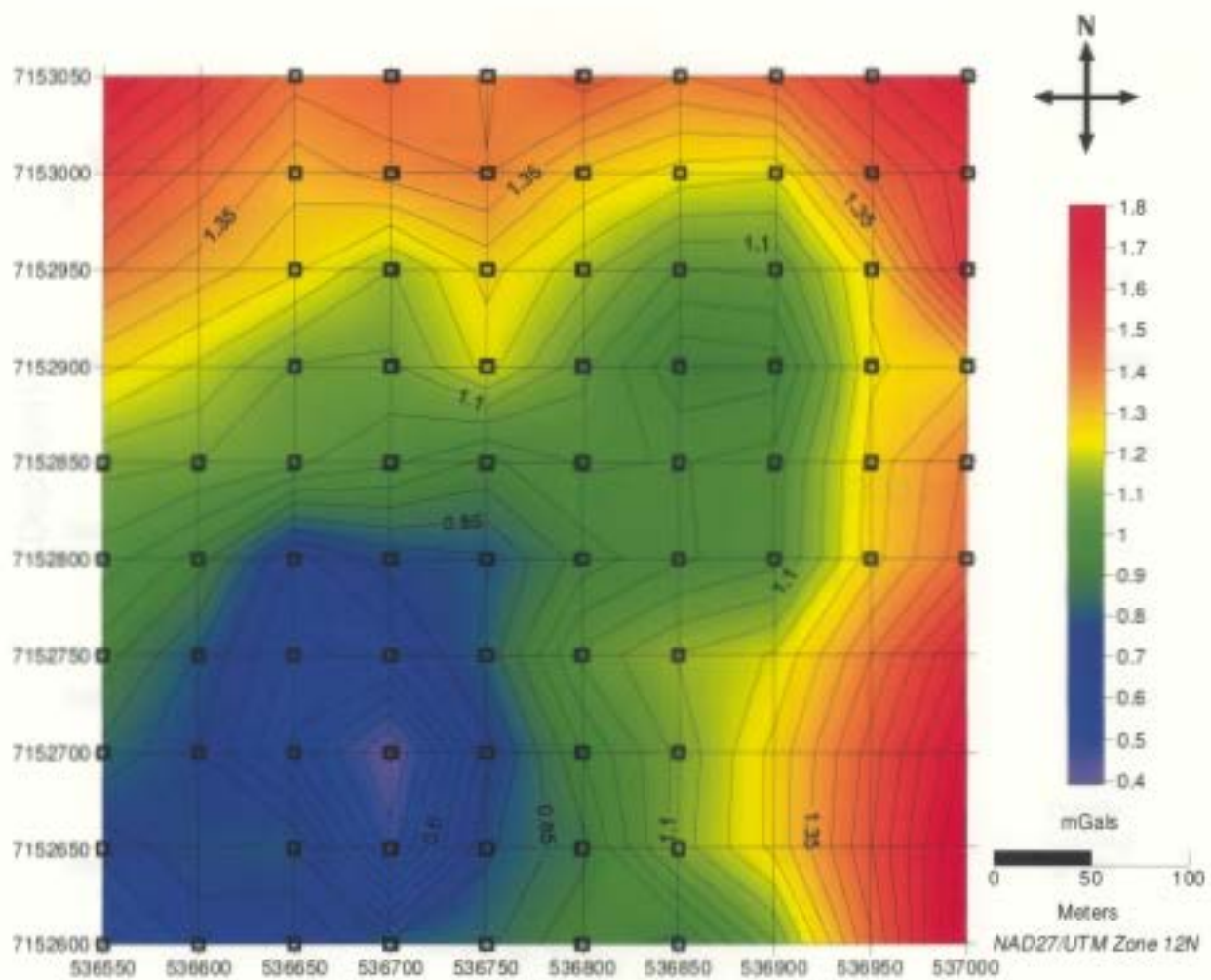


Figure 5.32: Lake method corrected gravity data with 57 mGals removed.

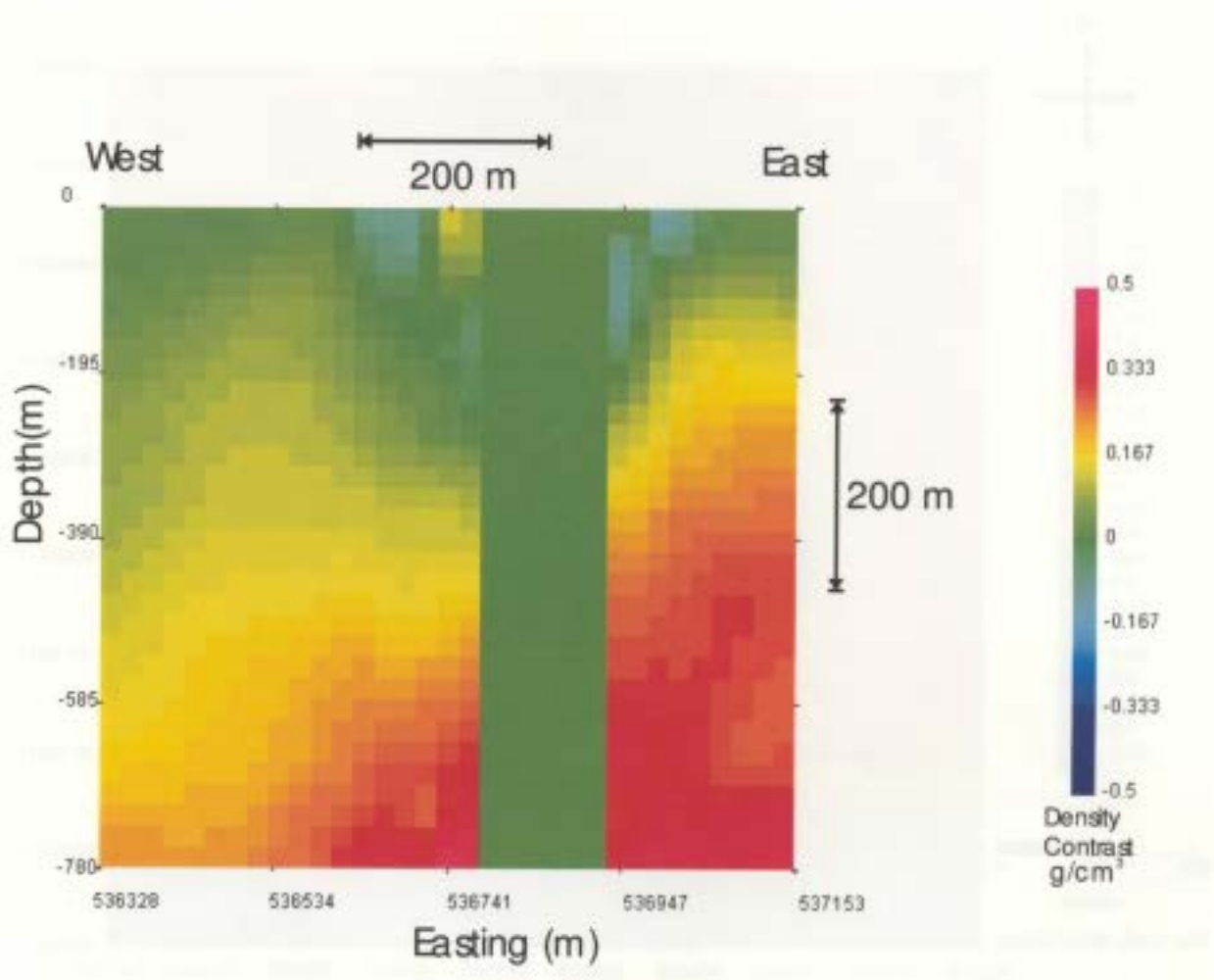


Figure 5.33: A depth slice of the gravity subsurface model running west to east across 7152900N with the location of pipe A154N zeroed or “stripped”. This model will be used to produce a forward model of the regional field.

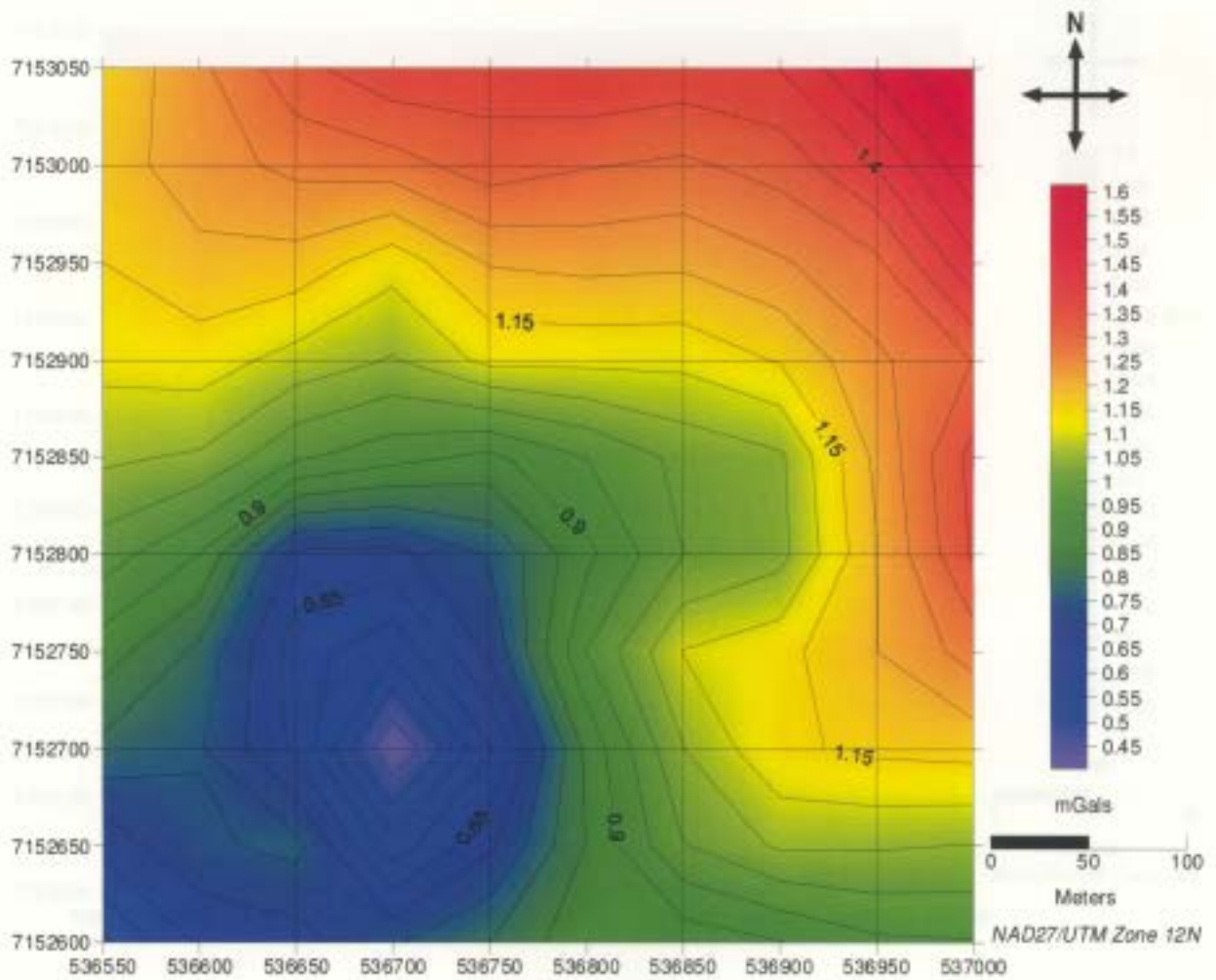


Figure 5.34: Map of the regional data for the gravity data resulting from a forward model of Figure 5.33. This data will be subtracted from Figure 5.32 resulting in the residual field seen in Figure 5.35.

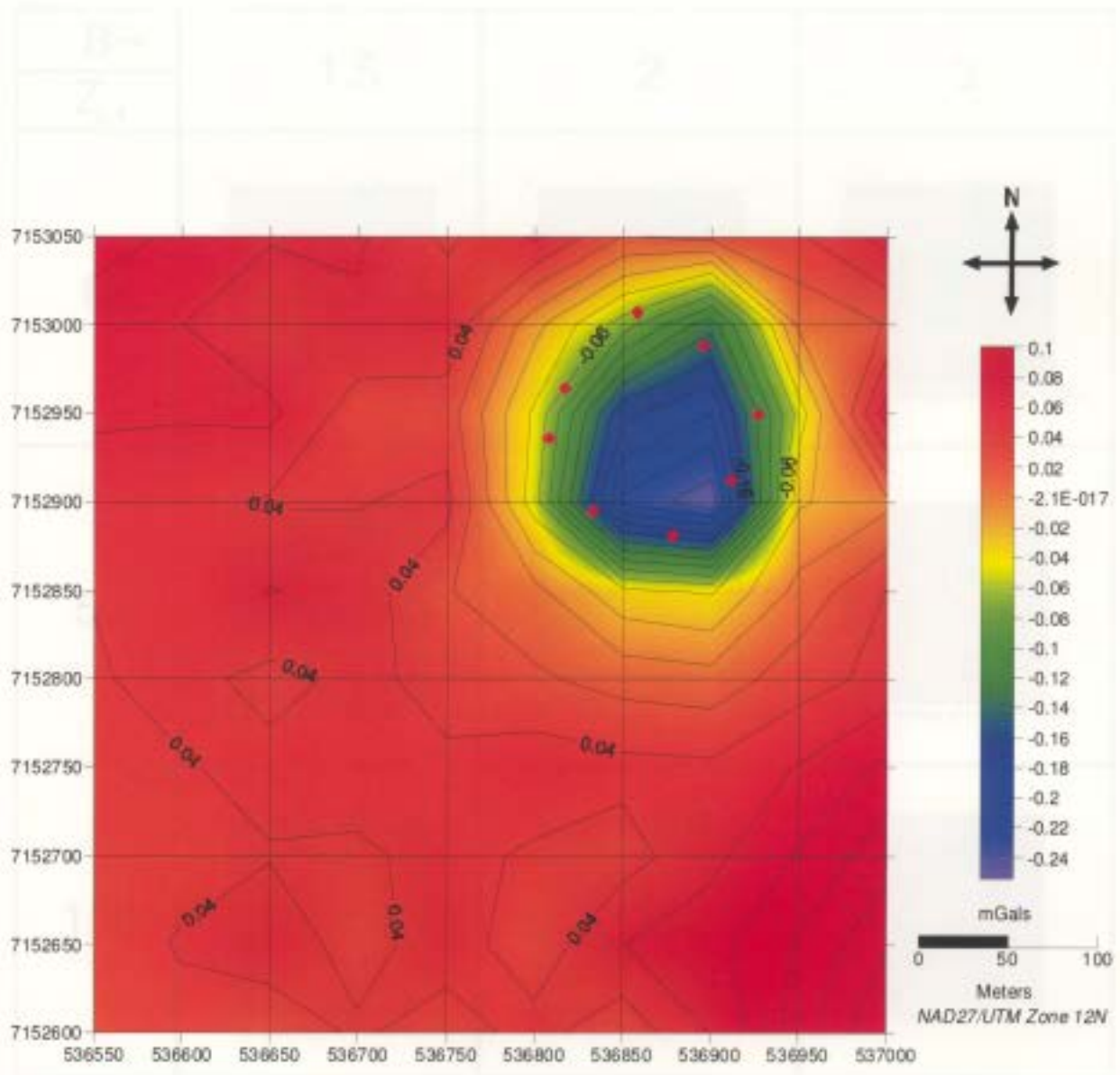


Figure 5.35: The residual gravity results for pipe A154N. Red diamonds outlines the location of the pipe, which coincides with the pipe anomaly. The pipe anomaly has a strength of -0.24mGals .

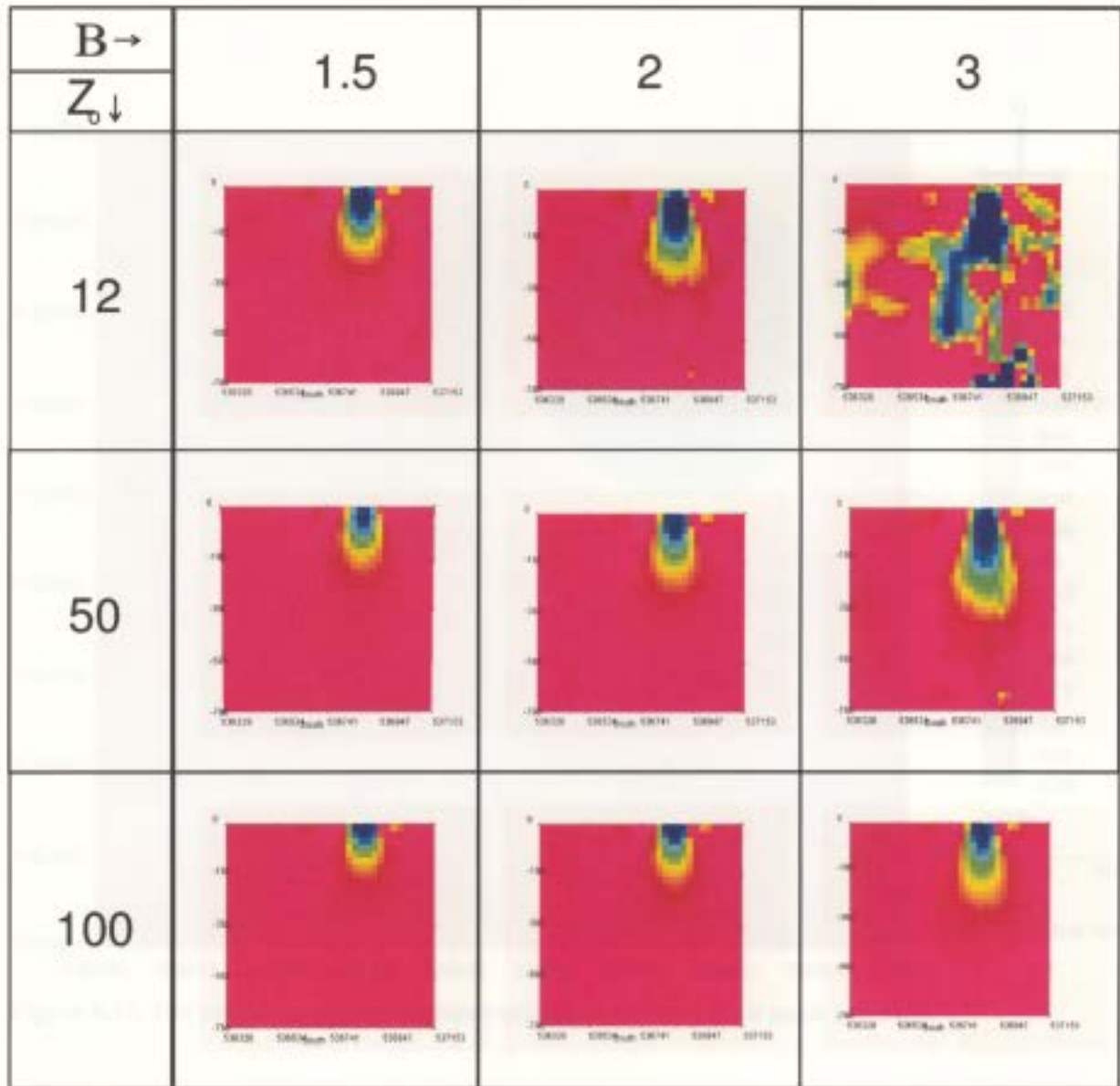


Figure 5.36: All gravity subsurface models were produced over the same dataset with various z_0 and β values and are shown on the same colour scale. This experiment was performed by varying both parameters and testing their effects upon the results of the inversion. Values of z_0 shown here include 12, 50 and 100 and values β shown include 1.5, 2, and 3. After considering these combinations it was determined that the combination of z_0 at 50 and β at 3 produced the fuzzy blob with the features closest to kimberlite pipe A154N for gravity.

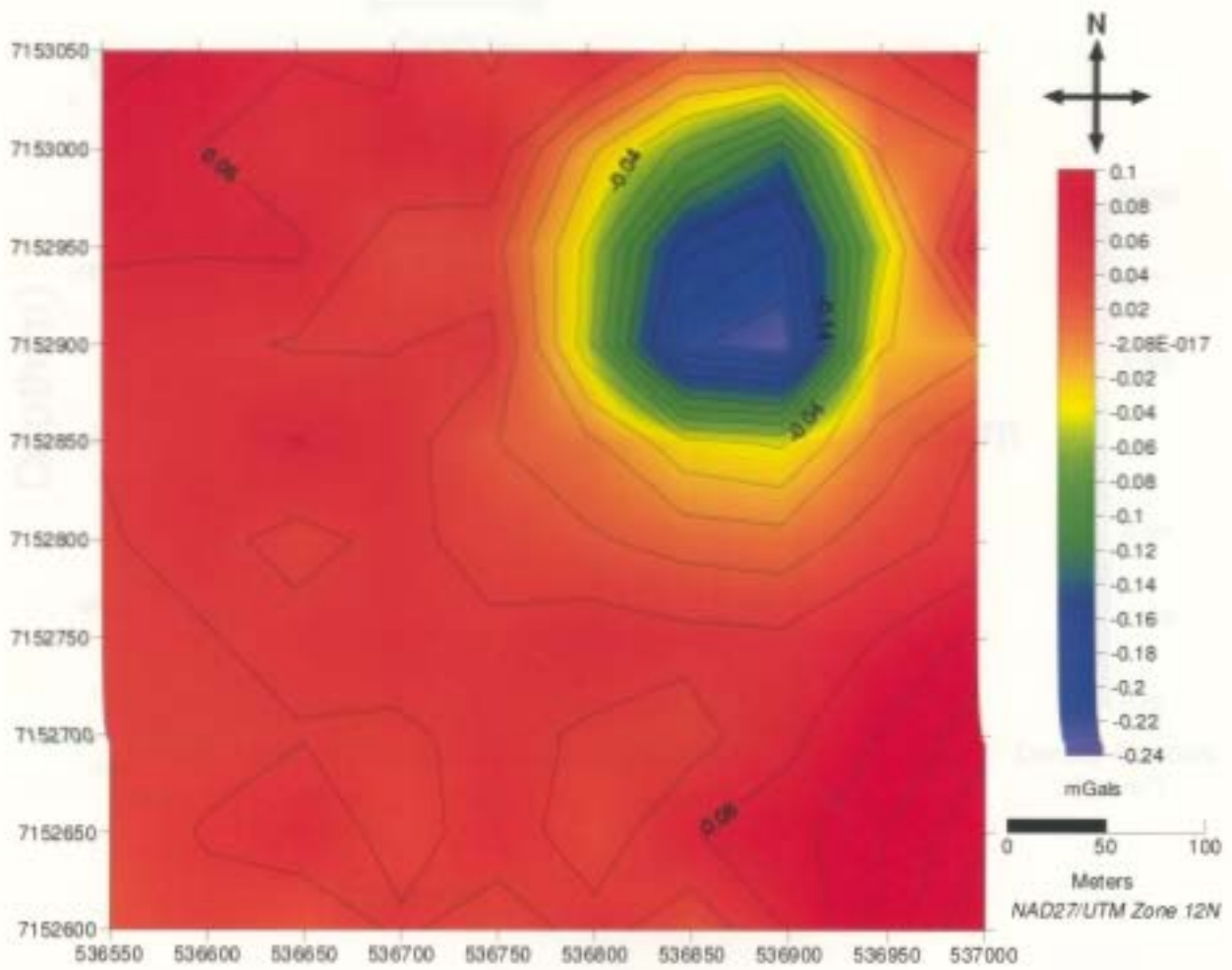


Figure 5.37: The predicted gravity dataset resulting from the *default mode* inversion

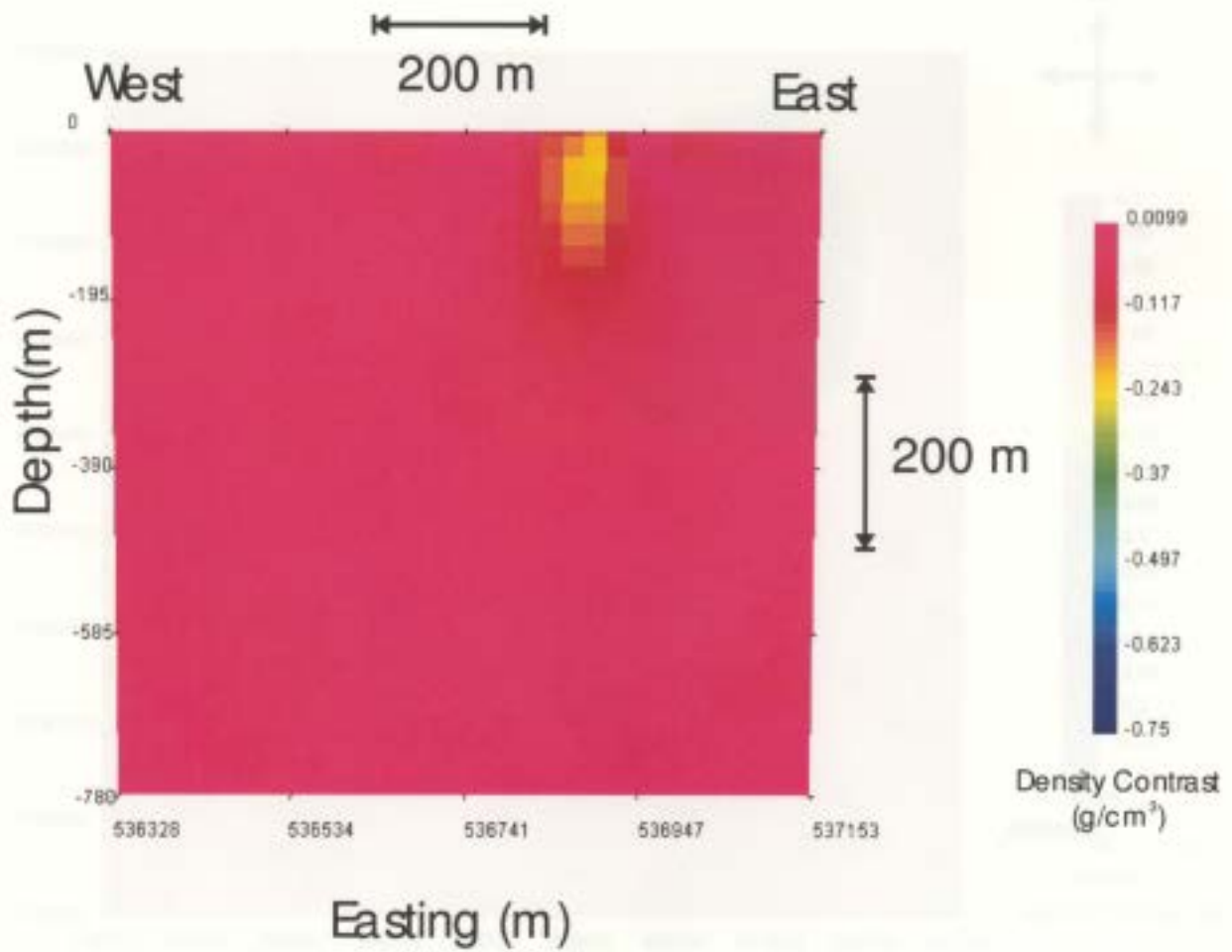


Figure 5.38: A depth slice running west to east across 7152900N of the density contrast model produced by the *default mode* inversion.

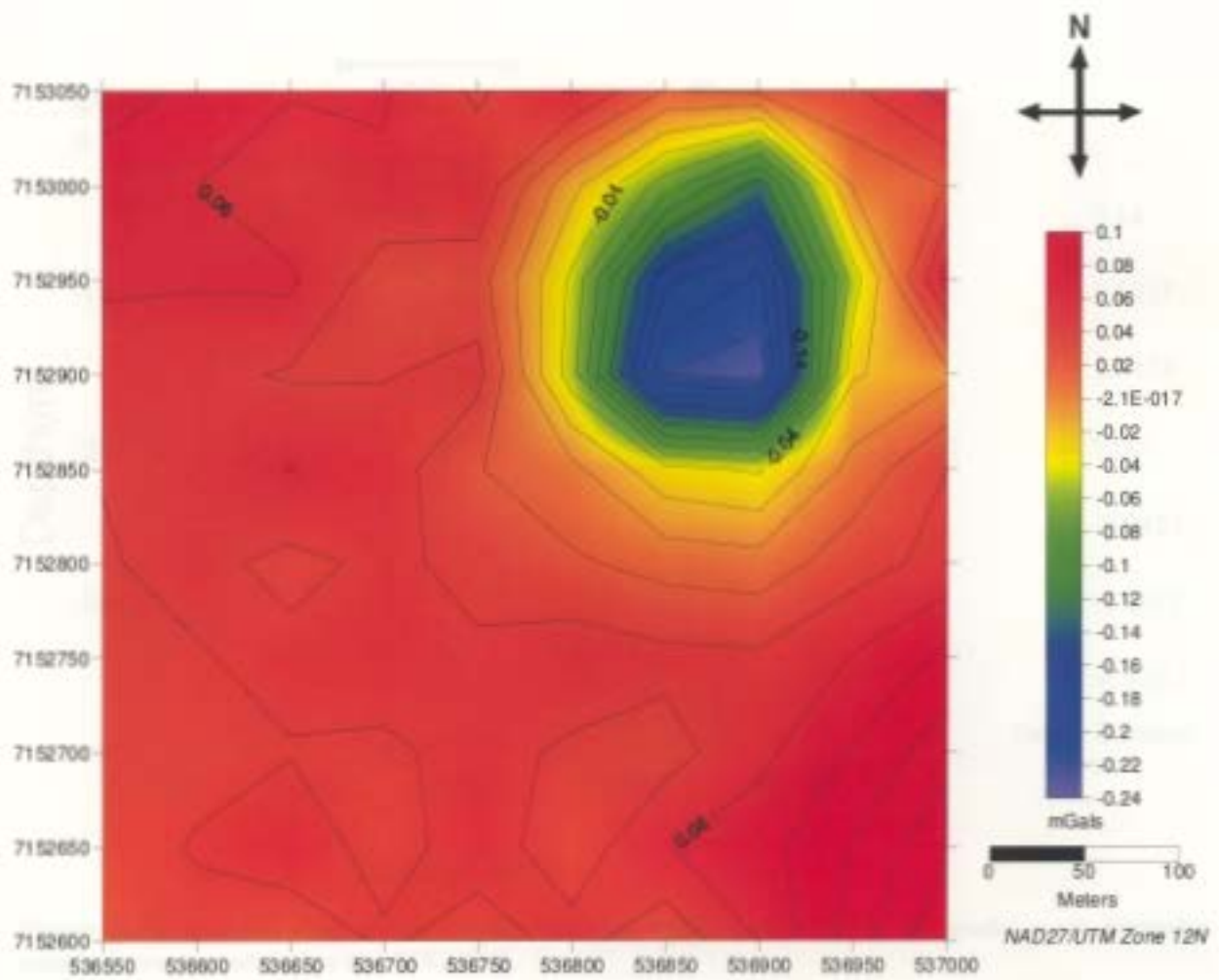


Figure 5.39: The predicted dataset resulting from the *model mode* inversion.

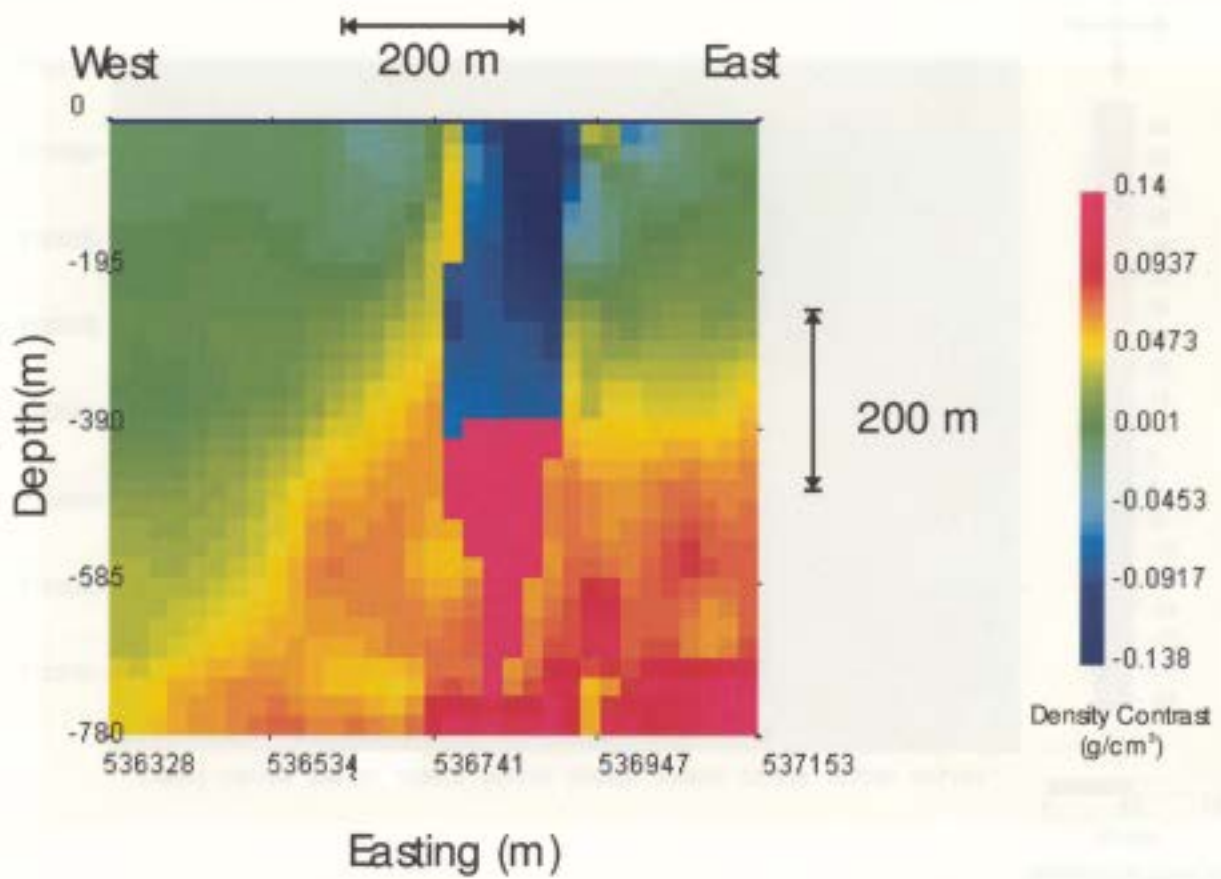


Figure 5.40: A depth slice of the density contrast model produced by the *model mode* inversion running west to east across line 7152900N.

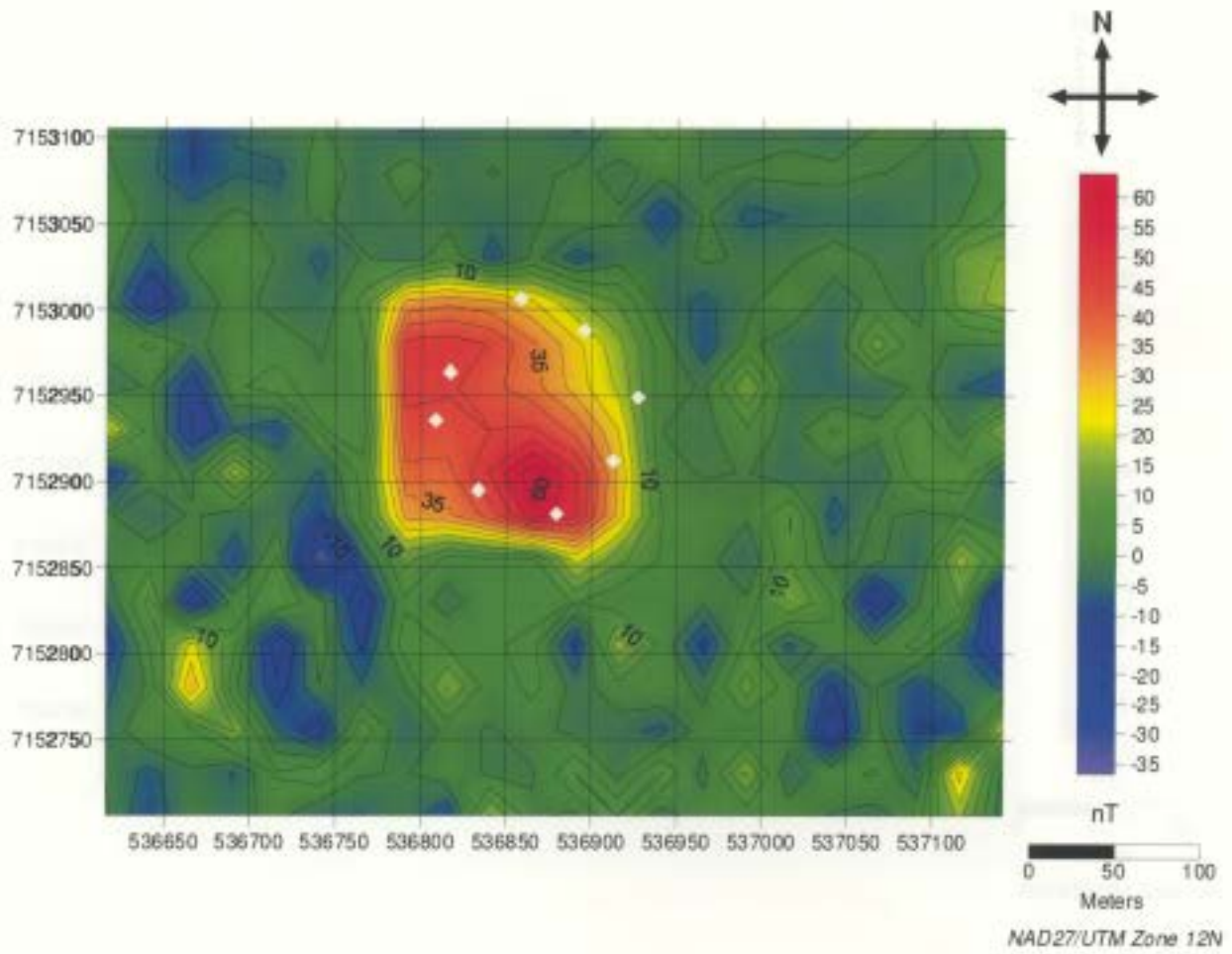


Figure 5.41: Trimmed residual total magnetic field data used in the MAG3D inversions. The location of pipe A154N is marked with white diamonds.

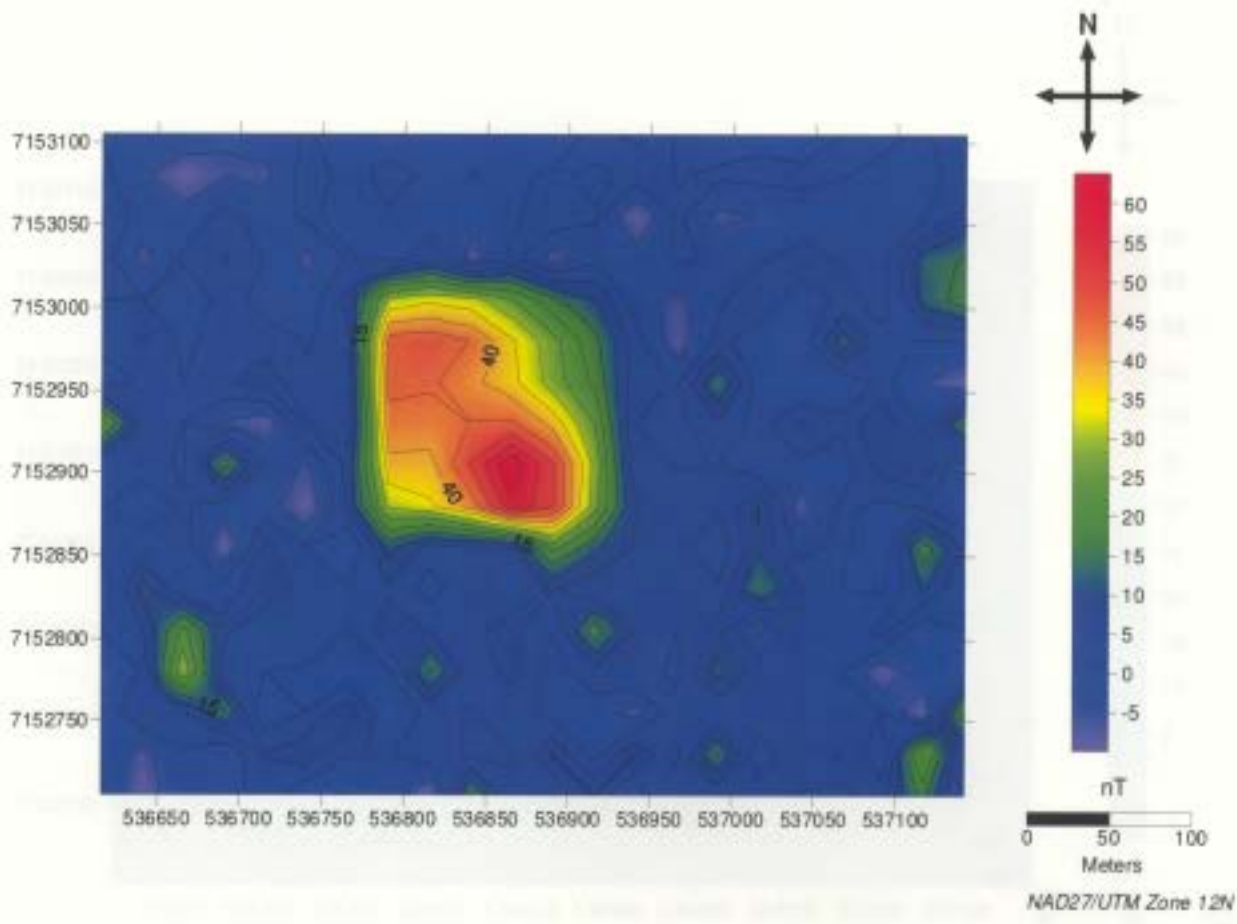


Figure 5.42: Some extreme data points were re-set to zero. These are points that are not associated with the kimberlite pipe and were interfering with the inversion process.

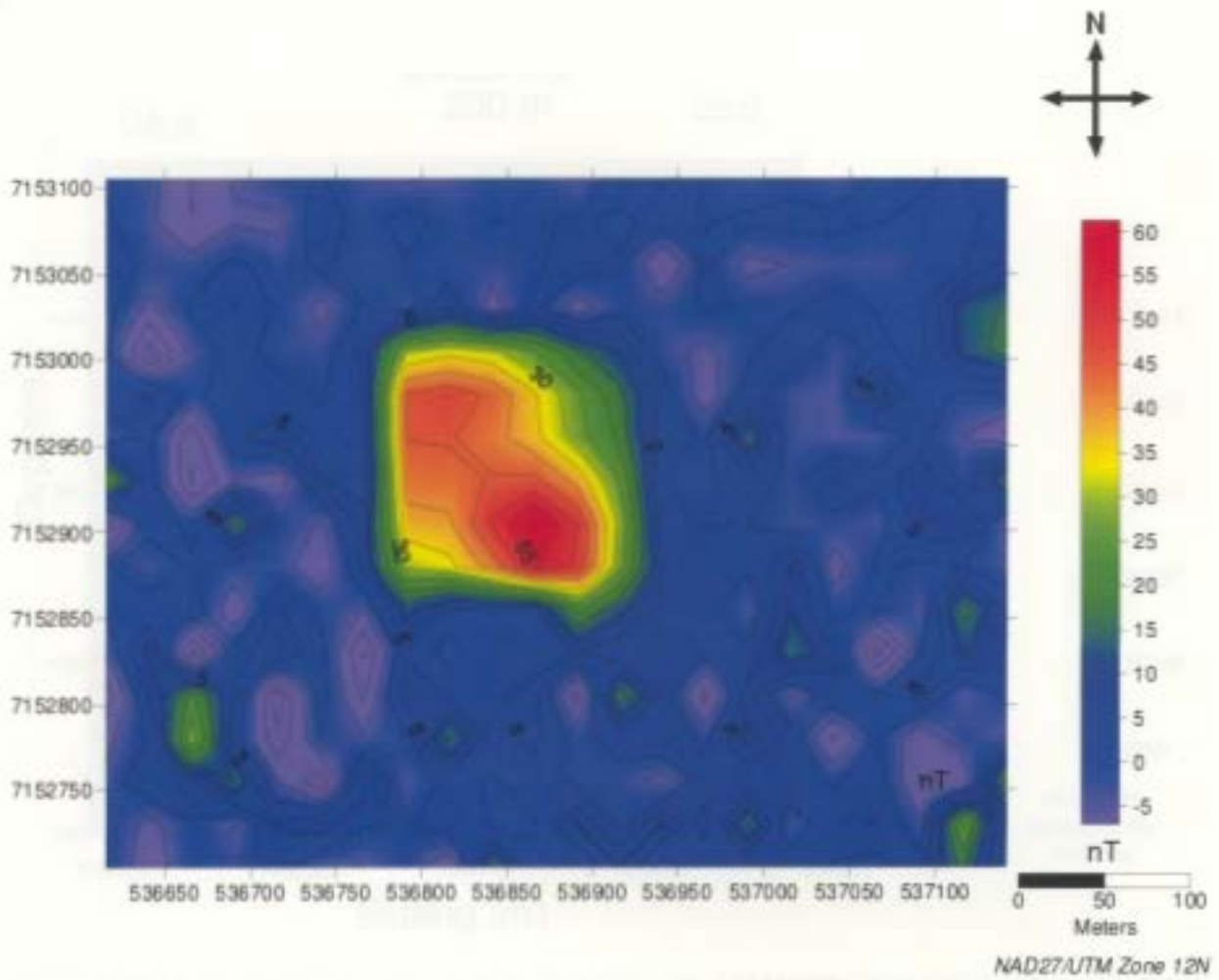


Figure 5.43: The predicted total magnetic field dataset of the *default mode inversion*.

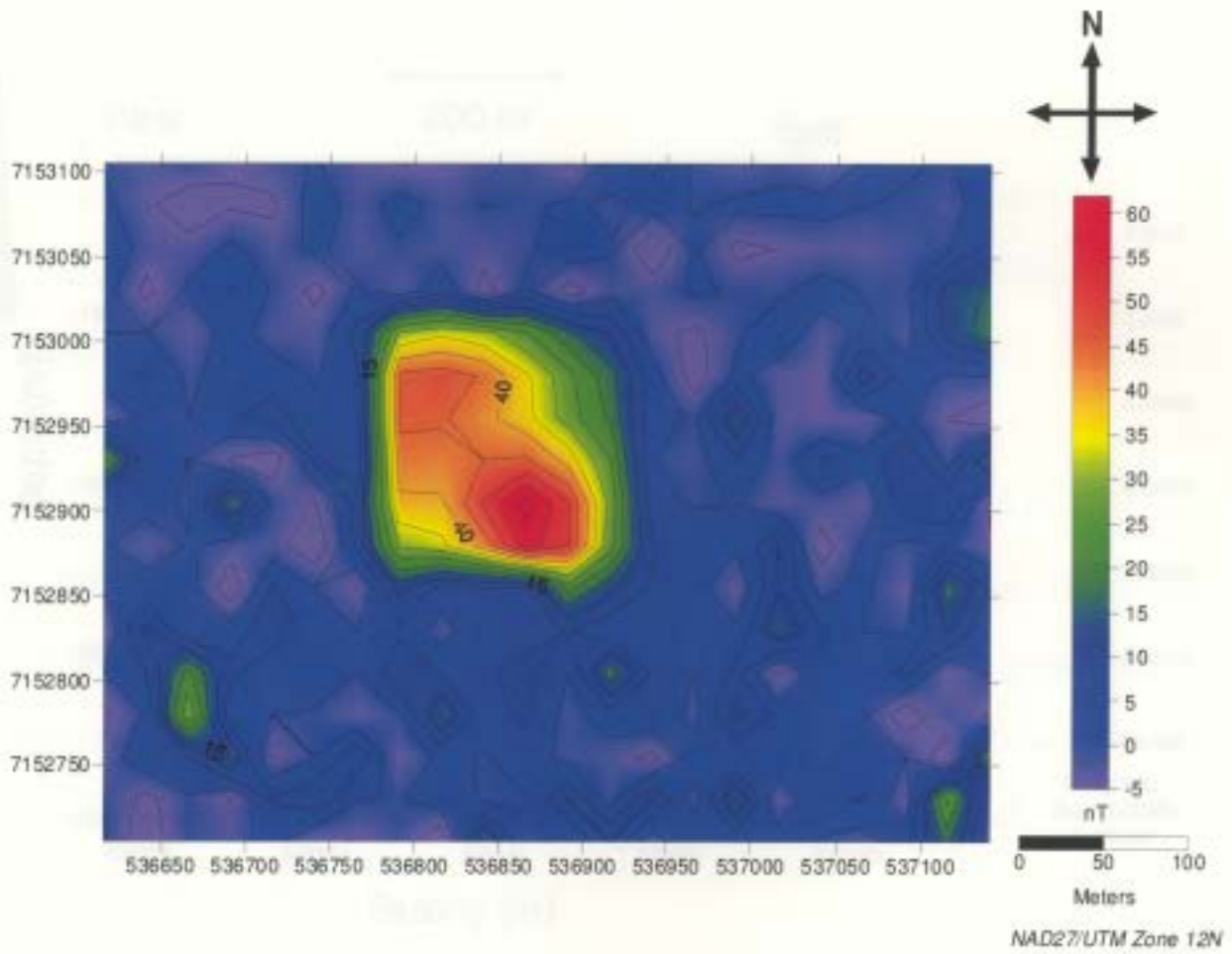


Figure 5.45: The predicted data resulting from the *model mode* magnetic inversion.

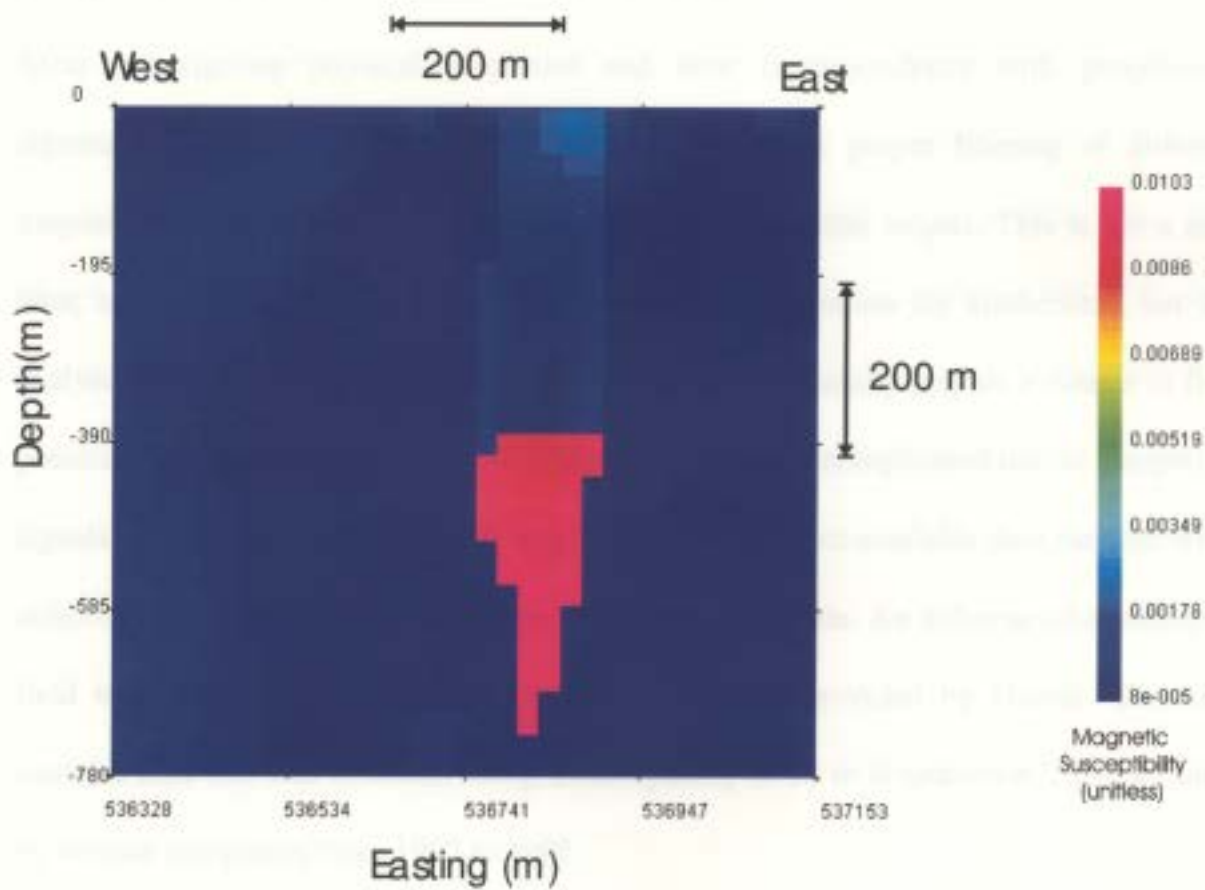


Figure 5.46: A depth slice running west to east across line 7152900N of the magnetic susceptibility model produced by the *model mode* inversion.

5.1 Magnetic Susceptibility Investigation

The primary goal of this investigation is to determine the magnetic susceptibility of the subsurface. This is achieved by measuring the magnetic field strength and direction at various depths and locations. The data is then processed to produce a magnetic susceptibility map. This map is used to identify areas of high magnetic susceptibility, which are likely to contain iron. The results of this investigation are presented in the following sections.

Chapter 6: Exploration for Kimberlite Pipes

After investigating physical properties and their correspondence with geophysical signatures, it is felt that there is great potential in the proper filtering of airborne magnetic, resistivity and gravity surveys to isolate kimberlite targets. This is not a new idea; airborne surveys are extensively used in the exploration for kimberlites, but the analyses of these results are encumbered by having to manually inspect a dataset to find potential targets. Detection of kimberlite pipes is at times complicated due to competing signals from random and diverse geological features. Due to available data the following airborne investigation will focus on total magnetic field data. An airborne total magnetic field map compiled by Aurora Geosciences Ltd was provided by Diavik. The map contains data that was collected along a line spacing of 50 m at unknown flight altitudes by various companies from 1992 to 1997.

In the Diavik area, diabase dykes have large positive magnetic signatures making pipes located close to these dykes difficult to detect. There is also the issue of remanent magnetization obscuring magnetic signatures as was discussed in Chapter 5.

6.1 Airborne Magnetic Investigation

The airborne total magnetic field map seen in Figure 6.1 was taken over the area of two known pipes: A154N and A154S. The locations of these pipes are marked on this map. There is a small positive anomaly present over the location of pipe A154N and a large positive anomaly over pipe A154S. The focus of this investigation will be on pipe

A154N. Since pipe A154S is in the same area, comments will be made about this pipe throughout. By reviewing the profile taken across pipe A154N (Figure 6.2), the magnetic signature of the pipe can be seen as a small peak between two large peaks associated with diabase dykes. The pipes small magnetic high is difficult to see in a large-scale map, suggesting that majority of the pipe's signature is hidden in the background field. It is proposed that by using directional filters and edge detection techniques, the signature over pipe A154N will be better defined and easier to detect in map view. The following investigation will test this hypothesis.

6.1.1 Directional Filters

A trend removal filter works by rejecting responses that are aligned with a specified trend direction. The trend direction can be given as a single angle or a range of angles. This filter was used to remove the effects of the dykes. There are three dykes seen in Figure 70. These dykes include two that are trending between 0° and 25° and one trending between 340° and 360° . Before running any edge detection filters, all three dykes were removed. The results are seen in map view in Figure 6.3, and in profile in Figure 6.4. Pipe A154N and Pipe A154S are still isolated in map view. By reviewing the profile over pipe A154N, the anomaly can be still present but the dyke responses have been largely attenuated. This dataset will be used during the investigation into edge detection techniques.

6.1.2 Edge Detection Techniques

The maximum horizontal gradient can be used to highlight the edges of an anomaly (Telford et al. 1990). It is equal to the sum of the squares of the x and y field derivatives (Eqn.1). As generalized by Miller and Singh (1994), the horizontal gradient peaks over the edges of a source body and is zero over the top of the source body.

The horizontal gradient approach uses the following equation:

$$\frac{df}{dh} = \left[\left(\frac{df}{dx} \right)^2 + \left(\frac{df}{dy} \right)^2 \right]^{1/2} \quad (13)$$

Where: $\frac{df}{dh}$ = magnitude horizontal gradient

$\frac{df}{dx}$ and $\frac{df}{dy}$ = gradients in the x and y directions respectively.

The analytical signal approach is similar to the horizontal gradient approach, except that it includes the vertical derivative (Roest et al 1992) (Eqn. 14):

$$|A(x, y)| = \left[\left(\frac{df}{dx} \right)^2 + \left(\frac{df}{dy} \right)^2 + \left(\frac{df}{dz} \right)^2 \right]^{1/2} \quad (14)$$

Where: $|A(x, y)|$ = the absolute value of the analytical signal

$\frac{df}{dx}$, $\frac{df}{dy}$, and $\frac{df}{dz}$ = represents gradients in the x, y, and z directions respectively

The first vertical derivative is positive over the top of the center of a body, is zero over the edge of a body and is negative outside of a vertical body (Miller and Singh 1994). By introducing the vertical (z) derivative the analytical signal reveals maximums directly overtop of the body in addition to the edges of the body (Roest et al. 1992). In combination with the horizontal derivative, the analytical signal technique will transform a circular anomaly into a sharper high making it easier to identify. As kimberlite anomalies are generally circular in shape, this technique should be advantages for their detection.

6.1.3 Discussion and Conclusions

The results of horizontal gradient and analytical signal filtering can be seen in Figures 6.5 and 6.6 respectively. The edges of kimberlite pipe A154N are located along 7152925N at 536850E and 536950E. The profiles for each technique are seen in Figure 6.7, with the pipe edges marked along the profile.

Both the horizontal gradient and analytical signal techniques aid in the isolation of kimberlite pipe anomalies. The analytical signal technique highlights the signature of pipe A154N more clearly than the horizontal gradient method. By design, the horizontal gradient only detects the edges of an anomaly. By reviewing the profile it can be seen that the edges were in fact detected, however, this did not make the anomaly easy to isolate in map view. In contrast, the analytical signal is designed to detect the edges and

the center of the source body. By reviewing its profile it can be seen that the edges and center were indeed detected. Comparing the profiles and map views of both techniques it appears that the advantage of analytical signal's detection of the center of the source body makes it easier to isolated pipe A154N. Pipe A154S was also isolated during this process, however, this pipe seems to respond to both the analytical signal and the horizontal gradient techniques. By reviewing the north-west area of Figure 6.5 and 6.6, there are anomalies present that are the correct size and shape to be undiscovered kimberlite pipes, however, it cannot be ruled out that these techniques are causing false anomalies. These techniques appear to work for both pipes A154N and A154S.

6.2 Other Kimberlite Detection Techniques

The future of kimberlite exploration seems to be headed in the direction of using pattern recognition techniques on survey data. A pattern recognition algorithm can be utilized to automatically pick out kimberlite anomalies from a dataset. One such technique was developed by Keating and Sailhac (2004). Their technique uses pattern recognition; patterns based on typical theoretical anomalies which are then swept through a grid in search of an anomaly defined by a specific pattern. Their implementation is restricted and considers generalized models based on vertical cylindrical pipes. Not all kimberlite pipes can be defined as vertical cylindrical bodies and therefore neither can their signatures. It is proposed that the patterns should be defined by the shape and size of anomalies resulting from forward models constrained by accurate physical property data and geometries. For example the magnetic forward model of pipe A154N (Figure 5.5,

Chapter 5). This anomaly has its own specific shape, size, and signature, in theory it can be used to define a pattern that will locate pipe A154N in a dataset and pipes with similar signatures. Using known pipe anomalies like this one, not theoretical anomalies, should provide a greater degree of accuracy to this technique.

An extensive study into this technique was beyond the time available for this thesis. It does however present an interesting case that could make use of the physical property data that was collected throughout this project, not only for pipe A154N but also for the other pipes on Diavik property.

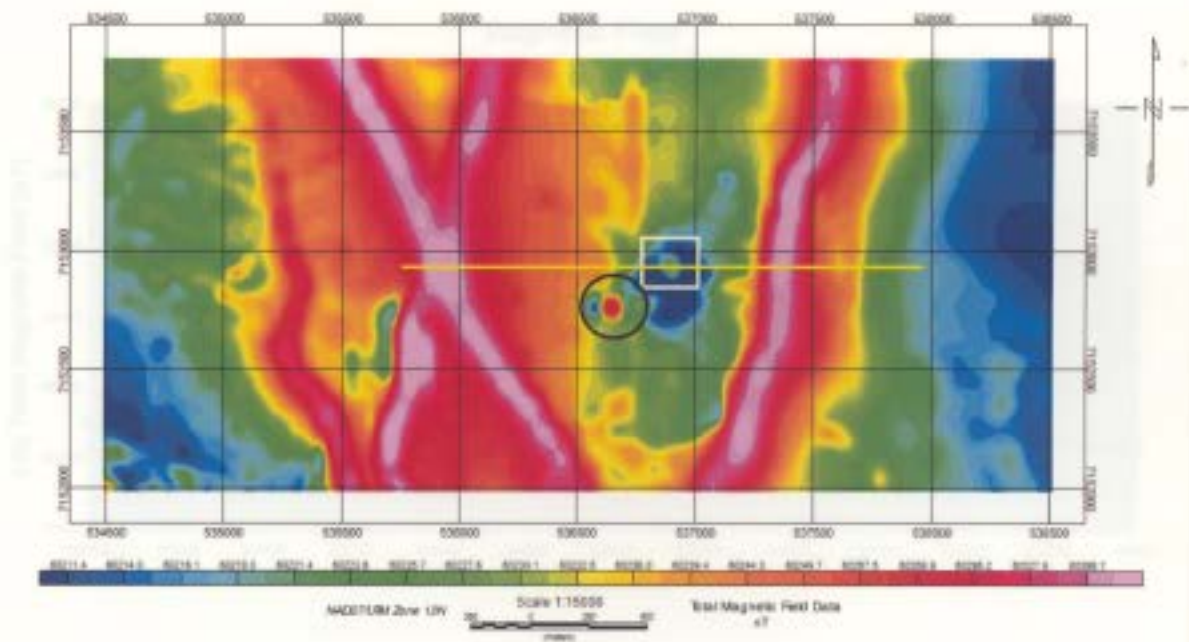


Figure 6.1: Airborne total magnetic field map with the location of A154N marked by a white box and pipe A154S marked with a black circle. The yellow locates profile line 7152925N that is seen in Figure 6.2. The elongated magnetic highs represent diabase dykes, which are believed to be swamping the signature of pipe A154N.

Magnetic Field

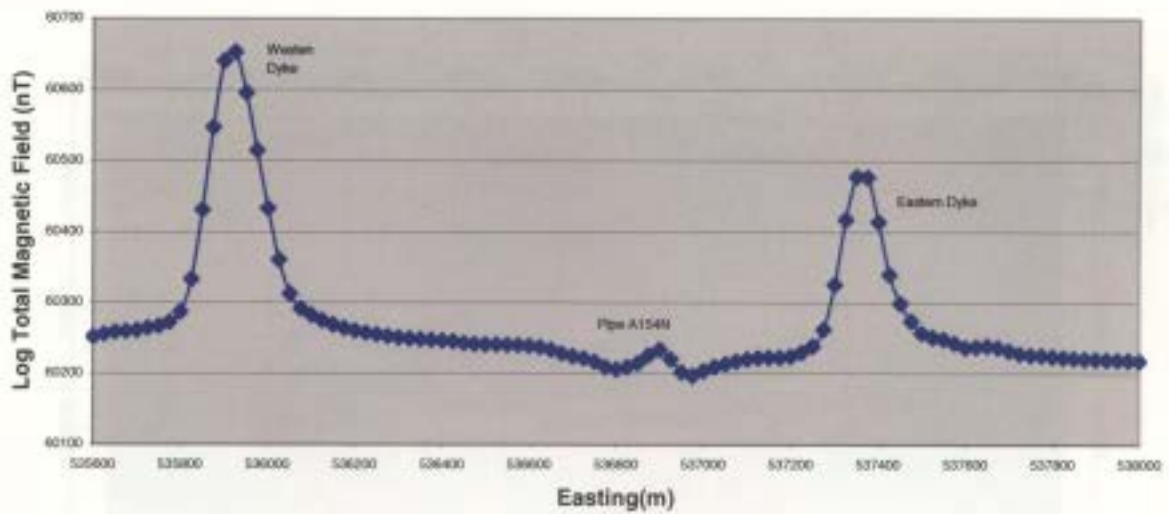


Figure 6.2: Profile of the resulting total magnetic field across pipe A154N along 7152925N. Note the location of the two dykes and pipe A154N.

Figure 6.2: The resulting profile after the total magnetic field of the profile from 7152925N was recorded along the line and the resulting magnetic field profile is shown. The profile shows the location of the two dykes and pipe A154N. The profile is shown along 7152925N and the resulting profile is shown in Figure 6.2.

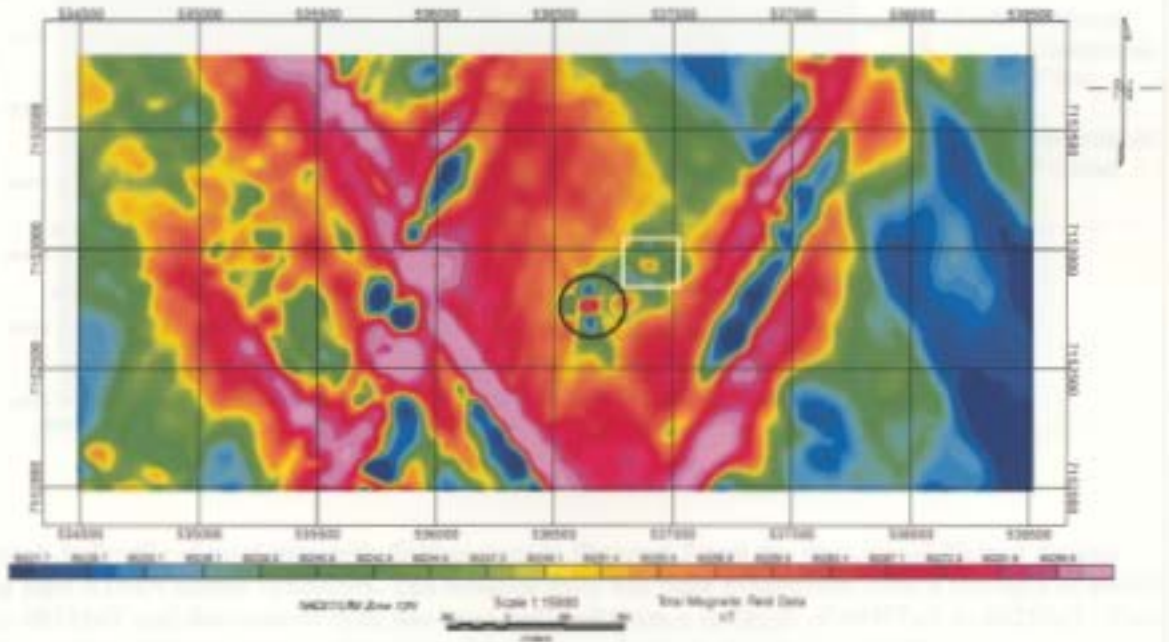


Figure 6.3: The resulting dataset after the trend removal of the dykes. Pipes A154N and A154S are marked as a white box and black circle respectively. Both pipe signatures are visible. It seems that the anomaly for pipeA154S has been reduced but the anomaly for pipe A154N is easier to see. A profile was taken along 7152925N of this dataset and can be seen in Figure 6.4.

Directional Filtered Total Magnetic Field Data

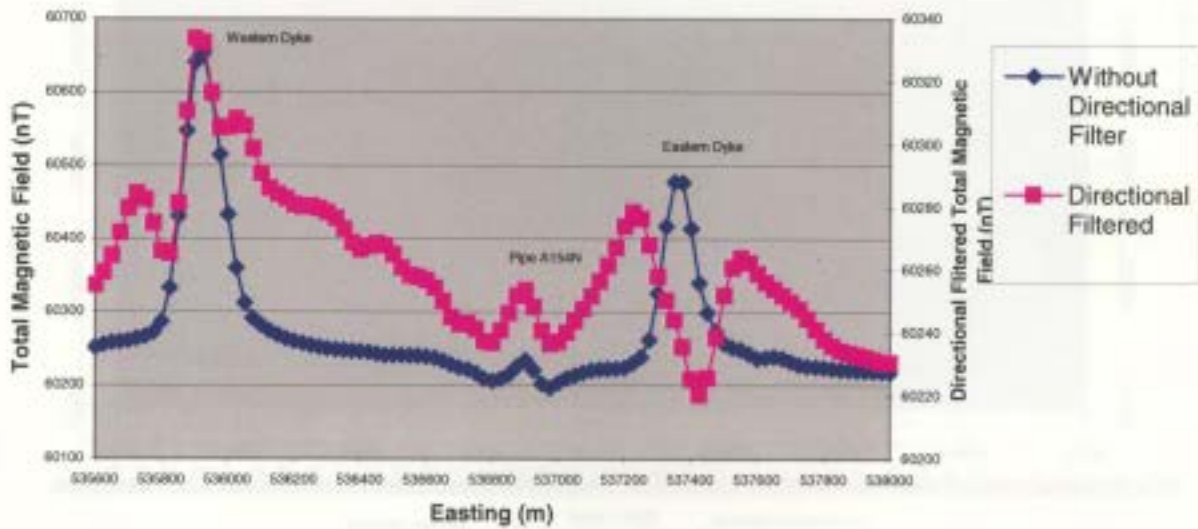


Figure 6.4: Profile of total magnetic field as seen in Figure 6.3 and the directional filtered dataset along pipe A154N across 7152925N. The western dyke has been attenuated from a strength of 60652 nT to 60333nT and the eastern dyke has been reduced from a strength of 60477nT to 60255nT. Due to the removal of the western and eastern dykes it is easier to isolated pipe A154N.

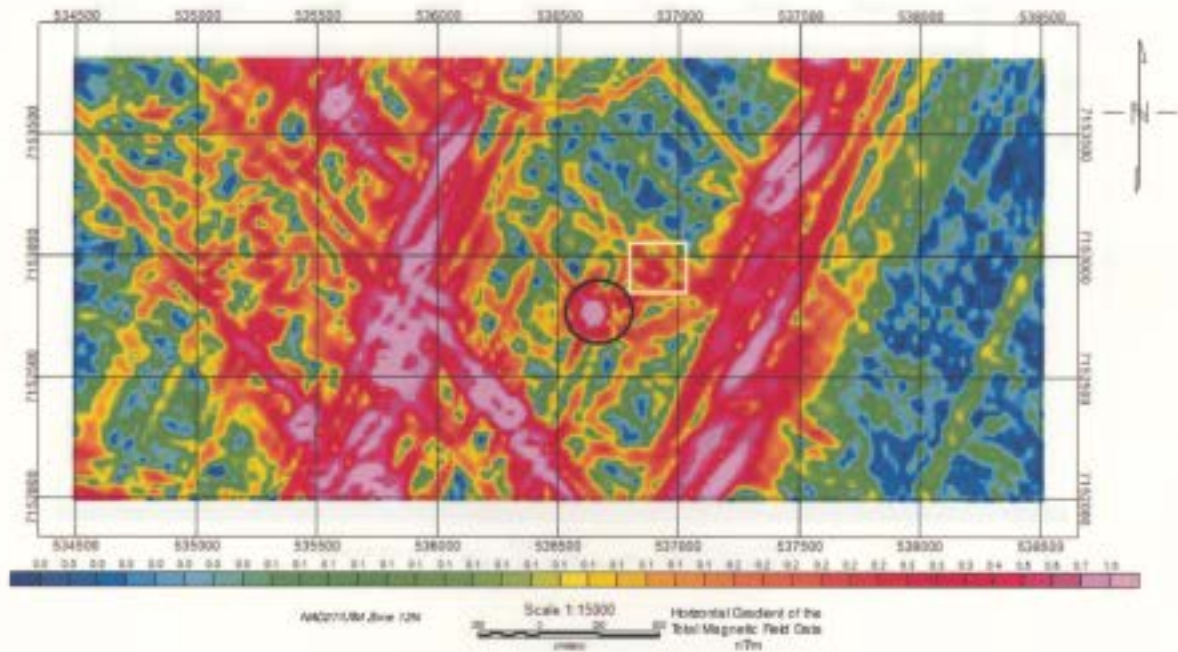


Figure 6.5: The results of applying horizontal gradient over the area. The location of pipe A154N and pipe A154S are marked with a white box and a black circle respectively. The horizontal gradient method has isolated pipe A154N and has clearly define pipe A154S.

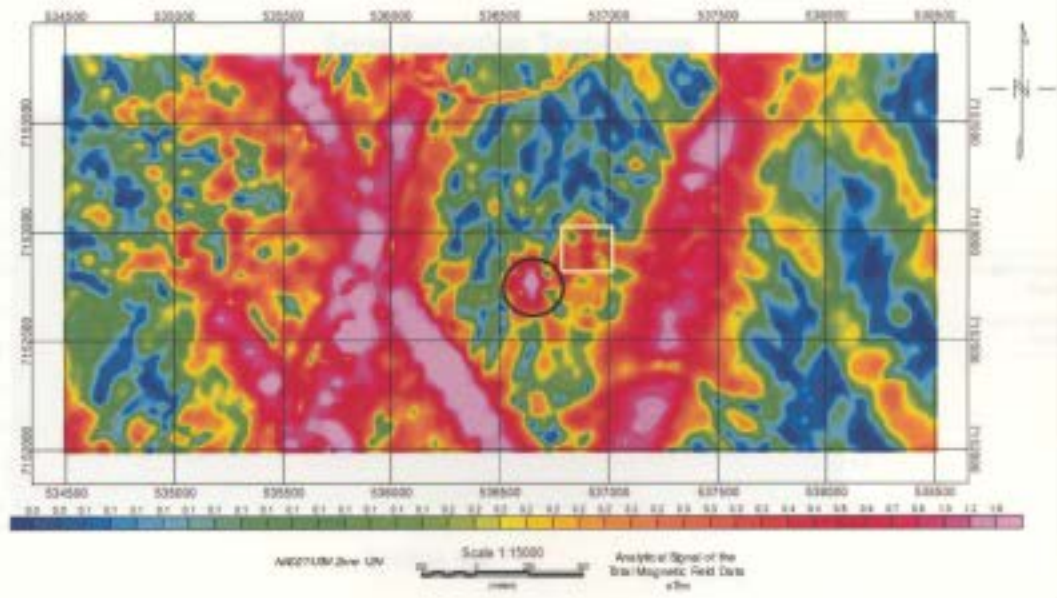


Figure 6.6: The results of applying analytical signal over the area. The location of pipe A154N is marked with a white box while the location of pipe A154S is marked with a black circle. The location of pipe A154N has been isolated while pipe A154S is clearly isolated.

Edge Detection Techniques

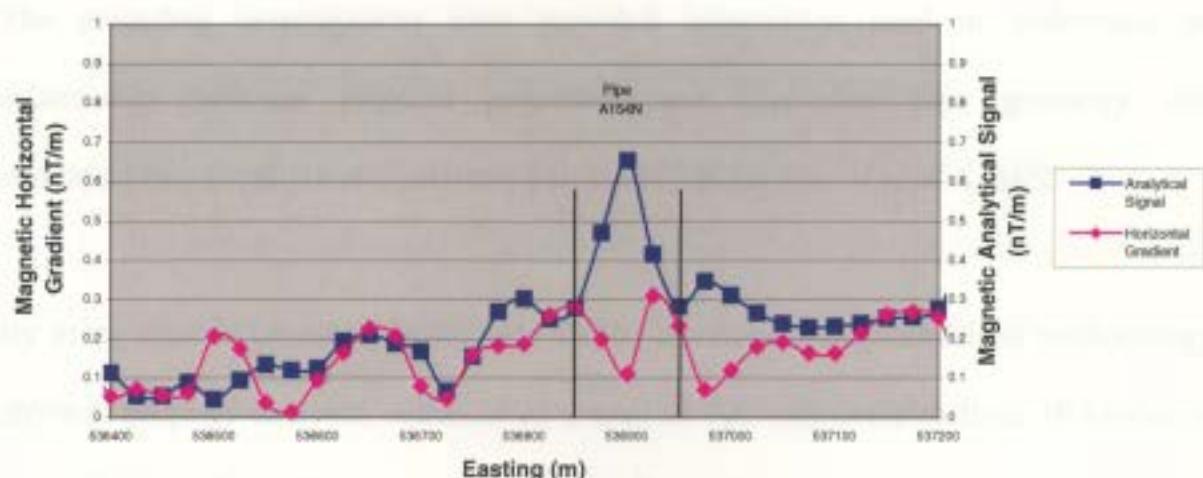


Figure 6.7: Profile of the resulting magnetic horizontal gradient and analytical signal filters across pipe A154N along 7152925N. Note the x-axis scale has been reduced in order to see the effects over pipe A154N. The horizontal gradient (in pink) has maximum values over the edges of pipe A154N and drops down over the top of the anomaly whereas; the analytical signal (in blue) shows maximum values over the top of the pipe.

Chapter 7: Conclusions

The preceding investigations have provided information used to understand the relationship between physical properties and kimberlite pipe geometry with corresponding geophysical signatures, particularly in the case of pipe A154N.

By using reliable laboratory equipment and by developing a systematized methodology, physical property data was collected on a total of 400 rock samples from 16 kimberlite pipes. Correct physical property from the Diavik area was essential to the accuracy of this investigation. It is strongly recommended that physical property information be collected from the area of interest as opposed to using values from a standardized table.

Statistical analysis proved that each physical property measurement was repeatable. The physical property data collected was split into two categories: data from pipe A154N and data from the remaining 15 pipes. A comparison was performed between these two categories to show that pipe A154N has physical properties which are representative of the Diavik area. It specifically showed that the average kimberlite properties of pipe A154N are similar to those properties for the other 15-kimberlite pipes in the area, with one exception being the density of the root zone. However, as seen in the forward modeling results, the majority of the gravitational response for pipe A154N is generated by the crater zone, therefore, this difference in root density is not an issue when dealing with pipes with deep crater/root zone interfaces. It was also found that the host rock properties were quite variable throughout the area.

The physical property values of pipe A154N from this study were compared to previous studies performed on kimberlite pipes from various locations throughout Canada, (Mwenifumbo et al 1996; Katsube and Kjargaard 1996). There are some differences between the previous collected data and the data collected in thesis for pipe A154N. Showing once again the importance of collecting data for the area that is being study. These differences could be caused by the differences in kimberlite magma from different kimberlite fields.

A Spearman rank test was used to investigate the dependence of each physical property with density and depth. Both tests were performed on two categories: pipe A154N data and data from the other 15 pipes. It was found that the rank test results for pipe A154N generally had higher levels of confidence associated with them and were therefore used as the representative correlation values. The results of this test conclude that there is no strong monotonic relationship between any physical property with depth or density. There were, however, some medium correlations found. These include positive correlation between density and magnetic susceptibility for all rock types, depth and remanent magnetization for host rock and root zone, depth and magnetic susceptibility for all rock types and depth and resistivity for both the host rock and crater zone. These results indicate that the respective properties have a small dependence upon each other.

The physical property values measured during this thesis, along with a constrained pipe model of A154N provided by Diavik, allowed for the construction of realistic subsurface

models. From these models, gravity and magnetic forward models were generated. This investigation involved running forward models over the two kimberlite zones and comparing those results to the full pipe model. One of the major outcomes was the conclusion that the largest contributor to the magnetic and gravity responses in pipe A154N comes from the kimberlite crater zone, not the root zone. When exploring for kimberlite pipes with similar structure to pipe A154N the focus should be on the crater zone. Forward models can also be used to aid in kimberlite detection techniques such as pattern recognition. These forward modeling signatures for pipe A154N compared well with residual observed data.

Residual data, along with physical property models, were also used to constrain gravity and magnetic inversions for pipe A154N. Two modes of inversion were used. These are a *default mode* and *model mode*. The *default mode* used only default setting whereas the *model mode* inversion used defined depth weighting parameters and the physical property models. It was concluded that constrained inversions performed much better than unconstrained inversions. There are, however, limitations to the forward models and inversions of pipe A154N. These include nonuniqueness, and in the case of magnetics data inversion, a lack of remanent magnetic information. Remanent magnetization within the kimberlite zones is often of the same order of magnitude, or greater than induced magnetization. In subsequent inversions of this data, a model that takes remanence into account should provide a more accurate inversion. It is unfortunate that the core samples

measured where not orientated and therefore the direction of remanent magnetism could not be measured.

The information gained by forward modeling and inversions was applied to airborne data. Given the circular shape of the kimberlite magnetic signature of pipe A154N, it was decided that edge detecting techniques would be used isolated pipe signatures. These include horizontal gradient and analytical signal techniques. However, due to the high background fields caused by local diabase dykes, directional filters were first applied which was mostly successful in attenuating the dykes. The result of both edge detecting techniques work well at isolating a pipe signature however, it was felt that false anomalies were also generated in the area. The process of isolating a kimberlite signature depends on the nature of the signal in the region; there seems to be no simple and widespread solution. Another method that could be used to find kimberlite pipes in a large-scale magnetic map is pattern recognition. Signature patterns, like those generated using forward models in this thesis, can be used to sweep through a dataset looking for this specific signature. This method was suggested by Keating and Sailhac (2004), however, their method used theoretical anomalies not known pipe anomalies.

Once a potential pipe target has been isolated, the area should be investigated with ground surveys (total magnetic field, HLEM, gravity, etc.), which help pinpoint the potential pipe in order to locate a drilling program. Since the physical properties of the pipes in the Diavik area have been found during this thesis, inversions of the potential

target can also help define potential drill locations. By using only field data, the *default mode* inversions will only generate a fuzzy blob close to the surface. Using *model mode* depth weighting parameters defined during this thesis and the magnetic susceptibility and density models for pipe A154N a better inverted subsurface was created and consequently better constraints for any drill programs. It is noted that the geometry of pipe A154N may or may not be similar to any given potential target pipe, however, it will give the inversion a good starting point. After the first inversion, a better idea of pipe geometry will be generated and the model can be changed to fit a new pipe's geometry. For example the crater zone root zone interface may be shallower, and the pipe diameter may be larger.

By using the techniques outlined in this thesis, more information was gained about pipe A154N. What is even more, these techniques and physical property values can be applied to aid in the exploration of unknown kimberlites in the Diavik area.

References:

Armstrong, J.P. and Kjarsgaard, B.A. 2003. Geology setting of kimberlite in the Archean slave province, VIIIth International Kimberlite Conference, Slave Province and Northern Alberta Field Trip Guidebook, : 31-38.

Bleeker, W. 2002. Archean tectonics; a review, with illustrations from the slave craton, The Early Earth: Physical, Chemical and Geological Development., **Geological Society, London**: 151-181.

Bleeker, W., Davis, W.J., Ketchum, J.W., Sircombe, K., and Stern, R.A. 2001. Tectonic evolution of the slave craton, Canada, AGSO- Geoscience Australia, **International Archaean Symposium**: 288-290.

Bryan, D. and Bonner, R. 2003. The Diavik diamond mine, Lac de Gras, Northwest Territories, Canada, VIIIth International Kimberlite Conference, Slave Province and Northern Alberta Field Trip Guidebook, : 61-65.

Butler, R.F. 1992. Paleomagnetism. Blackwell Scientific Publications, Ontario, Canada.

Cox, R. and Barnes, S.J. 2004. Laser-ablation ICP-MS analysis of mantle garnets: Single-mineral thermometry and geospeedometry applied to diamond exploration [online]. Available from www.divex.ca/projects/sc17_fr.html 2007]

Davis, W.J., Bleeker, W., MacLachlan, K., Jones, A.G., and Snyder, D. 2001. The late tectonic evolution of the slave craton and formation of its tectosphere, AGSO- Geoscience Australia, **International Archaean Symposium**: 300-302.

Davis, J. 2002. Statistics and data analysis in geology. John Wiley & Sons, New York.

Devore, J.L. 2004. Probability and statistics for engineering and the sciences. Thomson Books/Cole, Canada.

Diavik. 2007. Available from www.diavik.com 2006]

Earth Decisions. 2006. Gocad.

Exploranium. 1997. User's guide: KT-9 Kappameter rev.1. GEO F/X, Mississauga, Ontario.

Farquharson, C. 2007. Personal communication.

Farquharson, C. 2006. Constructing piecewise-constant models in multi-dimensional minimum-structure inversions, 76th Annual Meeting of the Society of Exploration Geophysicists, New Orleans, Louisiana,

Field, M. and Scott-Smith, B.H. 1998. Textural and genetic classification schemes of kimberlite: A new perspective. Extended Abstracts of the 7th International Kimberlite Conference, Cape Town, South Africa, : 214-216.

Geological Survey of Canada. 2007. Geomagnetism [online]. Available from http://www.geolab.nrcan.gc.ca/geomag/apps/mdcal_e.php.

Graham, I., Burgess, J.L., Bryan, D., Ravenscroft, P.J., Thomas, E., Doyle, B.J., Hopkins, R., and Armstrong, K.A. 1999. Exploration history and geology of the Diavik kimberlites, Lac de Gras, Northwest Territories, Canada, Seventh International Kimberlite Congerence, **Vol 1**: 262-279.

Griffin, W.L., Doyle, B.J., Ryan, C.G., Pearson, N.J., O'Reilly, S.Y., Davis, R., Kivi, K., Achterbergh, E.V., and Ntatpov, L.M. 1999. Layered mantle lithosphere in the Lac de Gras area, slave craton: Composition, structure and origin, *Journal of Petrology*, **Vol 40**: 705-727.

Hays, W.L. and Winkler, R.L. 1970. Statistics probability, inference, and decision. Holt, Rinehart and Winston, INC., New York.

Katsube, T.R. and Kjarsgaard, B.A. 1996. Physical characteristics of Canadian kimberlites, Searching for Diamonds in Canada, Geological Survey of Canada, **Open File 3228**: 241-242.

Katsube, T.R. and Scromeda, N. 1994. Physical properties of Canadian kimberlites, Somerset Island, Northwest Territories, and Saskatchewan, Current Research, Part B Geological Suvery of Canada, : 35-42.

Katsube, T.R., Scromeda, N., Bernius, G., and Kjarsgaard, B.A. 1992. Laboratory physical property measurements on kimberlites, Current Research, Part E Geological Survey of Canada, **Paper 92-1E**: 357-364.

Kearey, P., Brooks, M., and Hill, I. 2003. An introduction to geophysical exploration. Blackwell Publishing, United Kingdom.

Keating, P. and Sailhac, P. 2004. Use of the analytical signal to identify magnetic anomalies due to kimberlite pipes, *Geophysics*, **Vol 69**: 180-190.

King, J. and Helmstaedt, H. 1997. The slave province, Northwest Territories, Canada, Oxford Monographs on Geology and Geophysics, **Vol 35**: 459-479.

King, J.E., Davis, W.J., and Relf, C. 1992. Late Archean tectono-magnetic evolution of the central slave province, northwest territories, Canadian Journal of Earth Sciences, **Vol 29**: 2156-2170.

Kjarsgaard, B.A. 1996. Kimberlites, Searching for Diamonds in Canada, Geological Survey of Canada, **Open File 3228**: 29-37.

Kjarsgaard, B.A. 1996. Slave province kimberlites, N.W.T, Searching for Diamonds in Canada, Geological Survey of Canada, **Open File 3228**: 55-60.

Li, Y. and Oldenburg, D.W. 1998. 3-D inversion of gravity data, Geophysics, **Vol 63**: 109 - 119.

Li, Y. and Oldenburg, D.W. 1998^b. Separation of regional magnetic field data, Geophysics, **Vol 63**: 431-439.

Li, Y. and Oldenburg, D.W. 1996. 3D inversion of magnetic data, Geophysics, **Vol 61**: 394-408.

Lockhart, G., Grutter, H., and Carlson, J. 2004. Temporal, geomagnetic and related attributes of kimberlite magmatism at Ekati, Northwest Territories, Canada, Lithos, **Vol 77**: 665-682.

Lorenz, V. and Kurszlaukis, S. 2003. Kimberlite pipes: Growth models and resulting implications for diamond exploration, VIIIth International Kimberlite Conference, Long Abstract: 1-5.

May, P. Molecule of the month diamond [online]. Available from <http://www.chm.bris.ac.uk/motm/diamond/diamond.htm> 2006]

Miller, H.G. and Singh, V. 1994. Potential field tilt - a new concept for location of potential field sources, Journal of Applied Geophysics, **Vol 32**: 213-217.

Mwenifumbo, C.J., Hunter, J.A.M., and Killeen, P.G. 1996. Geophysical characteristics of Canadian kimberlites, Searching for Diamonds in Canada, Geological Survey of Canada, **Open File 3228**: 237-240.

Oldenburg, D.W., Li, Y., Farquharson, C., Kowalczyk, P., Aravanis, T., King, A., Zhang, P., and Watts, A. 1998. Applications of geophysical inversions in mineral exploration, The Leading Edge, : 461-465.

Parasnis, D.S. 1997. Principles of applied geophysics. Chapman & Hall, New York.

- Pidwirny, M. 2006. Introduction to the hydrosphere [online]. Available from <http://www.physicalgeography.net/fundamentals/8a.html> 2007]
- Power, M., Belcourt, G., and Rockel, E. 2004. Geophysical methods for kimberlite exploration in northern Canada, *The Leading Edge*, : 1124-1129.
- Schon, J.H. 1996. *Physical properties of rocks: Fundamentals and principles of petrophysics*. Pergamon,
- SPSS. 2006. *Statistics package for the social sciences graduate package 15.0*.
- Stubley, M. 1998. *Bedrock geology of the east island area, Lac de Gras*. Stubley Geoscience,
- Telford, W.M., Geldart, L.P., and Sheriff, R.E. 1990. *Applied geophysics*. Cambridge University Press, New York.
- Topping, J. 1969. *Errors of observation and their treatment*. Chapman and Hall Limited, London.
- UBC-GIF 2002 Developed under the consortium research project Joint/Cooperative Inversion of Geophysical and Geological Data, UBC-Geophysical Inversion Facility, Department of Earth and Ocean Sciences, University of British Columbia, Vancouver, British Columbia. MAG3D; A program library for forward modelling and inversion of magnetic data over 3D structures, version 3.1.
- UBC-GIF 2002 Developed under the consortium research project Joint/Cooperative Inversion of Geophysical and Geological Data, UBC-Geophysical Inversion Facility, Department of Earth and Ocean Sciences, University of British Columbia, Vancouver, British Columbia. GRAV3D; A program library for forward modelling and inversion of gravity data over 3D structures, version 2.0.

Appendix A
Raw Data

Sample Number	Rock Type	Density (g/cm³)	Remanent Magnetization (A/m)	Magnetic Susceptibility (unitless)	Resistivity (ohm-m)
1.00	Host Rock	2.60	0.00161	-0.00040	N/A
2.00	Host Rock	2.70	0.00061	0.00005	N/A
3.00	Host Rock	2.63	0.00031	-0.00009	N/A
4.00	Host Rock	2.63	N/A	-0.00008	N/A
5.00	Host Rock	N/A	N/A	0.00025	N/A
6.00	Host Rock	2.58	0.00074	0.00002	N/A
7.00	Host Rock	2.67	0.00128	-0.00032	N/A
8.00	Host Rock	2.73	N/A	N/A	N/A
9.00	Host Rock	2.74	0.02588	N/A	N/A
10.00	Host Rock	2.69	0.00120	N/A	N/A
11.00	Host Rock	2.62	0.00083	-0.00026	N/A
12.00	Host Rock	2.66	N/A	0.00008	N/A
13.00	Host Rock	2.64	0.00050	N/A	N/A
14.00	Host Rock	2.63	0.00081	-0.00028	N/A
15.00	Host Rock	2.66	0.00107	0.00011	N/A
16.00	Host Rock	2.64	0.00063	N/A	N/A
17.00	Host Rock	2.69	0.00054	N/A	N/A
18.00	Host Rock	2.66	0.00167	-0.00006	N/A
19.00	Host Rock	2.65	0.00035	-0.00036	N/A
20.00	Host Rock	2.70	0.00286	0.00022	N/A
21.00	Host Rock	2.62	0.00068	-0.00006	N/A
22.00	Host Rock	2.58	0.00078	-0.00021	N/A
23.00	Host Rock	2.73	0.00104	0.00021	N/A
24.00	Host Rock	2.60	0.00098	-0.00009	N/A
25.00	Host Rock	2.78	0.00106	0.00026	N/A
26.00	Host Rock	2.71	0.00116	-0.00001	N/A
27.00	Host Rock	2.72	0.00010	0.00017	N/A
28.00	Host Rock	2.66	0.00056	N/A	N/A
29.00	Host Rock	2.61	0.00147	-0.00006	N/A
30.00	Host Rock	2.64	0.00140	0.00005	N/A
31.00	Host Rock	2.66	0.00403	-0.00013	N/A
32.00	Host Rock	N/A	N/A	N/A	N/A
33.00	Host Rock	N/A	N/A	-0.00010	N/A
34.00	Host Rock	2.70	0.00224	0.00017	N/A
35.00	Host Rock	2.66	0.00080	-0.00002	N/A
36.00	Host Rock	2.68	0.00090	0.00000	N/A
37.00	Host Rock	N/A	N/A	-0.00014	N/A
38.00	Host Rock	2.61	0.00088	-0.00008	N/A
39.00	Host Rock	2.62	0.00218	-0.00015	N/A
40.00	Host Rock	2.68	0.00216	-0.00011	N/A
41.00	Host Rock	2.67	0.00106	-0.00037	N/A
42.00	Host Rock	2.73	0.00066	0.00040	N/A
43.00	Host Rock	2.62	0.00092	0.00001	N/A
44.00	Host Rock	N/A	N/A	-0.00016	N/A
45.00	Host Rock	2.76	0.00277	0.00034	N/A
46.00	Host Rock	2.66	0.00026	0.00001	N/A
47.00	Host Rock	2.66	N/A	0.00002	N/A

Sample Number	Rock Type	Density (g/cm ³)	Remanent Magnetization (A/m)	Magnetic Susceptibility (unitless)	Resistivity (ohm-m)
48.00	Host Rock	2.72	N/A	0.00023	N/A
49.00	Host Rock	N/A	N/A	0.00055	N/A
50.00	Host Rock	2.74	0.03760	0.00023	N/A
51.00	Host Rock	N/A	N/A	0.00050	9,075.12
52.00	Host Rock	2.62	0.00080	-0.00009	N/A
53.00	Host Rock	2.66	0.00572	0.00008	11,572.21
54.00	Host Rock	2.60	0.00089	0.00009	N/A
55.00	Host Rock	2.61	0.00030	0.00013	17,755.27
56.00	Host Rock	2.68	0.00114	0.00002	N/A
57.00	Host Rock	2.69	0.00281	0.00009	4,096.56
58.00	Host Rock	2.65	0.00057	0.00007	3,877.47
59.00	Host Rock	2.67	0.01251	0.00020	11,734.34
60.00	Host Rock	N/A	N/A	0.00009	N/A
61.00	Host Rock	2.69	0.00138	0.00004	12,404.07
62.00	Host Rock	2.60	0.00317	-0.00003	19,898.40
63.00	Host Rock	2.69	0.00109	0.00010	N/A
64.00	Host Rock	2.65	N/A	0.00013	N/A
65.00	Root Zone	2.87	0.32427	0.01400	1,124.57
66.00	Root Zone	2.71	3.12209	0.00554	N/A
67.00	Root Zone	2.81	0.33051	N/A	N/A
68.00	Root Zone	2.86	0.60721	0.01780	731.25
69.00	Root Zone	2.82	3.37052	0.01310	534.27
70.00	Root Zone	N/A	0.89050	0.01580	N/A
71.00	Root Zone	2.85	0.57745	0.01330	232.74
72.00	Root Zone	2.72	2.21861	0.00726	N/A
73.00	Root Zone	2.73	0.83523	N/A	204.97
74.00	Crater Zone	2.58	0.29894	0.00078	N/A
75.00	Crater Zone	N/A	1.19820	0.00304	5,414.00
76.00	Host Rock	2.59	0.00290	0.00005	N/A
77.00	Host Rock	N/A	0.00297	0.00002	N/A
78.00	Host Rock	N/A	0.00086	-0.00001	N/A
79.00	Host Rock	2.60	0.00066	-0.00001	566.48
80.00	Crater Zone	2.71	0.78800	0.00286	N/A
81.00	Crater Zone	N/A	N/A	N/A	N/A
82.00	Crater Zone	2.64	N/A	0.00428	325.86
83.00	Crater Zone	N/A	0.57105	N/A	133.62
84.00	Root Zone	2.88	2.20339	0.00982	691.99
85.00	Root Zone	2.64	0.61901	0.00762	N/A
86.00	Root Zone	N/A	N/A	N/A	N/A
87.00	Crater Zone	2.64	0.60316	N/A	N/A
88.00	Root Zone	2.83	N/A	0.00932	N/A
89.00	Root Zone	2.95	N/A	0.00826	N/A
90.00	Root Zone	2.69	3.00343	0.00534	474.53
91.00	Crater Zone	N/A	0.84537	N/A	N/A
92.00	Root Zone	2.88	1.75293	0.00694	670.52
93.00	Crater Zone	N/A	N/A	0.00557	626.53
94.00	Crater Zone	2.41	0.28260	0.00056	N/A

Sample Number	Rock Type	Density (g/cm ³)	Remanent Magnetization (A/m)	Magnetic Susceptibility (unitless)	Resistivity (ohm-m)
95.00	Crater Zone	2.54	1.32973	0.00388	288.73
96.00	Crater Zone	2.46	1.88757	0.00211	N/A
97.00	Host Rock	2.63	0.03538	0.00003	608.22
98.00	Host Rock	2.73	0.06924	0.00035	1,358.74
99.00	Host Rock	N/A	N/A	0.00004	N/A
100.00	Host Rock	2.78	0.08148	0.00039	N/A
101.00	Host Rock	2.59	0.00119	-0.00011	4,084.51
102.00	Host Rock	N/A	N/A	0.00029	N/A
103.00	Host Rock	2.60	N/A	0.00000	465.83
104.00	Host Rock	2.56	N/A	-0.00002	508.75
105.00	Root Zone	N/A	0.74993	N/A	N/A
106.00	Root Zone	N/A	N/A	N/A	N/A
107.00	Host Rock	2.65	N/A	0.00013	1,503.52
108.00	Crater Zone	2.39	0.28805	0.00047	N/A
109.00	Crater Zone	N/A	N/A	0.00237	N/A
110.00	Crater Zone	2.38	0.19254	0.00050	N/A
111.00	Crater Zone	N/A	N/A	0.00077	N/A
112.00	Crater Zone	2.66	N/A	0.00294	N/A
113.00	Crater Zone	N/A	0.00148	0.00430	935.83
114.00	Crater Zone	N/A	N/A	0.00119	284.37
115.00	Crater Zone	2.51	0.09911	0.00122	1,882.33
116.00	Host Rock	N/A	N/A	0.00062	1,930.71
117.00	Host Rock	2.69	0.02384	0.00043	N/A
118.00	Host Rock	2.68	0.04102	0.00044	1,128.52
119.00	Host Rock	2.71	0.02889	0.00013	758.03
120.00	Host Rock	2.68	0.04080	0.00049	619.20
121.00	Host Rock	2.58	0.00152	0.00001	N/A
122.00	Host Rock	2.75	0.02771	0.00068	4,312.29
123.00	Host Rock	2.57	0.00167	0.00004	N/A
124.00	Host Rock	2.66	0.00125	0.00046	N/A
125.00	Host Rock	2.69	0.03024	-0.00002	662.68
126.00	Host Rock	2.82	0.05754	0.00059	3,541.87
127.00	Host Rock	2.83	N/A	0.00050	N/A
128.00	Host Rock	2.60	0.00114	N/A	471.53
129.00	Host Rock	2.75	0.03764	0.00040	1,078.17
130.00	Host Rock	2.67	0.02250	0.00028	2,303.99
131.00	Host Rock	2.61	0.00075	0.00004	1,142.16
132.00	Crater Zone	2.44	0.01483	0.00053	N/A
133.00	Host Rock	2.61	N/A	-0.00006	4,568.32
134.00	Host Rock	2.59	0.00328	-0.00005	N/A
135.00	Crater Zone	N/A	0.00107	0.00041	N/A
136.00	Crater Zone	2.54	0.00913	0.00034	N/A
137.00	Crater Zone	N/A	N/A	0.00033	N/A
138.00	Crater Zone	2.43	0.01267	0.00033	N/A
139.00	Crater Zone	N/A	N/A	0.00038	N/A
140.00	Crater Zone	2.40	0.00875	0.00043	N/A
141.00	Crater Zone	N/A	N/A	0.00048	N/A

Sample Number	Rock Type	Density (g/cm³)	Remanent Magnetization (A/m)	Magnetic Susceptibility (unitless)	Resistivity (ohm-m)
142.00	Crater Zone	N/A	N/A	0.00025	N/A
143.00	Crater Zone	N/A	N/A	0.00028	N/A
144.00	Crater Zone	N/A	N/A	N/A	N/A
145.00	Crater Zone	N/A	N/A	0.00032	N/A
146.00	Crater Zone	2.36	0.01786	0.00038	N/A
147.00	Host Rock	N/A	0.00299	0.00018	2,041.07
148.00	Crater Zone	N/A	N/A	0.00031	N/A
149.00	Crater Zone	2.52	0.45555	0.00096	N/A
150.00	Crater Zone	2.36	0.34919	0.00101	N/A
151.00	Crater Zone	2.49	0.27116	0.00080	1,136.70
152.00	Crater Zone	2.47	0.22075	0.00078	819.23
153.00	Crater Zone	2.39	0.45839	0.00127	N/A
154.00	Crater Zone	2.62	0.11421	0.00077	N/A
155.00	Host Rock	2.65	0.00019	-0.00001	1,571.01
156.00	Host Rock	2.63	0.00246	N/A	N/A
157.00	Crater Zone	2.47	0.03858	0.00066	N/A
158.00	Crater Zone	N/A	N/A	0.00038	N/A
159.00	Crater Zone	2.54	0.02370	0.00066	N/A
160.00	Crater Zone	2.54	0.03745	0.00053	370.63
161.00	Crater Zone	2.56	0.67995	0.00223	N/A
162.00	Crater Zone	2.52	0.90612	0.00227	1,860.08
163.00	Crater Zone	2.61	0.44455	0.00188	1,376.12
164.00	Crater Zone	2.48	0.13482	0.00060	N/A
165.00	Crater Zone	2.59	0.20584	0.00094	N/A
166.00	Crater Zone	2.49	0.22838	0.00095	N/A
167.00	Crater Zone	2.55	0.08354	0.00084	1,713.68
168.00	Crater Zone	2.42	0.74130	0.00235	894.88
169.00	Crater Zone	2.58	0.33951	0.00104	854.69
170.00	Crater Zone	2.53	0.52609	0.00221	762.92
171.00	Crater Zone	2.57	0.17098	0.00103	171.67
172.00	Host Rock	2.66	0.00136	0.00006	7,305.93
173.00	Host Rock	2.70	0.02480	0.00011	12,587.50
174.00	Host Rock	2.70	0.00121	-0.00002	4,332.28
175.00	Host Rock	2.73	0.06061	0.00030	N/A
176.00	Crater Zone	2.59	0.40860	0.00126	N/A
177.00	Crater Zone	2.48	0.63718	0.00188	1,113.46
180.00	Crater Zone	2.41	0.00393	0.00028	N/A
181.00	Crater Zone	2.47	0.62887	0.00207	N/A
182.00	Crater Zone	2.60	0.72547	0.00284	3,810.85
183.00	Crater Zone	2.54	0.44339	0.00280	2,286.90
184.00	Crater Zone	2.61	0.81257	N/A	2,974.04
185.00	Host Rock	2.67	0.00077	-0.00004	N/A
186.00	Host Rock	2.62	0.00055	-0.00001	14,131.90
187.00	Crater Zone	N/A	N/A	0.00031	N/A
188.00	Crater Zone	N/A	N/A	0.00047	N/A
189.00	Crater Zone	N/A	N/A	0.00026	N/A
190.00	Crater Zone	N/A	N/A	0.00046	N/A

Sample Number	Rock Type	Density (g/cm ³)	Remanent Magnetization (A/m)	Magnetic Susceptibility (unitless)	Resistivity (ohm-m)
191.00	Crater Zone	2.68	1.05915	0.00216	4,124.35
192.00	Crater Zone	2.67	1.62823	0.00290	3,368.33
193.00	Crater Zone	2.51	1.07055	0.00327	4,564.02
194.00	Crater Zone	2.58	0.08931	0.00563	N/A
195.00	Crater Zone	2.43	0.14837	0.00105	1,542.60
196.00	Crater Zone	2.62	0.03668	0.00041	6,534.78
197.00	Crater Zone	N/A	N/A	0.00041	N/A
200.00	Crater Zone	2.35	0.03373	0.00008	N/A
201.00	Crater Zone	N/A	N/A	N/A	N/A
202.00	Crater Zone	N/A	N/A	0.00000	N/A
203.00	Crater Zone	2.34	0.00778	0.00008	N/A
204.00	Root Zone	2.85	1.46940	0.00173	N/A
205.00	Root Zone	2.64	0.07517	0.00032	N/A
206.00	Host Rock	2.63	0.00133	-0.00004	N/A
207.00	Host Rock	2.73	0.00092	0.00011	N/A
208.00	Host Rock	2.58	0.00202	-0.00010	N/A
209.00	Host Rock	2.67	0.00162	0.00000	N/A
210.00	Host Rock	2.67	N/A	0.00006	N/A
211.00	Host Rock	2.75	N/A	N/A	N/A
212.00	Crater Zone	2.40	0.05689	0.00046	N/A
213.00	Crater Zone	2.15	0.01054	N/A	N/A
214.00	Crater Zone	2.54	0.06349	0.00036	N/A
215.00	Host Rock	N/A	N/A	0.00032	N/A
216.00	Host Rock	2.63	0.00065	0.00016	N/A
217.00	Host Rock	2.64	0.00085	-0.00001	N/A
218.00	Host Rock	2.65	0.00085	-0.00002	N/A
219.00	Host Rock	2.67	0.00044	-0.00004	N/A
220.00	Host Rock	2.74	0.00033	0.00023	N/A
221.00	Host Rock	2.64	0.00215	-0.00004	N/A
222.00	Crater Zone	2.81	N/A	N/A	N/A
224.00	Root Zone	N/A	N/A	N/A	N/A
225.00	Host Rock	2.68	N/A	0.00013	N/A
226.00	Host Rock	2.63	0.00170	-0.00004	N/A
227.00	Crater Zone	2.40	0.05499	0.00025	N/A
228.00	Crater Zone	2.52	0.05446	-0.00028	N/A
229.00	Crater Zone	2.27	0.03740	0.00030	N/A
230.00	Crater Zone	N/A	N/A	N/A	N/A
231.00	Crater Zone	2.64	N/A	0.00003	N/A
232.00	Crater Zone	N/A	N/A	N/A	N/A
233.00	Crater Zone	2.39	0.02829	0.00017	N/A
234.00	Crater Zone	N/A	N/A	N/A	N/A
235.00	Host Rock	2.64	0.00388	-0.00008	N/A
236.00	Host Rock	2.61	0.00069	-0.00008	N/A
237.00	Host Rock	2.57	0.00149	-0.00004	N/A
238.00	Root Zone	2.90	1.23297	0.00130	N/A
239.00	Crater Zone	2.37	0.07674	0.00030	N/A
240.00	Crater Zone	2.75	N/A	N/A	N/A

Sample Number	Rock Type	Density (g/cm³)	Remanent Magnetization (A/m)	Magnetic Susceptibility (unitless)	Resistivity (ohm-m)
241.00	Crater Zone	2.69	N/A	N/A	N/A
242.00	Host Rock	N/A	N/A	0.00047	N/A
243.00	Host Rock	2.64	0.00351	0.00001	N/A
244.00	Host Rock	N/A	N/A	N/A	N/A
245.00	Host Rock	2.60	0.00107	-0.00002	N/A
246.00	Crater Zone	N/A	N/A	0.00019	N/A
247.00	Host Rock	2.68	0.00138	-0.00004	N/A
248.00	Host Rock	2.62	0.00024	-0.00012	N/A
249.00	Host Rock	2.70	0.00194	N/A	9,834.01
250.00	Host Rock	2.63	0.00007	N/A	13,034.11
251.00	Host Rock	2.72	0.00007	0.00000	N/A
252.00	Host Rock	2.71	0.00199	N/A	10,457.16
253.00	Host Rock	N/A	N/A	-0.00007	N/A
254.00	Host Rock	2.77	0.00010	N/A	8,234.06
255.00	Crater Zone	N/A	N/A	0.00207	N/A
256.00	Crater Zone	N/A	N/A	0.00017	N/A
257.00	Host Rock	2.71	0.00016	N/A	10,315.90
258.00	Host Rock	2.62	0.00209	N/A	7,494.83
259.00	Host Rock	2.71	0.00022	N/A	N/A
260.00	Root Zone	2.55	0.01105	0.00049	N/A
261.00	Host Rock	N/A	0.00028	N/A	15,868.46
262.00	Host Rock	2.66	0.00006	0.00000	N/A
263.00	Host Rock	2.74	0.02254	0.00035	N/A
264.00	Host Rock	2.77	0.00021	0.00014	N/A
265.00	Host Rock	2.63	0.00016	-0.00001	N/A
266.00	Host Rock	2.79	0.00019	0.00015	N/A
267.00	Host Rock	2.71	0.00074	0.00000	N/A
268.00	Host Rock	N/A	N/A	N/A	N/A
269.00	Host Rock	2.64	0.00011	-0.00004	N/A
270.00	Host Rock	2.63	0.00037	-0.00002	N/A
271.00	Crater Zone	N/A	N/A	0.00021	N/A
272.00	Crater Zone	2.74	0.20369	N/A	N/A
272.50	Host Rock	2.64	0.00030	N/A	17,611.93
273.00	Crater Zone	N/A	N/A	0.00008	N/A
274.00	Crater Zone	2.56	0.00097	0.00050	603.88
275.00	Crater Zone	2.47	0.00045	0.00052	N/A
276.00	Crater Zone	2.40	0.00147	N/A	N/A
277.00	Crater Zone	N/A	N/A	0.00144	N/A
278.00	Crater Zone	2.39	0.00070	0.00052	N/A
279.00	Crater Zone	2.47	0.00100	0.00050	261.94
280.00	Crater Zone	2.58	0.00053	0.00053	N/A
281.00	Crater Zone	2.58	0.00012	N/A	N/A
282.00	Crater Zone	N/A	N/A	0.00055	N/A
283.00	Crater Zone	2.47	0.00140	0.00093	233.07
284.00	Host Rock	2.64	0.00010	0.00003	8,984.85
285.00	Host Rock	2.63	0.00010	0.00005	N/A
286.00	Host Rock	2.62	0.00031	0.00000	48,535.04

Sample Number	Rock Type	Density (g/cm³)	Remanent Magnetization (A/m)	Magnetic Susceptibility (unitless)	Resistivity (ohm-m)
287.00	Host Rock	2.62	0.00006	0.00000	18,586.88
288.00	Host Rock	2.72	0.00012	0.00025	N/A
289.00	Host Rock	2.65	0.00011	0.00001	22,195.17
290.00	Host Rock	2.65	0.00005	0.00007	N/A
291.00	Crater Zone	N/A	N/A	0.00055	N/A
292.00	Crater Zone	N/A	N/A	0.00060	N/A
293.00	Crater Zone	N/A	N/A	0.00070	N/A
294.00	Crater Zone	N/A	N/A	0.00070	N/A
295.00	Crater Zone	2.66	0.00055	0.00061	N/A
296.00	Host Rock	2.66	0.00025	0.00004	8,622.92
297.00	Host Rock	2.70	0.00016	0.00012	N/A
298.00	Host Rock	2.74	N/A	0.00073	N/A
299.00	Root Zone	2.65	0.12491	0.01140	N/A
300.00	Root Zone	2.31	0.06651	0.00642	N/A
301.00	Root Zone	N/A	N/A	0.01520	N/A
302.00	Crater Zone	2.47	0.01058	0.00170	N/A
303.00	Host Rock	2.77	0.00232	0.00018	N/A
304.00	Root Zone	N/A	N/A	0.00128	N/A
305.00	Crater Zone	N/A	N/A	0.00067	197.20
306.00	Crater Zone	2.41	0.00723	0.00029	N/A
307.00	Host Rock	2.75	0.00600	0.00054	15,250.98
308.00	Crater Zone	2.41	0.00470	0.00031	N/A
309.00	Root Zone	N/A	N/A	0.00133	N/A
310.00	Root Zone	2.87	0.22996	0.00175	N/A
311.00	Crater Zone	2.64	0.00227	0.00048	N/A
312.00	Root Zone	2.70	0.00211	0.00045	11,292.79
313.00	Root Zone	N/A	N/A	0.00095	2,495.45
314.00	Host Rock	2.64	0.00296	0.00000	17,260.59
315.00	Host Rock	2.69	0.00347	0.00025	2,313.89
316.00	Crater Zone	2.28	0.46245	0.00234	N/A
317.00	Root Zone	2.78	1.94778	0.01480	N/A
318.00	Crater Zone	2.66	0.59502	0.02700	952.77
319.00	Host Rock	N/A	N/A	0.00047	15,225.64
320.00	Host Rock	2.67	0.00079	0.00040	N/A
321.00	Host Rock	2.68	0.00191	0.00005	N/A
322.00	Host Rock	2.59	0.00137	0.00001	N/A
323.00	Host Rock	2.61	0.00131	0.00034	259.77
325.00	Crater Zone	2.38	0.10831	0.00064	N/A
326.00	Host Rock	N/A	N/A	0.00034	N/A
327.00	Host Rock	2.57	4.86058	0.00248	N/A
328.00	Crater Zone	N/A	N/A	0.00040	N/A
329.00	Crater Zone	N/A	N/A	0.00020	N/A
330.00	Crater Zone	N/A	N/A	0.00032	N/A
331.00	Crater Zone	N/A	N/A	0.00062	N/A
332.00	Host Rock	2.72	0.63474	0.00090	3,882.78
333.00	Host Rock	2.72	0.00655	0.00024	34,113.84
334.00	Host Rock	2.72	0.06517	0.00035	10,881.88

Sample Number	Rock Type	Density (g/cm³)	Remanent Magnetization (A/m)	Magnetic Susceptibility (unitless)	Resistivity (ohm-m)
335.00	Host Rock	2.72	0.05446	0.00037	9,573.94
336.00	Crater Zone	N/A	N/A	0.01760	N/A
337.00	Crater Zone	2.24	0.98391	0.01750	N/A
338.00	Crater Zone	N/A	N/A	N/A	N/A
339.00	Crater Zone	2.38	3.26027	0.02270	N/A
340.00	Crater Zone	N/A	N/A	0.01720	N/A
341.00	Crater Zone	2.59	1.58224	0.01180	N/A
342.00	Host Rock	2.73	0.08657	0.00051	6,376.89
343.00	Host Rock	2.72	0.52894	0.00039	9,508.05
344.00	Crater Zone	2.29	1.74927	0.01790	N/A
345.00	Crater Zone	2.57	1.39994	0.02070	N/A
346.00	Host Rock	2.73	0.00362	0.00017	N/A
347.00	Host Rock	N/A	N/A	N/A	N/A
348.00	Host Rock	2.71	0.00349	0.00009	N/A
349.00	Host Rock	N/A	N/A	0.00016	N/A
350.00	Host Rock	2.65	0.00460	0.00003	N/A
351.00	Crater Zone	2.85	1.13414	0.01080	N/A
352.00	Crater Zone	2.54	1.77913	0.00400	N/A
353.00	Root Zone	2.64	5.47868	0.02860	6,378.70
354.00	Root Zone	2.60	1.84680	0.04300	1,939.03
355.00	Crater Zone	2.72	N/A	0.00047	N/A
356.00	Host Rock	2.70	0.01022	0.00022	N/A
357.00	Host Rock	2.73	0.00179	0.00020	9,881.79
358.00	Host Rock	N/A	N/A	0.00019	16,599.50
359.00	Host Rock	2.72	0.00236	0.00017	10,669.86
360.00	Host Rock	2.73	0.00177	0.00005	N/A
361.00	Host Rock	N/A	N/A	0.00000	N/A
362.00	Crater Zone	2.49	0.08012	0.00096	N/A
363.00	Crater Zone	2.59	1.60330	0.01760	N/A
364.00	Host Rock	2.71	0.00075	0.00018	2,276.78
365.00	Crater Zone	N/A	N/A	0.00333	N/A
366.00	Host Rock	2.62	0.00585	0.00003	2,063.45
367.00	Crater Zone	N/A	N/A	0.00063	N/A
368.00	Crater Zone	N/A	N/A	0.00107	N/A
369.00	Crater Zone	N/A	N/A	0.00019	N/A
370.00	Crater Zone	2.42	0.06532	0.00068	N/A
371.00	Crater Zone	2.58	0.07162	0.00032	N/A
372.00	Crater Zone	2.44	0.04644	0.00041	N/A
373.00	Host Rock	2.70	0.00192	0.00023	1,975.05
374.00	Host Rock	2.65	0.00200	0.00003	12,783.04
375.00	Host Rock	2.72	0.00497	0.00024	5,803.08
376.00	Host Rock	2.64	0.00377	0.00003	9,794.97
377.00	Root Zone	N/A	N/A	0.00551	N/A
378.00	Root Zone	N/A	N/A	0.00318	N/A
379.00	Host Rock	2.62	0.00539	0.00029	1,393.13
380.00	Host Rock	2.78	0.02765	0.00053	3,856.03
381.00	Host Rock	2.74	0.02897	0.00035	26,155.14

Sample Number	Rock Type	Density (g/cm³)	Remanent Magnetization (A/m)	Magnetic Susceptibility (unitless)	Resistivity (ohm-m)
382.00	Root Zone	N/A	N/A	0.00531	N/A
383.00	Root Zone	N/A	N/A	0.00494	N/A
384.00	Host Rock	2.72	0.00710	0.00026	12,400.61
385.00	Host Rock	2.72	0.00855	0.00021	32,670.71
386.00	Crater Zone	N/A	N/A	0.00177	N/A
387.00	Crater Zone	2.50	2.37660	0.00504	N/A
388.00	Crater Zone	2.51	1.63531	0.00364	N/A
389.00	Crater Zone	2.35	3.16034	0.01010	N/A
390.00	Crater Zone	N/A	N/A	0.00889	N/A
391.00	Crater Zone	2.35	4.55893	0.00885	N/A
392.00	Host Rock	2.67	0.00324	0.00012	2,198.26
393.00	Host Rock	2.78	0.00368	0.00023	12,290.89
394.00	Host Rock	2.59	0.00273	0.00000	16,208.15
395.00	Host Rock	2.66	0.00599	0.00000	14,268.99
396.00	Root Zone	N/A	N/A	0.02070	N/A
397.00	Root Zone	2.58	6.30515	0.02780	N/A
398.00	Root Zone	2.29	5.10851	0.01940	N/A
399.00	Root Zone	2.51	N/A	0.03380	N/A
400.00	Root Zone	2.53	3.82177	0.02200	N/A



